Ryerson University
Digital Commons @ Ryerson

Theses and dissertations

1-1-2011

Effect of grain refinement on the microstructure, dendrite coherency and porosity of AZ91E magnesium alloy

Mihai Vlasceanu
Ryerson University

Follow this and additional works at: http://digitalcommons.ryerson.ca/dissertations

Part of the Mechanical Engineering Commons

Recommended Citation
Vlasceanu, Mihai, "Effect of grain refinement on the microstructure, dendrite coherency and porosity of AZ91E magnesium alloy" (2011). *Theses and dissertations.* Paper 689.

This Thesis is brought to you for free and open access by Digital Commons @ Ryerson. It has been accepted for inclusion in Theses and dissertations by an authorized administrator of Digital Commons @ Ryerson. For more information, please contact bcameron@ryerson.ca.

EFFECT OF GRAIN REFINEMENT ON THE MICROSTRUCTURE, DENDRITE COHERENCY AND POROSITY OF AZ91E MAGNESIUM ALLOY

by

Mihai Vlasceanu
B.Eng, Ryerson University, 2008

A thesis
presented to Ryerson University

in partial fulfillment of the
requirements for the degree of
Master of Applied Science
in the Program of
Mechanical Engineering

Toronto, Ontario, Canada, 2011

© Mihai Vlasceanu 2011

AUTHOR'S DECLARATION

I hereby declare that I am the sole author of this thesis.

I authorize Ryerson University to lend this thesis or dissertation to other institutions or individuals for the purpose of scholarly research.

_____

Mihai Vlasceanu

I further authorize Ryerson University to reproduce this thesis by photocopying or by other means, in total or in part, at the request of other institutions or individuals for the purpose of scholarly research.

_____

Mihai Vlasceanu

ABSTRACT

EFFECT OF GRAIN REFINEMENT ON THE MICROSTRUCTURE, DENDRITE COHERENCY AND POROSITY OF AZ91E MAGNESIUM ALLOY

Mihai Vlasceanu

B.Eng, Mechanical Engineering, Ryerson University, 2008

Magnesium (Mg) alloys present a promising alternative to aluminum (Al) alloys in lightweight applications. However, relative to Al alloys, Mg alloys have poor castability. Castability is influenced significantly by the dendrite coherency point (DCP), which represents the temperature, time, and solid fraction at which an interlocking solid network forms during solidification. An increase in the solid fraction at coherency may improve the castability of the alloy and reduce casting defects such as porosity, hot tears and misruns. A successful method for increasing the solid fraction at the DCP in Al alloys involves the use of grain refiners such as titanium (Ti). However, the influence of Ti refiners on the DCP in Mg alloys has not been thoroughly investigated. The objective of this research was to study the effect of Al-5Ti-1B refiner on the dendrite growth mechanism, DCP and porosity of AZ91E magnesium alloy.

This thesis is a pioneering effort in relating the grain refinement effect of Ti on the DCP, coherency solid fraction, and porosity development during the solidification of Mg alloy, AZ91E. It represents an important step in improving the castability of Mg alloys.

Varying levels of Al-5Ti-1B grain refiner (0.005, 0.05, 0.1, 0.2, and 0.3 wt.% Ti) were added to AZ91E. The effect of Al-5Ti-1B grain refiner on the microstructure and dendrite growth mechanism of AZ91E was investigated. Quench experiments were performed to observe transformations in the dendritic morphology that resulted from the refiner additions. The growth rate and DCP were determined using the rheological method. The changes in porosity levels were determined for the grain refiner additions.

The smallest grain size (63% reduction) and largest increase in the coherency solid fraction (double the solid fraction) as compared to base AZ91E was obtained at the 0.005 wt.% Ti level. These improvements were a consequence of the decreased growth rate caused by the growth restricting effect of the refiner and increase in the number of nucleants. The greatest decrease in porosity (from 1.6% to 0.7%) was also achieved at the 0.005 wt.% Ti level. This decrease in porosity was a consequence of the increased coherency solid fraction. With further refiner additions, grain size increased and coherency solid fraction decreased due to the increased dendrite growth rate. This phenomenon was caused by instability in the morphology of the dendrites that subsequently changed from equiaxed to a lancet-like dendritic structure. The lancet structure penetrated through the diffusion layer and caused solute to diffuse sidewise rather than in front of the dendrite tip, thereby causing a substantial increase in growth rate.

From this thesis, it was concluded that the coherency solid fraction can be doubled as compared to the base alloy, with only 0.005 wt.% Ti addition in the form of Al-5Ti-1B grain refiner. This addition level caused a significant improvement in the castability of AZ91E alloy and reduced the casting porosity by 45%.

ACKNOWLEDGEMENTS

Firstly, I thank my supervisor, Professor C. Ravindran, for his continuous support and guidance. The vast amount of knowledge he shared with me was extremely beneficial throughout my graduate studies.

I thank my friends, Sophie, Francesco, Abdallah, Ken, Anthony and Mobaraz at the Centre for Near-net-shape Processing of Materials, for their assistance and helpful ideas. Their companionship made our lab feel like a second home.

I thank Mr. Alan Machin for his advice, technical assistance and useful discussions.

I thank Mr. Joseph Amankrah and Mr. Qiang Li for their technical assistance and aid in SEM analysis.

Lastly, I thank my family and loved ones for their never-ending support and encouragement throughout my life.

TABLE OF CONTENTS

AUTHOR'S DECLARATION ..... **ii**
ABSTRACT…… ..... **iii**
ACKNOWLEDGEMENTS ..... **v**
TABLE OF CONTENTS ..... **vi**
LIST OF FIGURES ..... **ix**
LIST OF TABLES ..... **xiii**
NOMENCLATURE ..... **xv**
Elements xv
English xvi
Greek xvii
CHAPTER 1. INTRODUCTION **1**
CHAPTER 2. LITERATURE REVIEW **3**
2.1 AZ91 Magnesium Alloy 3
2.1.1 Microstructure 3
2.1.2 Common Casting Defects 4
2.2 Solidification Mechanism 6
2.2.1 Nucleation 6
2.2.1.1 Homogeneous Nucleation 7
2.2.1.2 Heterogeneous Nucleation 9
2.2.2 Growth 11
2.3 Dendrite Coherency 15
2.3.1 Influence of Dendrite Coherency on Castability and Casting Defects 16
2.3.2 Techniques to Determine the Dendrite Coherency Point 17
2.3.2.1 Mechanical Analysis 18
2.3.2.1.1 Rheological Method 18
2.3.2.1.2 Direct Shear-Cell Method 20
2.3.2.2 Thermal Analysis 21
2.3.2.2.1 One-Thermocouple Method 21
2.3.2.2.2 Two-Thermocouple Method 21

2.3.2.3 Comparison of Methods 23
2.3.3 Factors Affecting the Dendrite Coherency Point.....23
2.3.3.1 Effect of Cooling Rate.....23
2.3.3.2 Effect of Alloying.....25
2.3.3.3 Effect of Grain Refiner Addition 27
2.4 Chapter Summary 29
CHAPTER 3. OPTIMIZATION OF RHEOLOGICAL EXPERIMENT 30
3.1 Experimental Setup.....30
3.2 Control of Cooling Rate.....32
3.3 Control of Spindle Rotation Speed 33
3.4 Control of Spindle Temperature.....35
3.5 Summary of Rheological Experiments 37
CHAPTER 4. EXPERIMENTAL PROCEDURE 38
4.1 Rheological Experiments 38
4.1.1 Pre-Melting Procedure 38
4.1.2 Melting Procedure.....39
4.1.3 Post-Melting Procedure.....39
4.2 Quench Experiments.....40
4.2.1 Specimen Casting 40
4.2.2 Quenching 40
4.3 Preparation for Microscopy and Grain Size Measurements 42
4.4 Porosity Experiments.....43
4.5 Summary of Experiments.....44
CHAPTER 5. RESULTS AND DISCUSSION 46
5.1 Microstructure 46
5.1.1 Grain Size Measurements.....46
5.1.2 AZ91E General Microstructure 48
5.1.3 Nucleation of Grains 49
5.1.4 Growth of Dendrites 51
5.2 Rheological Analysis 54
5.2.1 Dendrite Growth Rate 55

5.2.2 Coherency Solid Fraction 57
5.3 Porosity Analysis 59
CHAPTER 6. CONCLUSIONS AND SUGGESTIONS FOR FUTURE WORK 61
6.1 Conclusions 61
6.2 Suggestions for Future Work 63
REFERENCES…… 64
APPENDIX A COOLING CURVES AND RHEOLOGICAL PLOTS 67
A.1 A319 Alloy 67
A.2 AZ91 Base Alloy 67
A.3 AZ91 Base Alloy at 0.005 wt.% Ti Addition Level 70
A.4 AZ91 Base Alloy at 0.05 wt.% Ti Addition Level 72
A.5 AZ91 Base Alloy at 0.10 wt.% Ti Addition Level 75
A.6 AZ91 Base Alloy at 0.20 wt.% Ti Addition Level 77
A.7 AZ91 Base Alloy at 0.30 wt.% Ti Addition Level 79
APPENDIX B RHEOLOGICAL EXPERIMENTS SEM 81
B.1 AZ91 Base Alloy at 0.30 wt.% Ti Addition Level 81
APPENDIX C QUENCH EXPERIMENTS SEM 83
C.1 AZ91 Base Alloy at 0.005 wt.% Ti Addition Level 83
C.2 AZ91 Base Alloy at 0.05 wt.% Ti Addition Level 86
C.3 AZ91 Base Alloy at 0.10 wt.% Ti Addition Level 87
C.4 AZ91 Base Alloy at 0.20 wt.% Ti Addition Level 88
C.5 AZ91 Base Alloy at 0.30 wt.% Ti Addition Level 89
APPENDIX D ANOVA ANALYSIS 90
D.1 ANOVA Analysis of Grain Size 90
D.2 ANOVA Analysis of Growth Rate 92
D.3 ANOVA Analysis of Coherency Solid Fraction 93
D.4 ANOVA Analysis of Porosity 95

LIST OF FIGURES

Figure 1. Outline of the experiments.....2
Figure 2. AZ91 magnesium alloy microstructure showing (a) the equiaxed grain structure and (b) the hexagonal dendritic morphology revealed by coring within a grain [11]. 4
Figure 3. Segregation of thin oxide skin in an AZ91 alloy at 375X magnification [16]. 5
Figure 4. Shrinkage porosity in AZ92 sand casting at 150X magnification [16].....5
Figure 5. Hot tear in AZ91 alloy during die casting at 150X magnification [16]. 6
Figure 6. Homogeneous nucleation illustrating the free energy of a) liquid state (G1) and b) liquid and solid state (G2) [17].....7
Figure 7. Change in free energy with the formation of a solid sphere during homogeneous nucleation [17]. 9
Figure 8. Heterogeneous nucleation of spherical cap on a flat mould wall [17]. 10
Figure 9. a) Variation in ΔG^* with undercooling (ΔT) for homogeneous and heterogeneous nucleation, and b) corresponding nucleation rates [17]. 11
Figure 10. Breakdown of a planar solidification front into cells [17].....12
Figure 11. Illustration of a) cell, b) dendritic cell and c) dendrite [19].....13
Figure 12. Schematic of a casting illustrating three zones (chilled, columnar, equiaxed) [17]. ...14
Figure 13. Schematic of dendritic growth at mould wall [17].....14
Figure 14. Formation of columnar and equiaxed dendrites [19]. 15
Figure 15. Dendritic structure during solidification at various solid fractions [5]. 17
Figure 16. Rheological experimental setup (all units are in mm) [8]. 19
Figure 17. Temperature (T) and torque data (Tq) obtained from rheological experiment on a solidifying Al alloy [8].....19
Figure 18. Rheological data for AZ91 magnesium alloy [11].....20
Figure 19. Schematic of shear-cell. Crucible has 50 mm diameter and 55 mm depth [7].....20
Figure 20. Thermal analysis for one-thermocouple method [23]. 22
Figure 21. Thermal analysis for two-thermocouple method [23].....22
Figure 22. Micrographs showing the microstructures of $AlSi_7Cu_2$ that solidified: (a) 0.16 °C/s, (b) 0.46 °C/s, (c) 0.72 °C/s [22].....24
Figure 23. Cooling rate effect on grain size, SDAS and UTS of an $AlSi_7Cu_2$ alloy [22].....25

Figure 24. Schematic of apparatus used for rheological experiments. 31
Figure 25. Schematic of experimental setup for rheological experiments. 31
Figure 26. Crucible dimensions for rheological experiments.....32
Figure 27. Rheological data and cooling curve for A319 alloy with 5 RPM spindle speed. 33
Figure 28. Rheological data and cooling curve for A319 alloy with 1 RPM spindle speed. 34
Figure 29. Rheological data and cooling curve for A319 alloy with 0.5 RPM spindle speed. 35
Figure 30. Rheological data and cooling curve for A319 alloy with preheated spindle at 0.5 RPM spindle speed.....36
Figure 31. Schematic of the graphite mould used for quench experiments (units in mm). 41
Figure 32. Schematic of tube apparatus used for quench experiments (units in mm). 42
Figure 33. Microscopy sample location from rheological and quench experiments (units in mm). 43
Figure 34. Graphite mould for porosity experiments (units in mm). 44
Figure 35. Optical micrographs of the grain size for AZ91E base alloy at various addition levels. 47
Figure 36. Effect of grain refiner addition on the average grain size of AZ91E alloy. 47
Figure 37. SEM micrograph of unrefined AZ91E alloy showing a) general microstructure and EDX scans of b) primary α-Mg, c) $Mg_{17}Al_{12}$, and d) Mn_X-Al_Y phases. 49
Figure 38. SEM of quenched AZ91E at 0.005 wt.% Ti level illustrating a) equiaxed dendrite, b) enlarged view of Ti particle at the centre of dendrite, and c) EDX of the particle. 50
Figure 39. a) SEM micrograph and b) EDX for a rhelogical sample at the 0.3 wt.% Ti addition level illustrating the segregation of Ti particles at the eutectic region. 51
Figure 40. a) SEM micrograph and b) EDX for a quenched sample at the 0.3 wt.% Ti addition level illustrating the segregation of Ti particles to the solid-liquid interface. 52
Figure 41. SEM micrographs illustrating the change from the equiaxed dendritic structure (at 0.005wt% Ti) to a progressively more lancet-like structure with further Ti additions. 53
Figure 42. Typical rheological data and cooling curve obtained for AZ91E base alloy. 55
Figure 43. Effect of Ti level on the average dendrite growth rate of AZ91E. 57
Figure 44. Effect of Ti level on the average coherency solid fraction of AZ91E. 58
Figure 45. Effect of Ti addition level on the average porosity of cast AZ91E. 59

Figure A.1.1. Repeat rheological data and cooling curve for preheated spindle at 0.5 RPM spindle speed. 67

Figure A.2.1. First rheological data and cooling curve for AZ91 base alloy. 67
Figure A.2.2. Second rheological data and cooling curve for AZ91 base alloy. 68
Figure A.2.3. Third rheological data and cooling curve for AZ91 base alloy. 68
Figure A.2.4. Fourth rheological data and cooling curve for AZ91 base alloy. 69
Figure A.2.5. Fifth rheological data and cooling curve for AZ91 base alloy. 69
Figure A.2.6. Sixth rheological data and cooling curve for AZ91 base alloy. 70

Figure A.3.1. First rheological data and cooling curve for AZ91 alloy at 0.005 wt.% Ti level. ... 70
Figure A.3.2. Second rheological data and cooling curve for AZ91 alloy at 0.005 wt.% Ti level. 71
Figure A.3.3. Third rheological data and cooling curve for AZ91 alloy at 0.005 wt.% Ti level. . 71

Figure A.4.1. First rheological data and cooling curve for AZ91 alloy at 0.05 wt.% Ti level. 72
Figure A.4.2. Second rheological data and cooling curve for AZ91 alloy at 0.05 wt.% Ti level. 72
Figure A.4.3. Third rheological data and cooling curve for AZ91 alloy at 0.05 wt.% Ti level. ... 73
Figure A.4.4. Fourth rheological data and cooling curve for AZ91 alloy at 0.05 wt.% Ti level. . 73
Figure A.4.5. Fifth rheological data and cooling curve for AZ91 alloy at 0.05 wt.% Ti level. 74
Figure A.4.6. Sixth rheological data and cooling curve for AZ91 alloy at 0.05 wt.% Ti level. 74

Figure A.5.1. First rheological data and cooling curve for AZ91 alloy at 0.10 wt.% Ti level. 75
Figure A.5.2. Second rheological data and cooling curve for AZ91 alloy at 0.10 wt.% Ti level. 75
Figure A.5.3. Third rheological data and cooling curve for AZ91 alloy at 0.10 wt.% Ti level. ... 76
Figure A.5.4. Fourth rheological data and cooling curve for AZ91 alloy at 0.10 wt.% Ti level. . 76

Figure A.6.1. First rheological data and cooling curve for AZ91 alloy at 0.20 wt.% Ti level. 77
Figure A.6.2. Second rheological data and cooling curve for AZ91 alloy at 0.20 wt.% Ti level. 77
Figure A.6.3. Third rheological data and cooling curve for AZ91 alloy at 0.20 wt.% Ti level. ... 78
Figure A.6.4. Fourth rheological data and cooling curve for AZ91 alloy at 0.20 wt.% Ti level. . 78

Figure A.7.1. First rheological data and cooling curve for AZ91 alloy at 0.30 wt.% Ti level.....79
Figure A.7.2. Second rheological data and cooling curve for AZ91 alloy at 0.30 wt.% Ti level. 79
Figure A.7.3. Third rheological data and cooling curve for AZ91 alloy at 0.30 wt.% Ti level. ...80

Figure B.1.1. SEM micrograph of AZ91E alloy at the 0.3 wt.% Ti addition level showing a) general microstructure and EDX scans of b) primary α-Mg, c) $Mg_{17}Al_{12}$, and d) Mn_X-Al_Y phases. 81
Figure B.1.2. a) SEM micrograph and b) EDX for a rhelogical sample at the 0.3 wt.% Ti addition level illustrating the segregation of Ti particles at the eutectic region. 82

Figure C.1.1. SEM micrograph at one location illustrating a) dendritic structure, b) enlarged view of Ti particle at the centre of dendrite, and c) EDX of Ti particle.....83
Figure C.1.2. SEM micrograph at a second location illustrating a) dendritic structure, b) enlarged view of Ti particle at the centre of dendrite, and c) EDX of Ti particle. 84
Figure C.1.3. SEM micrograph at a third location illustrating a) dendritic structure, b) enlarged view of Ti particle at the centre of dendrite, and c) EDX of Ti particle. 85

Figure C.2.1. SEM micrograph at the transition stage from equiaxed to lancet dendrites. 86
Figure C.2.2. A second SEM micrograph at the transition stage from equiaxed to lancet dendrites. 86

Figure C.3.1. SEM micrograph illustrating progressively more lancet dendritic structure. 87
Figure C.3.2. A second SEM micrograph illustrating progressively more lancet dendritic structure.....87

Figure C.4.1. SEM micrograph illustrating the lancet dendritic morphology.....88
Figure C.4.2. A second SEM micrograph illustrating the lancet dendritic morphology. 88

Figure C.5.1. SEM micrograph illustrating the lancet dendritic morphology.....89

LIST OF TABLES

Table 1. Effect of cooling rate on coherency solid fraction in Al alloy 355 [8].....23
Table 2. Values for m, k and GRF for various alloying elements in magnesium [28]. 26
Table 3. Thermal analysis results for the coherency solid fractions for AZ91 alloy at various Ca levels [15]. 27
Table 4. A319 alloy composition (wt.%). 30
Table 5. Rheological experiments performed on A319 alloy. 37
Table 6. AZ91E alloy composition (wt.%). 38
Table 7. Al-5Ti-1B master alloy composition (wt.%). 39
Table 8. Rheological experiments performed on AZ91E alloy. 45
Table 9. Quench experiments performed on AZ91E alloy. 45
Table 10. Porosity experiments performed on AZ91E alloy. 45
Table 11. Rheological data obtained for AZ91E alloy at the tested addition levels. 56
Table 12. Influence of Ti level in AZ91E on the average grain size, growth rate, coherency solid fraction, and porosity. 60

Table D.1.1. Grain size values for the base alloy and all addition levels. 90
Table D.1.2. ANOVA (single factor) of grain size for base alloy and 0.005 wt.% Ti level. 90
Table D.1.3. ANOVA (single factor) of grain size for 0.005 wt.% Ti and 0.05 wt.% Ti level. ...91
Table D.1.4. ANOVA (single factor) of grain size for 0.05 wt.% Ti and 0.1 wt.% Ti level. 91

Table D.2.1. Growth rate values for the base alloy and all addition levels. 92
Table D.2.2. ANOVA (single factor) of growth rate for base alloy and 0.005 wt.% Ti level. 92
Table D.2.3. ANOVA (single factor) of growth rate for 0.005 wt.% Ti and 0.05 wt.% Ti level. .93

Table D.3.1. Dendrite coherency solid fraction values for the base alloy and all addition levels. 93
Table D.3.2. ANOVA (single factor) of dendrite coherency solid fraction for base alloy and 0.005 wt.% Ti level. 94
Table D.3.3. ANOVA (single factor) of dendrite coherency solid fraction for 0.005 wt.% Ti and 0.05 wt.% Ti level. 94

Table D.4.1. Porosity values for the base alloy and all addition levels. 95
Table D.4.2. ANOVA (single factor) of porosity for base alloy and 0.005 wt.% Ti level. 95
Table D.4.3. ANOVA (single factor) of porosity for 0.005 wt.% Ti and 0.05 wt.% Ti level.....96

NOMENCLATURE

Elements

Al – Aluminum

B – Boron

Ce – Cerium

Cu – Copper

Fe – Iron

Ge – Germanium

Mg – Magnesium

Mn – Manganese

Ni – Nickel

Pb – Lead

Sc – Scandium

Si – Silicon

Sn – Tin

Sr – Strontium

Ti – Titanium

V – Vanadium

Y - Yttrium

Yb - Ytterbium

Zn – Zinc

Zr – Zirconium

English

ANOVA – Analysis of variance

A_{SL} – Area at the solid/liquid interface

A_{SM} – Area at the solid/mould interface

D – Diffusion coefficient in the liquid

DCP – Dendrite coherency point

EDX – Energy dispersive X-ray spectroscopy

GRF – Growth restriction factor

G_V^L – Free energies per unit volume of the liquid

G_V^S – Free energies per unit volume of the solid

HCP – Hexagonal close-packed

k – Partition coefficient

L_V – Latent heat of fusion per unit volume

m – Slope of the liquidus line

mm – Millimeter

r – Radius of a sphere

r^* – Critical radius of an embryo to become a nucleant

R – Grain radius

SEM – Scanning electron microscopy

t – Time from liquidus to the dendrite coherency point

DCT – Coherency Temperature

T_L – Liquidus temperature of the alloy

T_M – Melting point of the pure metal

T_S – Solidus temperature of the alloy

V – Dendrite growth rate

V_S – Volume of the solid

Greek

δ_c – Thickness of the diffusion layer in front of the growing dendrite

ΔG – Change in free energy

ΔG_{het} – Energy barrier for heterogeneous nucleation

ΔG_{hom} – Energy barrier for homogeneous nucleation

ΔG_r – Change in free energy of a sphere

ΔG^* – Change in free energy of a sphere with a radius r^*

ΔT – Undercooling of a melt

µm – Micrometer

γ_{SL} – Free energy at the solid/liquid interface

γ_{SM} – Free energy at the solid/mould interface

γ_{ML} – Free energy at the mould/liquid interface

CHAPTER 1. INTRODUCTION

Magnesium (Mg) alloys have the lowest density of all structural metals (approximately 35% less dense than aluminum and 80% less dense than steel) [1, 2]. For this reason, Mg alloys have gained popularity in the automotive and aerospace industry. Mg alloys are commonly used for the manufacturing of cast engines and transmission housings for helicopters [1]. Volkswagen used magnesium for the crankcase and transmission housing of the Beetle. These components weighed a total of 17 kg, which was said to represent a savings of 50 kg when compared with using cast iron components. This saving of weight played a critical role in improving the stability of the rear-engine vehicle [1]. Of the Mg-Al alloys, AZ91 alloy is among the most common due to its high corrosion resistance and good castability in comparison to the other Mg alloys [1].

At room temperature, Mg alloys have limited slip systems due to their hexagonal close-packed (HCP) crystal structure. HCP crystal structures have three slip systems, whereas face-centred cubic (FCC) structures have 12 possible slip systems. Consequently, it is difficult to cold work alloys with an HCP structure. As a result, Mg parts are generally manufactured using casting processes [3]. The quality of the casting is strongly dependent on the castability of the alloy. Alloys with poor castability are more susceptible to porosity, hot tears and misruns [4, 5]. A key factor influencing the castability of the alloy is the point of dendrite impingement, commonly referred to as the dendrite coherency point (DCP). The DCP represents the instance at which an interlocking solid network has formed within the molten metal. Once the dendrites become coherent, liquid metal flow is restricted to interdendritic regions. Increasing the coherency solid fraction can have a strong positive influence on the castability of the alloy [6].

There are several methods to determine the DCP. Such methods include rheological analysis, shear cell and thermal analysis [7, 8]. In this thesis, the rheological method was used to identify the DCP. The rheological method is based on detecting significant mechanical changes that occur during solidification. At the DCP, the dendrites interlock, thereby increasing the shear stress that can be supported by the solidifying melt [9, 10]. The DCP is influenced by cooling rate, alloy composition and grain refiner additions.

Al-5Ti-1B (TIBOR®) master alloy is commonly used in the aluminum industry as a grain refiner and to delay the DCP of the cast alloy. The influence of TIBOR on the castability of AZ91E alloy however, has not been investigated. The aim of this thesis was to examine the effect of TIBOR grain refiner on the microstructure, dendritic morphology, DCP and casting porosity of AZ91E base alloy, in an effort to improve the alloy castability.

The relevant literature, with particular focus on previous research on dendrite coherency, is provided in Chapter 2. The optimization of the rheological experiment, with a focus on controlling the cooling rate and ensuring accurate significant rheological data, is discussed in Chapter 3. The experimental methods for examining the microstructure, determination of the DCP, and analysis of the porosity of the castings are presented in Chapter 4. The microstructural, rheological and porosity results are analyzed in Chapter 5. Finally, the conclusions of this research and proposed future research are summarized in Chapters 6 and 7, respectively. An outline of the experiments conducted in this thesis is presented in Figure 1 below.

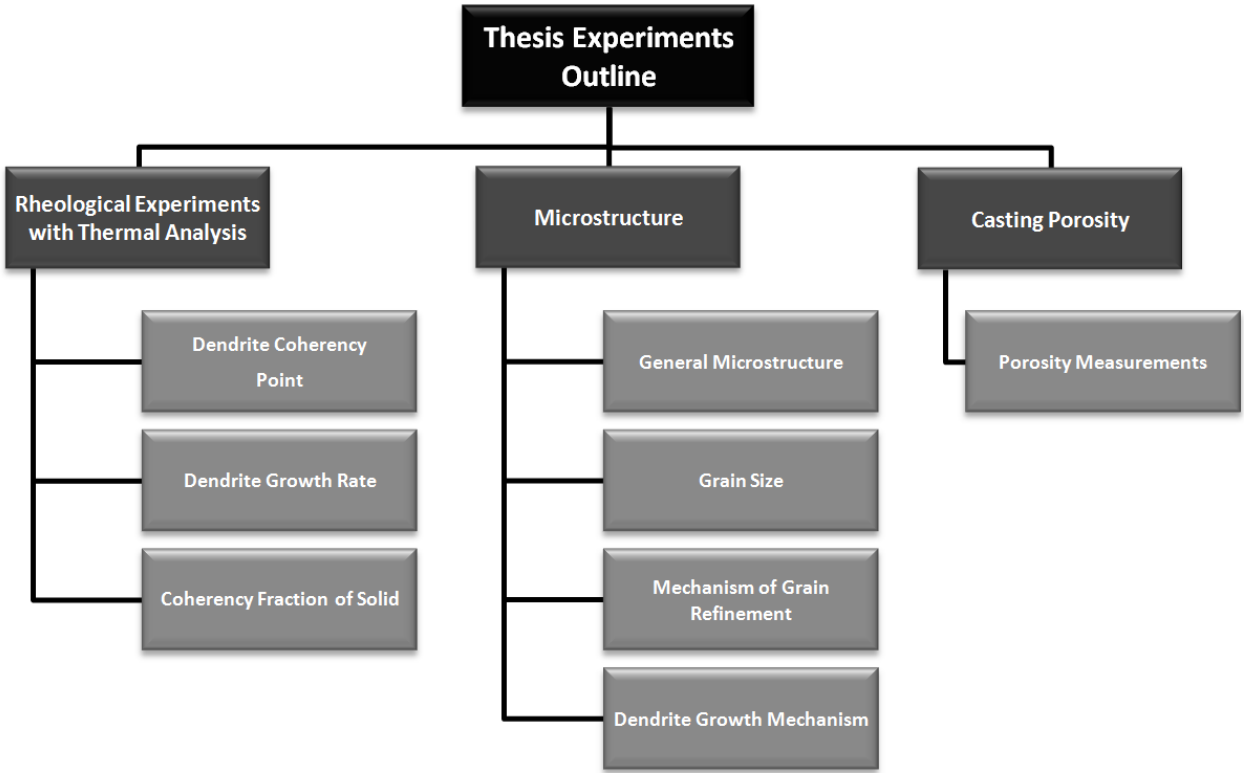

Figure 1. Outline of the experiments.

CHAPTER 2. LITERATURE REVIEW

In this chapter, the material properties and common casting defects for AZ91 magnesium alloy are presented. A discussion on the mechanisms for nucleation and growth of a solidifying metal then follows. Finally, the importance of studying dendrite coherency is discussed, along with the methods used to determine the dendrite coherency point (DCP) and the factors influencing the DCP, with a view to providing the focus of this study.

2.1 AZ91 Magnesium Alloy

Magnesium-aluminum alloys are the most common magnesium (Mg) alloys. Aluminum (Al) is one of the most preferred and common alloying elements for Mg alloys. The addition of Al to Mg improves the strength, increases the hardness and widens the freezing range, making the Mg alloy generally easier to cast [1].

Of the Mg-Al alloys, AZ91 alloy (9% aluminum, 0.7% zinc and 0.15% manganese) is one of the most commonly used alloys due to its high corrosion resistance and good castability in comparison to other Mg alloys [1]. The density of AZ91 alloy is 1.81 g/cm^3, slightly higher than that of pure Mg (1.738 g/cm^3) but significantly lower than that of pure Al (2.7 g/cm^3) [1, 2]. The published liquidus and solidus temperatures of the alloy are approximately 598 °C and 468 °C respectively [1]. As an alloying addition, zinc (Zn) improves the room temperature strength of the Mg alloy [1]. The most important function of the manganese (Mn) addition is to improve the saltwater resistance of this alloy. Manganese also slightly increases the yield strength [1].

2.1.1 Microstructure

Magnesium has a hexagonal close-packed (HCP) structure. As a result, cast AZ91 alloy has a six-fold dendritic structure [11, 12]. Common particles found at the centre of the dendritic structure in AZ91 alloys are Mn-Al particles (MnAl, $MnAl_4$, or $MnAl_6$) [1, 13]. The primary α-Mg dendrites grow in an equiaxed manner, given nearly isotropic heat flow [1, 13]. The equiaxed

grain structure and hexagonal dendritic morphology for an AZ91 alloy is shown in Figure 2. Once the diffusion fields overlap, the dendrite arms cease to grow in length. At this point, the dendrite arms continue to thicken while further solute is pushed to the boundaries of the dendrite arms. The last portion of liquid to solidify is the Mg_{17}-Al_{12} eutectic [14, 15].

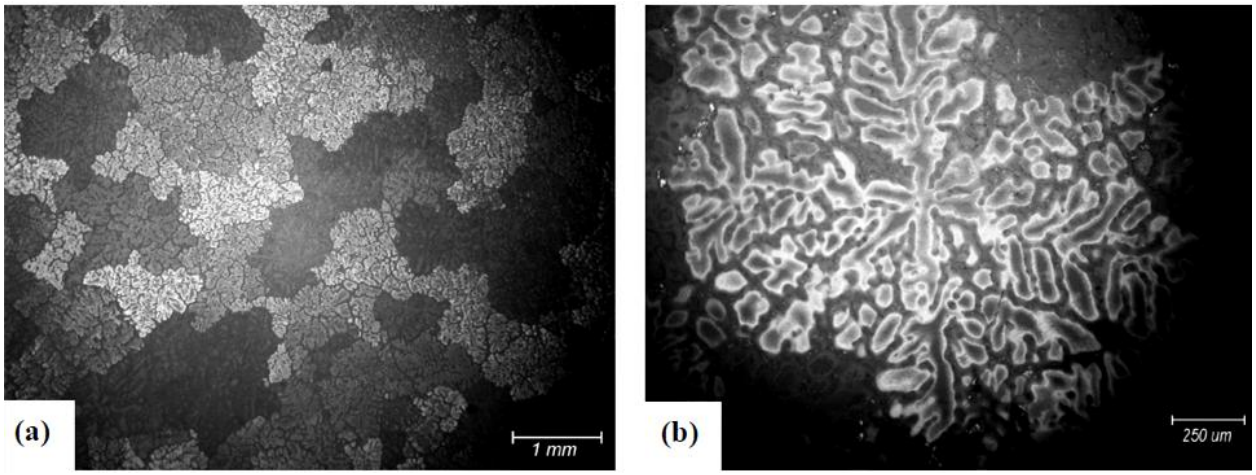

Figure 2. AZ91 magnesium alloy microstructure showing (a) the equiaxed grain structure and (b) the hexagonal dendritic morphology revealed by coring within a grain [11].

2.1.2 Common Casting Defects

One of the difficulties encountered in casting AZ91 alloy is protecting the melt from oxide formation. Unlike Al alloys which form a continuous thin oxide layer that prevents further oxidation during solidification, Mg alloys form a permeable oxide skin. The permeability of the oxide layer does not restrict oxygen from being in contact with the melt and, as a consequence, further oxide continues to form throughout solidification. One method to prevent the formation of magnesium oxide (MgO) is by melting and pouring Mg alloys in a vacuum chamber [13]. This however, is not a suitable solution since casting, in the industry, is not done in vacuum chambers. A practical solution to the oxidation problem is to protect the melt with an inert cover gas (such as CO_2). MgO can form if the melt is not properly protected. Further, due to turbulence from pouring of liquid metal, MgO can be included in the casting (Figure 3).

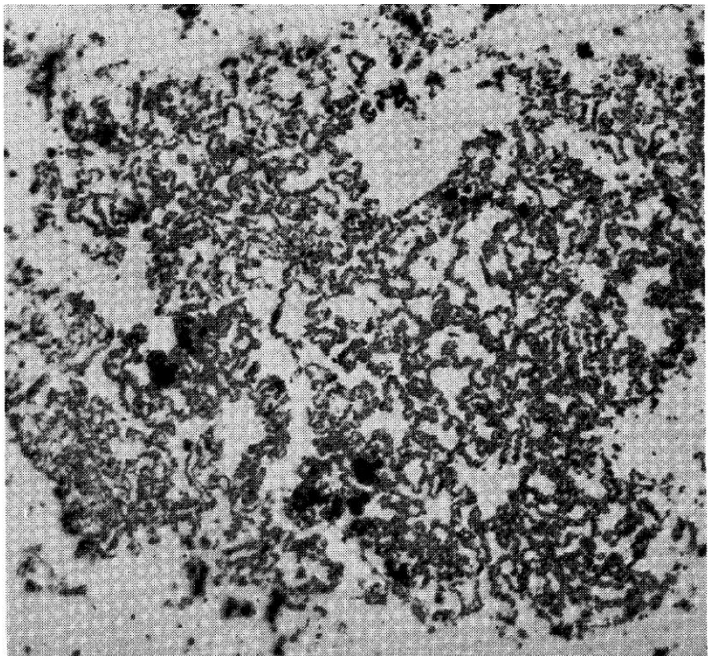

Figure 3. Segregation of thin oxide skin in an AZ91 alloy at 375X magnification [16].

Shrinkage porosity is another common defect encountered during casting of AZ91. Porosity is caused by a blockage of the feeding channels and the subsequent shrinkage of the entrapped liquid metal. An example of shrinkage porosity is illustrated in Figure 4.

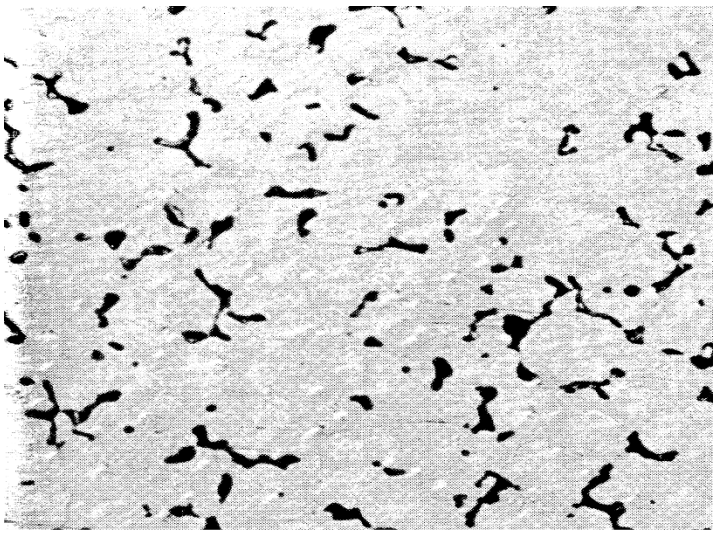

Figure 4. Shrinkage porosity in AZ92 sand casting at 150X magnification [16].

Blockage of the feeding channels in areas where the material is under thermal contractive stresses can lead to the formation of another type of casting defect known as a hot tear. An example of a hot tear in AZ91 alloy is illustrated in Figure 5.

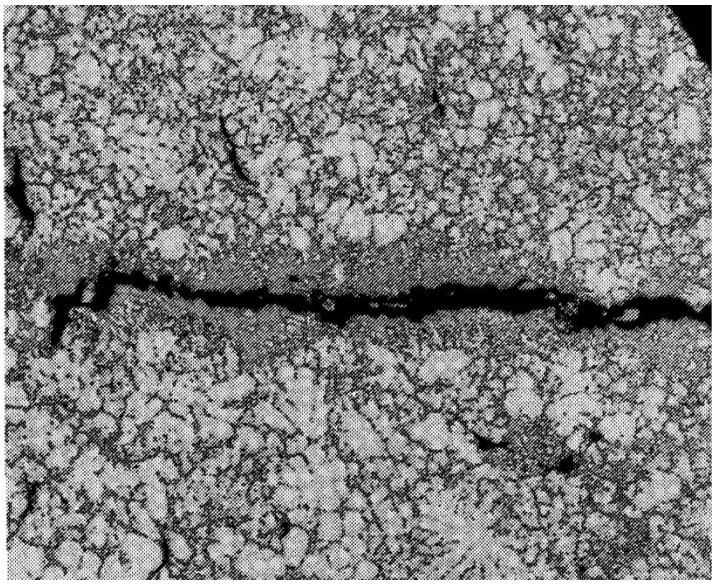

Figure 5. Hot tear in AZ91 alloy during die casting at 150X magnification [16].

2.2 Solidification Mechanism

The solidification mechanism for a pure metal or alloy can be divided into two stages. The first stage of solidification is nucleation. After the formation of stable nuclei in the solidifying melt, the growth stage follows.

2.2.1 Nucleation

It is not enough to cool liquid metal below the equilibrium liquidus temperature to initiate solidification. Molten metal will not begin to solidify until the required driving force for nucleation is reached. This driving force is provided by the local undercooling of the melt. If a sufficiently high undercooling is obtained, nucleation will start. Nucleation can be further divided into two types: homogeneous and heterogeneous. For homogeneous nucleation, the nuclei have the same composition as the phase that forms after nucleation. In heterogeneous

nucleation, the nucleating particle, commonly an impurity, has a composition different from the primary phase that forms thereafter.

2.2.1.1 Homogeneous Nucleation

In the liquid state of the metal, there are many small clusters of atoms (embryos) with the same crystalline orientation as in the solid state. As the temperature of the melt decreases below the equilibrium liquidus temperature, the clusters become more stable and the probability of finding larger clusters within the melt increases. To determine whether the embryo will dissolve or become a nucleant and continue to grow in the melt, the total free energy of the system must be analyzed. The free energies associated with each state are illustrated in Figure 6.

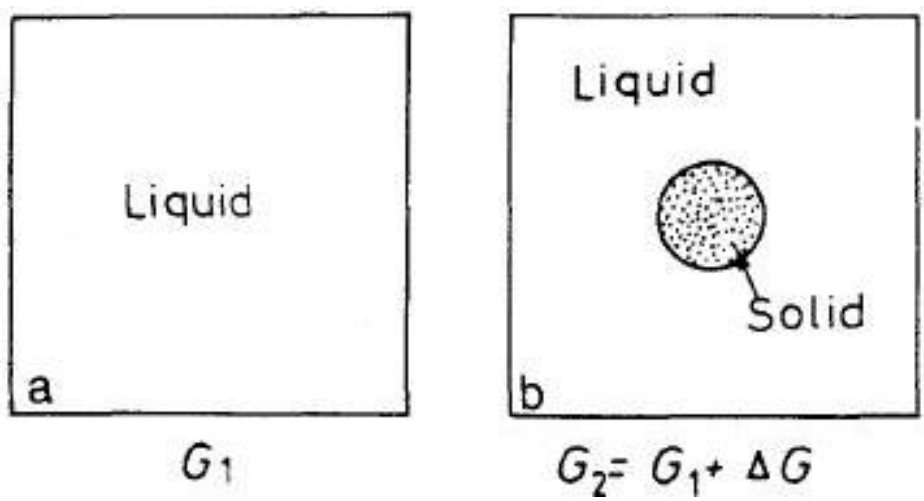

a) b)

Figure 6. Homogeneous nucleation illustrating the free energy of a) liquid state (G1) and b) liquid and solid state (G2) [17].

Due to the lower volume free energy of the solid as compared to the liquid, there is a negative contribution to the free energy of the system. The formation of a new solid/liquid interface however has a positive contribution to the free energy of the system. As a result, the change in free energy ΔG, through the formation of a solid, is given by

$$\Delta G = - V_S (G_V^L - G_V^S) + A_{SL}\gamma_{SL} \quad (1)$$

where V_S is the volume of the solid, G_V^L and G_V^S are the free energies per unit volume of the liquid and solid respectively, A_{SL} is the area at the solid/liquid interface and γ_{SL} is the free energy at the solid/liquid interface [17]. $A_{SL}\gamma_{SL}$ represents the interfacial free energy.

If the solid forming is assumed to be spherical, the change in free energy ΔG_r is given by

$$\Delta G_r = - 4/3\ \pi r^3 \Delta G_V + 4\pi r^2 \gamma_{SL} \qquad (2)$$

where r is the radius of the solid sphere and $\Delta G_V = G_V^L - G_V^S$ [17]. ΔG_V is dependent on the undercooling of the melt ΔT through the following equation:

$$\Delta G_V = (L_V \Delta T) / T_M \qquad (3)$$

where L_V is the latent heat of fusion per unit volume and T_M is the melting point of the metal [17]. For an embryo to become a nucleant, the radius of the solid sphere must reach a critical value r^* (Figure 7). The change in free energy at this instant is ΔG^*. If the radius of the sphere is smaller than r^*, the embryo will dissolve in the melt.

Due to the dependence of ΔG_V on ΔT, an increase in the local undercooling will decrease the critical radius r^*. If the undercooling is not large enough, nucleation will not occur due to the small probability of finding an embryo at a given instant with a radius greater than r^* [17]. In practice however, the undercooling required for nucleation is lower than the theoretical value due to the presence of impurity particles and the use of the mould wall as sites for heterogeneous nucleation.

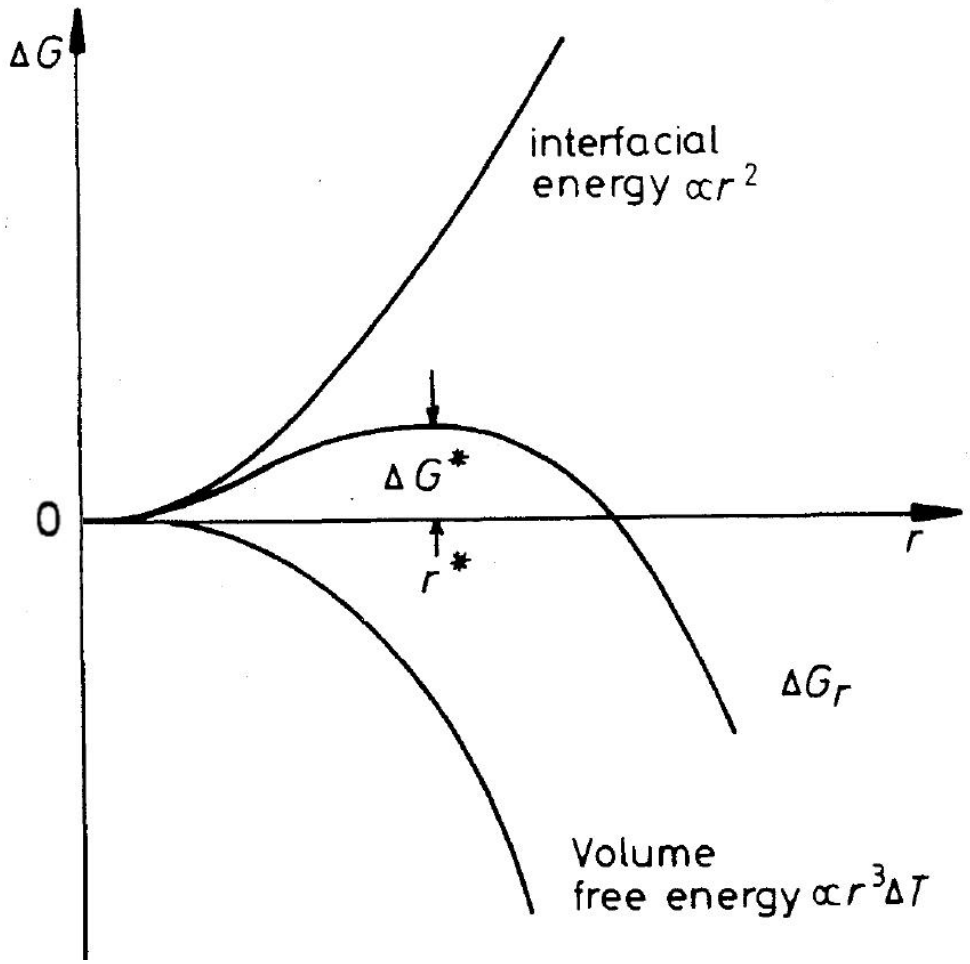

Figure 7. Change in free energy with the formation of a solid sphere during homogeneous nucleation [17].

2.2.1.2 Heterogeneous Nucleation

Heterogeneous nucleation differs from homogeneous nucleation in that the substrate that initiates solidification is of a different composition than the primary phase that forms thereafter. For heterogeneous nucleation, the embryo takes the form of a spherical cap with a wetting angle θ (Figure 8). The wetting angle is dependent on the lattice match between the particle and the substrate. A good lattice match will result in a lower wetting angle. One method to examine the lattice match is by analyzing the disregistry between the nucleating substrate and the crystal being formed. For heterogeneous nucleation, a planar disregistry of less than 10% is generally required [18].

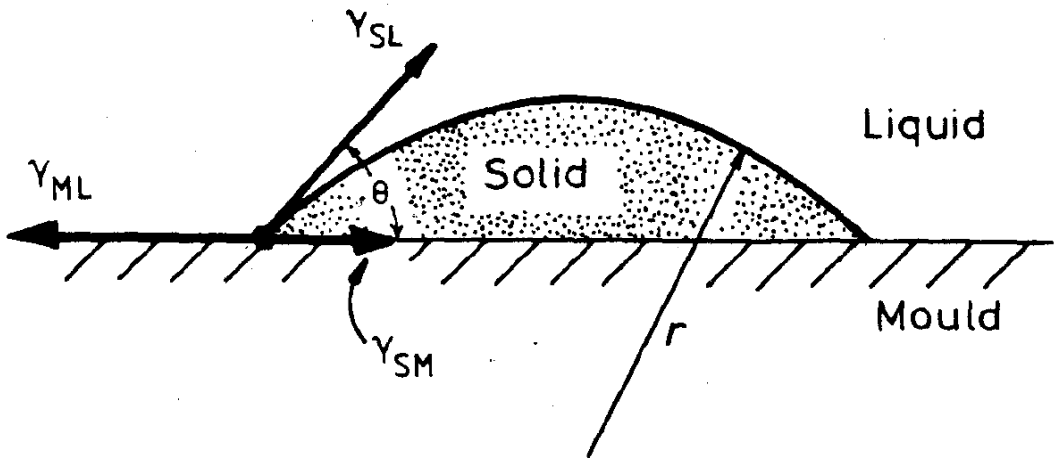

Figure 8. Heterogeneous nucleation of spherical cap on a flat mould wall [17].

The critical radius required for nucleation remains the same regardless of whether heterogeneous nucleation or homogeneous nucleation occurs. However, the energy barrier ΔG can be decreased significantly through heterogeneous nucleation. This is accomplished by lowering the interfacial energy. The interfacial energy decreases as the contact angle decreases, thereby subsequently reducing the energy barrier required for nucleation. The energy barrier for heterogeneous nucleation ΔG_{het} is given by the following equation:

$$\Delta G_{het} = - V_S \Delta G_V + A_{SL}\gamma_{SL} + A_{SM}\gamma_{SM} - A_{SM}\gamma_{ML} \quad (4)$$

where V_S is the volume of the spherical cap, ΔG_V is the same as for homogeneous nucleation, A_{SL} is the area of the solid/liquid interface, A_{SM} is the area of the solid/mould interface, and γ_{SL}, γ_{SM}, γ_{ML} are the free energies of the solid/liquid, solid/mould and mould/liquid interfaces respectively [17].

As a consequence of the decreased energy barrier with heterogeneous nucleation, smaller undercoolings are required for nucleation to occur. The variation in ΔG_{het} and ΔG_{hom} with change in undercooling is shown in Figure 9a. Figure 9b illustrates that for the same energy barrier, heterogeneous nucleation will initiate at significantly lower undercoolings in comparison to homogeneous nucleation. The nucleation rates for both heterogeneous and homogeneous nucleation increase drastically as the undercooling increases past the critical value.

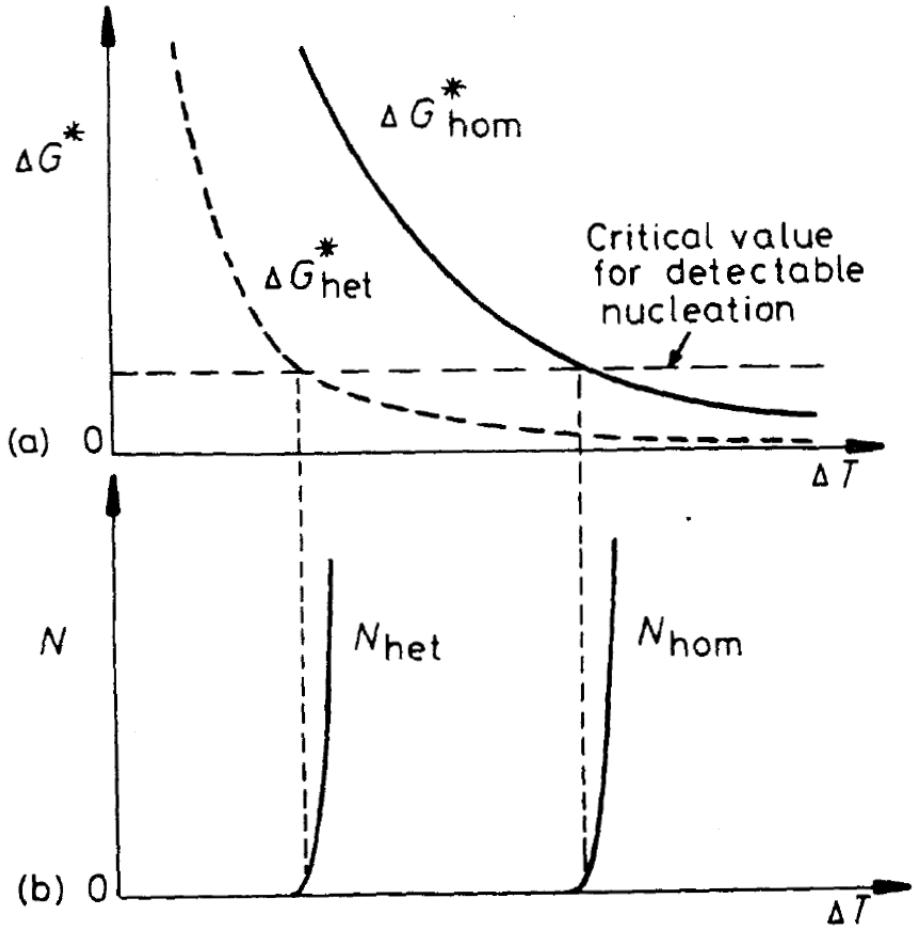

Figure 9. a) Variation in ΔG* with undercooling (ΔT) for homogeneous and heterogeneous nucleation, and b) corresponding nucleation rates [17].

2.2.2 Growth

Growth in pure metals differs from growth in alloys. Solidification as a pure metal, however, is rarely experienced in practice because impurity particles in the melt would alter the mechanics of solidification from pure metal to alloy behaviour. There are three distinct growth structures that can develop during alloy solidification: planar, cellular and dendritic [17, 19].

Planar solidification occurs when there is a uniform solute concentration ahead of the solidifying front. This, however, is rarely the case in alloy solidification. Consequently, alloys seldom undergo planar solidification except under well-controlled solidification conditions. The instability in the growth rate of the planar interface leads to the formation of protrusions. As the

solid grows, solute is rejected laterally as well as in front of the protrusions. This creates a diffusion field in front of the growing solid. The initial solid that forms is primary α. The rejected solute lowers the local equilibrium solidification temperature and causes recesses to form. The protrusions continue to grow due to a region of constitutional undercooling (undercooling caused by compositional changes) in the surrounding liquid. The tips grow at a faster rate than the depressions since the depressions accumulate the solute pushed by the tips. This growth behavior produces a cellular structure within the melt (Figure 10). Cells grow parallel to the heat flux but in the opposite direction.

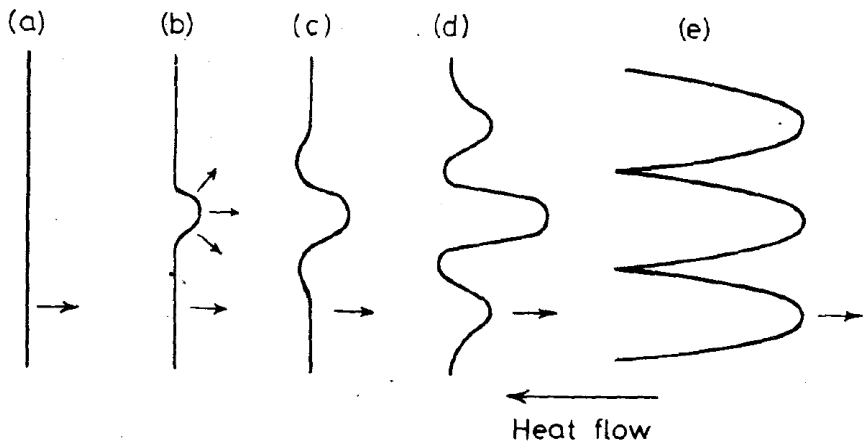

Figure 10. Breakdown of a planar solidification front into cells [17].

If the spacing between cells is sufficiently large, they will develop secondary branches and become dendrites (the name dendrite originates from the Greek word *dendros* meaning tree [17, 19]). While cells grow parallel to the direction of heat flow regardless of the crystallographic direction, dendrites grow in preferred crystallographic directions that are closest to the heat flow (Figure 11). In the case of face-centred cubic (FCC) crystals for example, the preferred dendrite orientations are the <100> family of directions [19]. For an HCP crystal structure, the preferred dendrite orientations are the <0001> family of directions [19].

The growth rate of the dendrite is strongly influenced by the radius of the dendrite tip. A dendrite with a smaller tip radius will grow quicker due to the more efficient solute redistribution. This is because the atoms rejected at the interface of a thin needle have a larger surrounding volume of liquid into which they can diffuse [19].

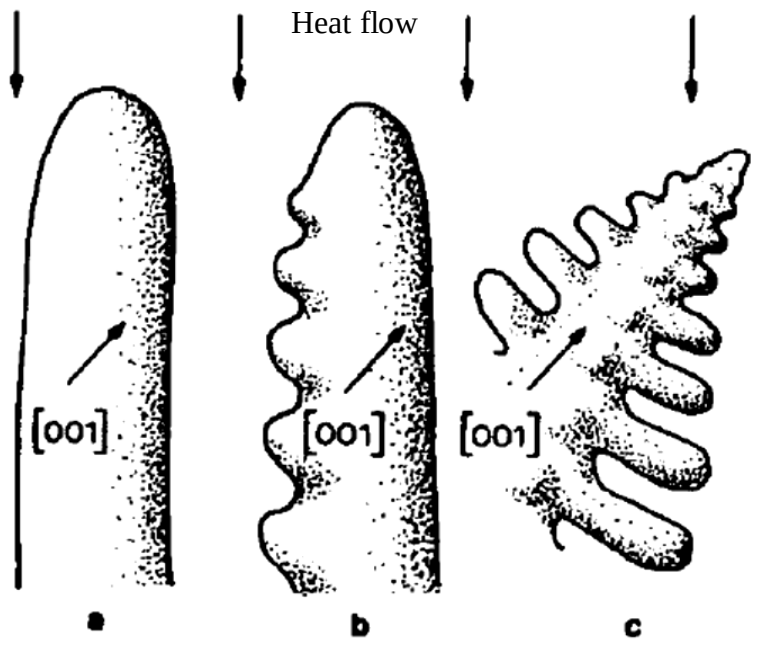

Figure 11. Illustration of a) cell, b) dendritic cell and c) dendrite [19].

The dendrites cease to grow lengthwise when the diffusion fields overlap [17, 19, 20]. The dendrite branches however, continue to thicken [19]. Thin branches may also dissolve and make room for the growth of thicker neighbouring branches.

During the solidification of a casting, three zones are generally present: chill zone, columnar zone and equiaxed zone [17]. These three zones are shown in Figure 12. The chill zone is a consequence of the rapid cooling of the melt at the mould wall. Even if the mould is preheated, the chill zone is still present because the mould wall acts as a heterogeneous nucleation site and thus requires a much lower undercooling for nucleation. Consequently, this region is the first to solidify.

Once the chill zone is developed, some crystals formed in the chill zone may continue to grow dendritically. Their growth is dependent on the orientation of the dendrites and the temperature gradient in the melt. Dendrite arms with the preferred crystallographic direction parallel to the direction of heat flow will outgrow the neighbouring dendrites that are not parallel to the heat flow. This phenomenon is shown in Figure 13. These dendrites are termed columnar dendrites [17, 19].

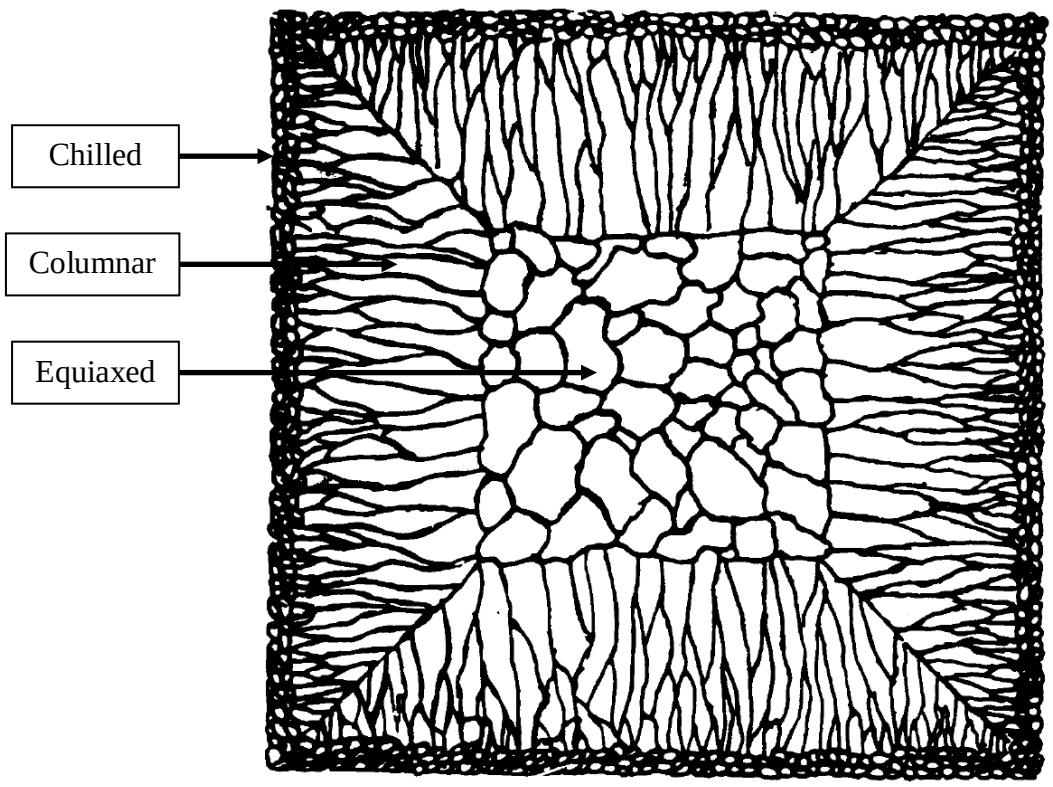

Figure 12. Schematic of a casting illustrating three zones (chilled, columnar, equiaxed) [17].

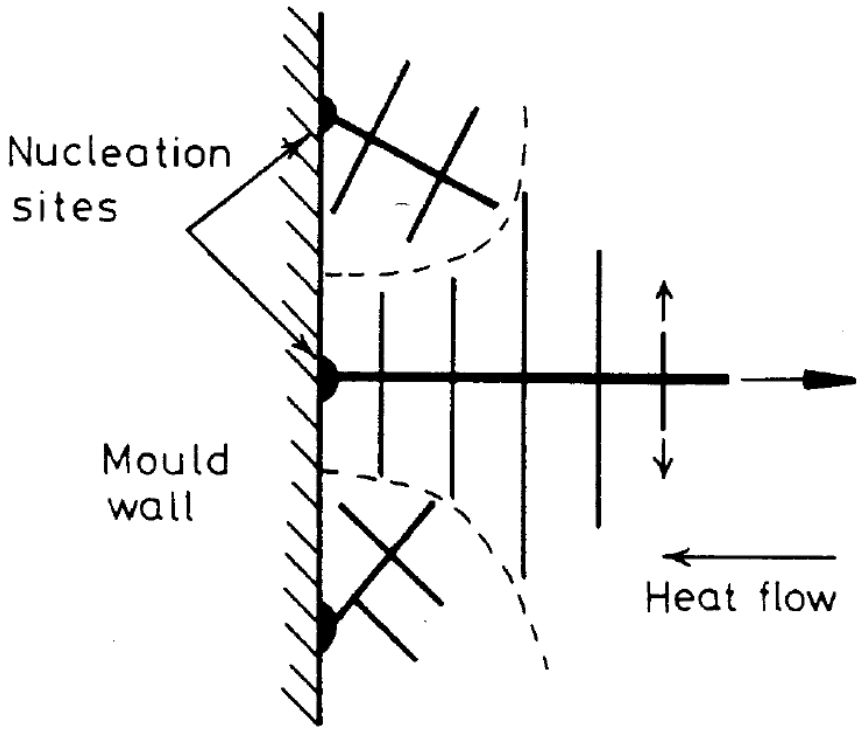

Figure 13. Schematic of dendritic growth at mould wall [17].

When the heat extraction is nearly isotropic, equiaxed dendrites form. Equiaxed dendrites grow along all the available preferred directions (Figure 14). They commonly form by using impurities within the melt as substrates for heterogeneous nucleation. They can also originate from broken dendrite side-branches [19].

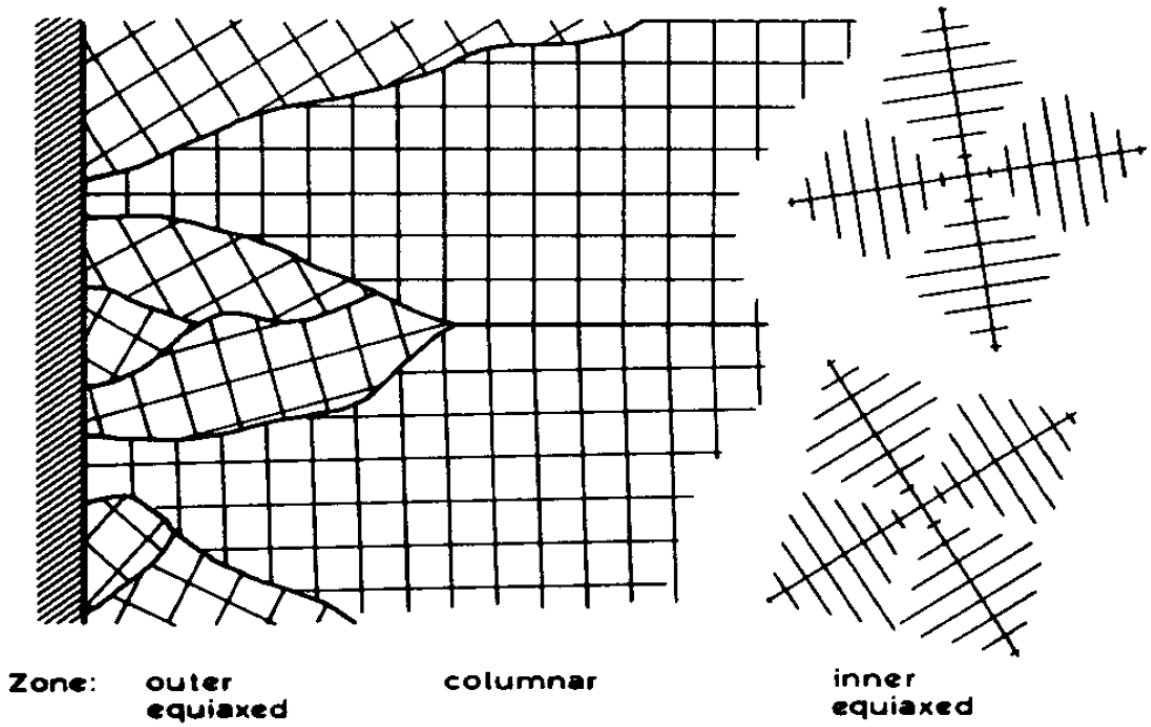

Figure 14. Formation of columnar and equiaxed dendrites [19].

2.3 Dendrite Coherency

As the dendrite arms continue to grow during solidification, there will be an instance when the diffusion fields in front of the dendrite tips overlap. The high solute concentration in front of the dendrite tips will prevent the lengthwise growth of the dendrites. In theory, the dendrite tips should not impinge on each other. However, due to hydrostatic pressures and the effect of the gravitational force, the dendrites are brought into contact to form a dendritic network [20]. The instance at which an interlocking solid network forms during solidification is termed the dendrite coherency point (DCP). The DCP is commonly specified in terms of coherency temperature and coherency solid fraction.

The DCP has a significant impact on the quality of the casting. Once the dendrites become coherent, liquid metal flow is restricted to interdendritic regions. The solid fraction at the DCP for different alloys can be compared to estimate which alloy is more prone to casting defects such as porosity, misruns and hot tears. In theory, an alloy that has a higher solid fraction at the DCP is less prone to casting defects [6].

2.3.1 Influence of Dendrite Coherency on Castability and Casting Defects

Castability is a generic term encompassing liquid metal flow, mold filling and solidification, with minimal defects in the final casting. The castability of the alloy is manifested in the minimal susceptibility of the cast metal to casting defects such as porosity, misruns, and hot tears. An alloy that has poor castability is more prone to casting defects [4, 5].

Porosity is a common casting defect that results from insufficient feeding. As liquid metal flows through the interdendritic regions, the dendrite arms continue to thicken and minimize interdendritic feeding. During solidification, some interdendritic regions become blocked. The blocked interdendritic liquid shrinks as it solidifies, thus causing interdendritic porosity in the casting.

Misruns are another branch of common casting defects that are a consequence of inadequate feeding. Misruns typically occur when liquid metal is fed through a thin section of the casting. If the interdendritic channels feeding this section are blocked, the thin section of the casting will not fill. As a result, the casting will be incomplete.

Hot tears form at the grain boundaries or at the interdendritic regions. As the liquid metal solidifies, the dendrite arms are pulled apart by mechanical stresses resulting from the thermal contraction of the liquid metal. If the interdendritic liquid cannot access the voids developed during thermal contraction, a hot tear will form [10]. As the coherency solid fraction decreases, the casting becomes more susceptible to hot tears since the interdendritic liquid is obstructed at an earlier stage in solidification [5]. Figure 15 shows the dendritic structure for an acetone alloy. The dendritic structure in Figure 15 (a) and (b) is open and allows for interdendritic liquid to

flow freely. The critical region for hot tear formation is just after the DCP (Figure 15c). In this region, the dendrites just begin to coalesce. Because the bonds between dendrite arms are not strong enough to withstand the mechanical stresses imposed by the thermal contraction of the interdendritic liquid, the dendritic network is broken in that particular region.

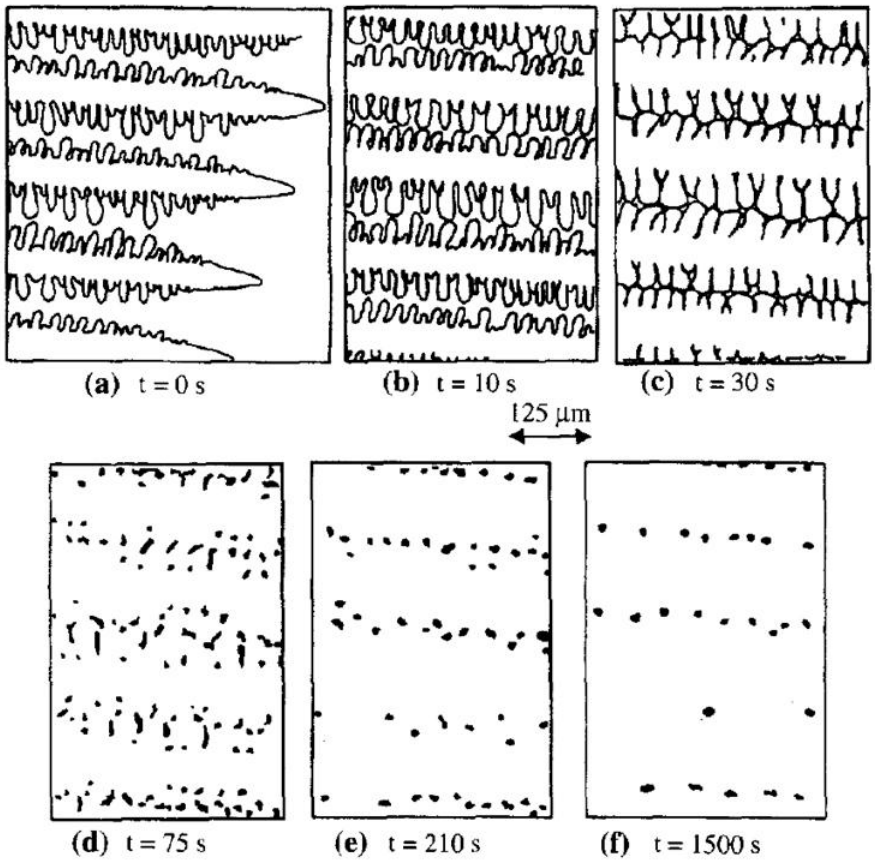

Figure 15. Dendritic structure during solidification at various solid fractions [5].

2.3.2 Techniques to Determine the Dendrite Coherency Point

The importance of the DCP in minimizing casting defects has led to the development of two approaches to determine it: the mechanical analysis approach and the thermal analysis approach. In the mechanical analysis approach, the DCP is determined through the inspection of mechanical changes that occur in the solidifying melt once the dendritic network is established. The thermal analysis approach evaluates changes in the thermal behaviour of the solidifying melt to determine the DCP.

2.3.2.1 Mechanical Analysis

At the DCP, the dendrites interlock thereby increasing the tensile and shear strength of the solidifying melt [7-10, 21]. The dendritic network exhibits solid-like behavior such as the ability to resist and transmit mechanical stresses. The mechanical analysis approach subjects the solidifying melt to a shear stress while constantly monitoring the temperature. Stress and temperature are plotted with respect to time, thereby obtaining two curves: a stress-time curve and a cooling curve. The time during solidification corresponding to a sharp increase in the material's resistance to the applied stress is the coherency time. The temperature on the cooling curve corresponding to this time is the coherency temperature. The coherency temperature and cooling curve can further be used to obtain the coherency solid fraction. The two most popular mechanical methods are the rheological method and the direct shear-cell method.

2.3.2.1.1 Rheological Method

The rheological method uses a viscometer to measure the torque required to rotate a spindle in the crucible with a metal cooling from the molten state [4, 8, 11]. A typical experimental setup for rheological analysis is shown in Figure 16. The spindle is attached to a spring inside the viscometer. The spring is subjected to a torque due to the resistance the spindle experiences as it rotates in the metal slurry. Temperature and torque data from the viscometer and thermocouple are continuously measured and recorded with respect to time. The coherency point is reached when there is a rapid increase in the torque experienced by the spindle (see Figure 17). The rapid increase in torque is due to dendrite arm coalescence that consequently restricts stirrer rotation [11, 20, 22].

Several researchers used the rheological method and found the coherency solid fraction for the AZ91 alloy to be in the range of 0.14 – 0.17 at a cooling rate of 1 °C/s [11, 13]. The DCP can also be determined by analyzing the derivative of the torque plot. This approach is commonly used when there is a significant amount of noise in the data obtained. Gourlay *et al.* [11] analyzed the derivative of the torque curve to determine the coherency point. A sample rheological curve from the experiments of Gourlay *et al.* is shown in Figure 18.

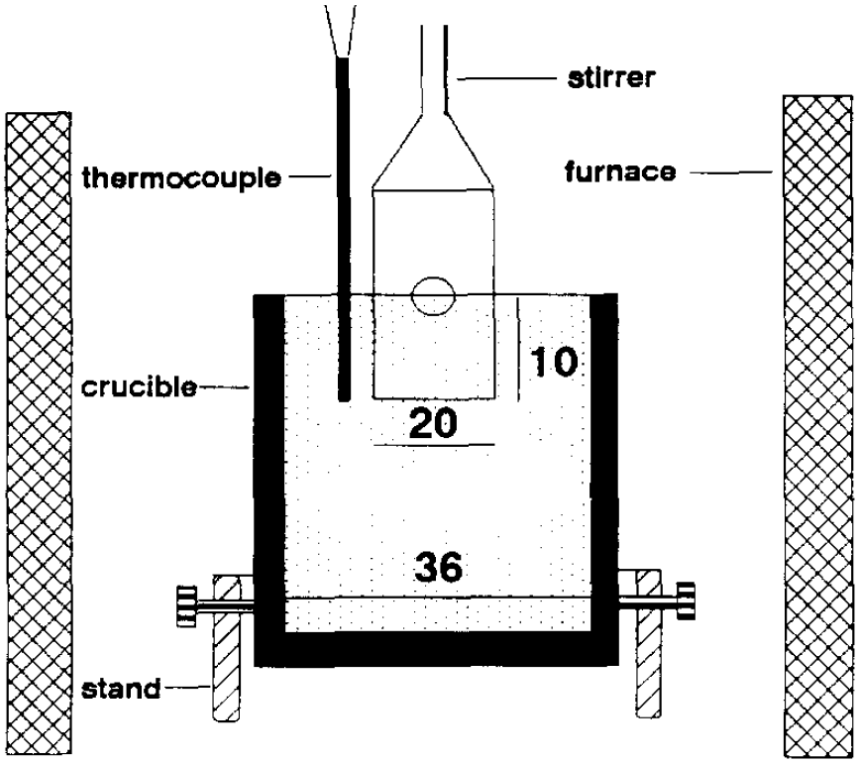

Figure 16. Rheological experimental setup (all units are in mm) [8].

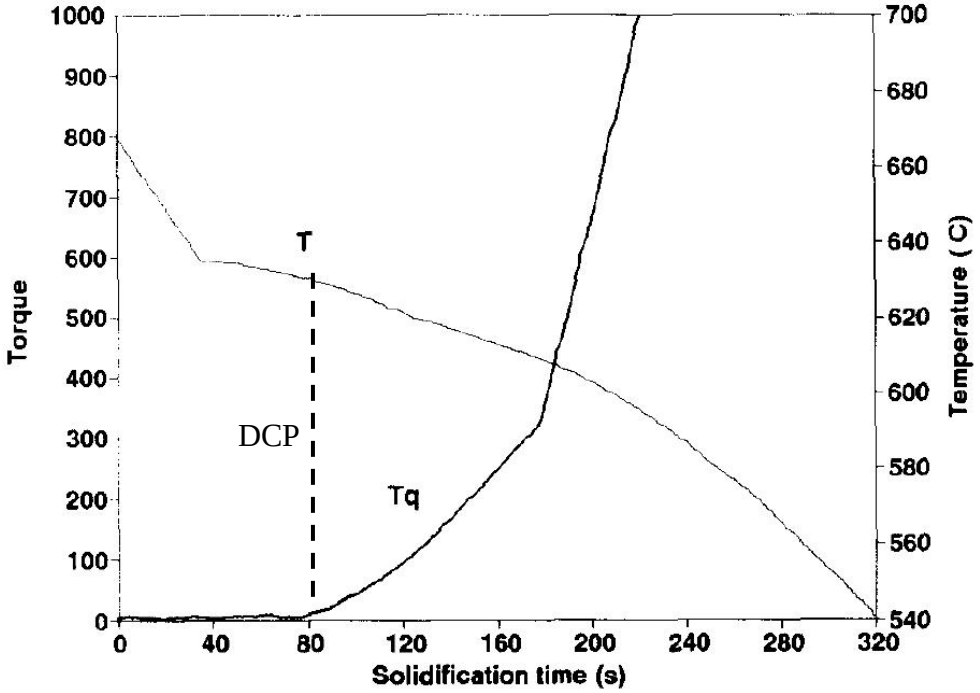

Figure 17. Temperature (T) and torque data (Tq) obtained from rheological experiment on a solidifying Al alloy [8].

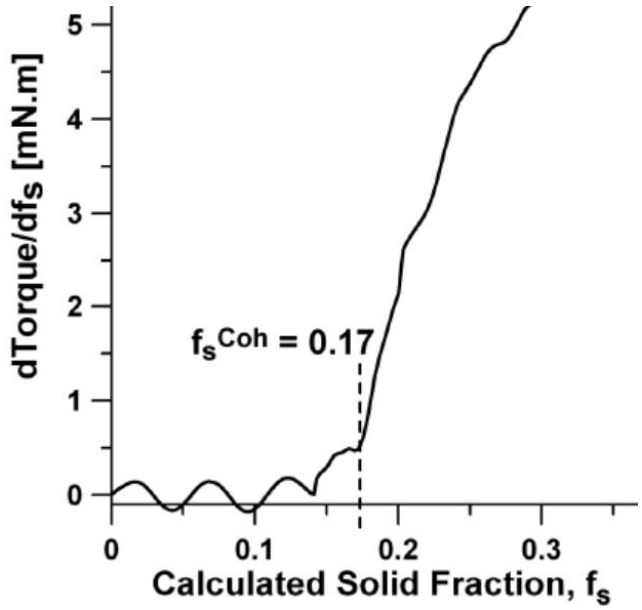

Figure 18. Rheological data for AZ91 magnesium alloy [11].

2.3.2.1.2 Direct Shear-Cell Method

The direct shear-cell method involves applying a shear stress along a horizontal cross-section of a sample [7]. A direct shear-cell apparatus is shown in Figure 19. The sample is sheared by the horizontal movement of the shear ring at a constant rate in isothermal conditions. The force required to shear the melt is constantly monitored, along with the temperature. At the DCP, there is a sharp increase in the force required by the pulling arm to deform the solidifying sample. The temperature corresponding to this sharp increase in force is the coherency temperature.

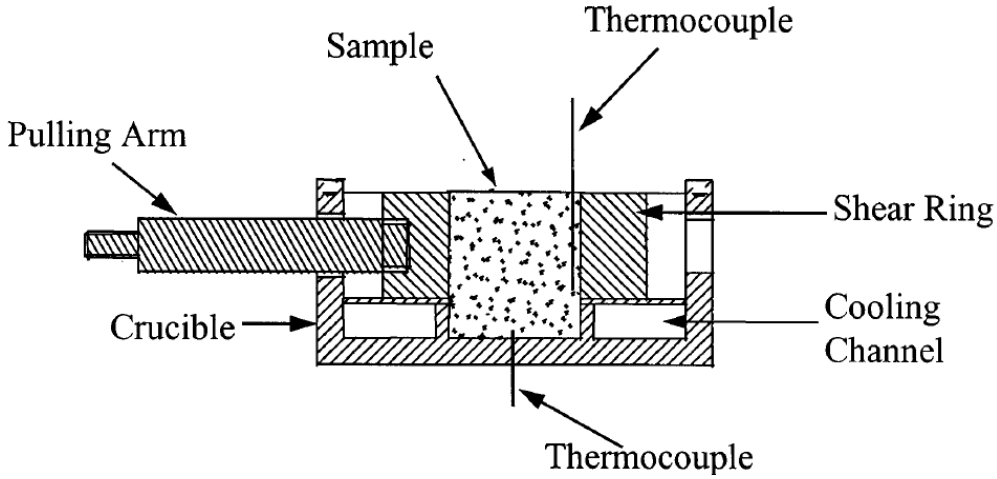

Figure 19. Schematic of shear-cell. Crucible has 50 mm diameter and 55 mm depth [7].

2.3.2.2 Thermal Analysis

At the DCP, the thermal conductivity of the solidifying melt significantly increases due to the formation of a solid network which has a higher thermal conductivity than that of the liquid metal [15, 23]. The thermal analysis approach relies on this change in conductivity to determine the temperature and solid fraction at the DCP. There are two main thermal analysis methods used to determine the DCP of the material: the one-thermocouple method and the two-thermocouple method.

2.3.2.2.1 One-Thermocouple Method

For the one-thermocouple method, a single thermocouple located in the centre of the solidifying melt is used to determine the DCP. The increase in thermal conductivity of the solidifying melt at the DCP causes an increase in the solidification rate. The minimum value in the second derivative of temperature with respect to time (d^2T/dt^2) corresponds to the instance that a significant change occurs in the thermal conductivity of the melt. This point is circled in Figure 20 and represents the DCP. The corresponding temperature on the cooling curve (T_C) is the coherency temperature.

2.3.2.2.2 Two-Thermocouple Method

For the two-thermocouple method, one thermocouple records the temperature at the centre of the melt (T_C) while the other records the temperature near the inner mould wall (T_W). At the DCP, the increase in thermal conductivity leads to a reduction in the temperature difference (ΔT) between these two thermocouples [15, 23-25]. Therefore, using two thermocouples, the DCP can be found from the plot of temperature difference (ΔT) vs. time (t). The coherency point corresponds to the largest temperature difference after nucleation. Once the DCP is reached, the conductivity in the melt increases and, consequently, there is a decrease in the temperature difference. The DCP is circled in Figure 21. The corresponding temperature (T_C) is the coherency temperature.

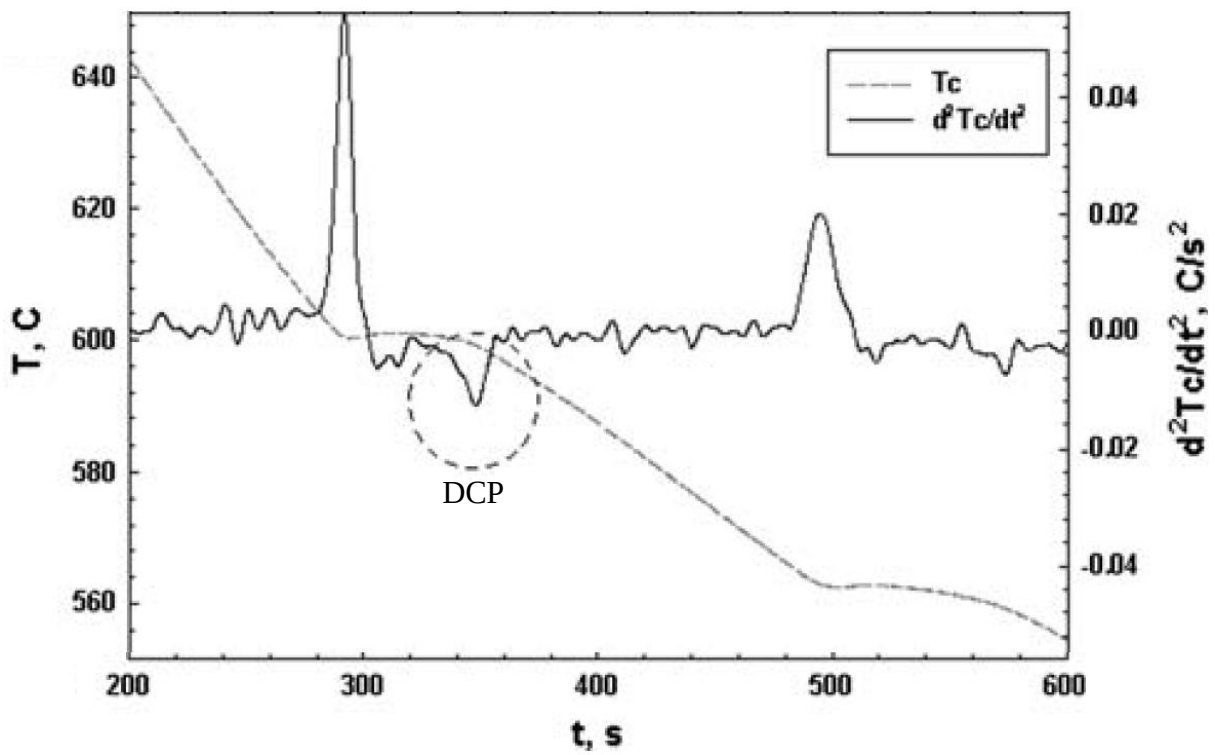

Figure 20. Thermal analysis for one-thermocouple method [23].

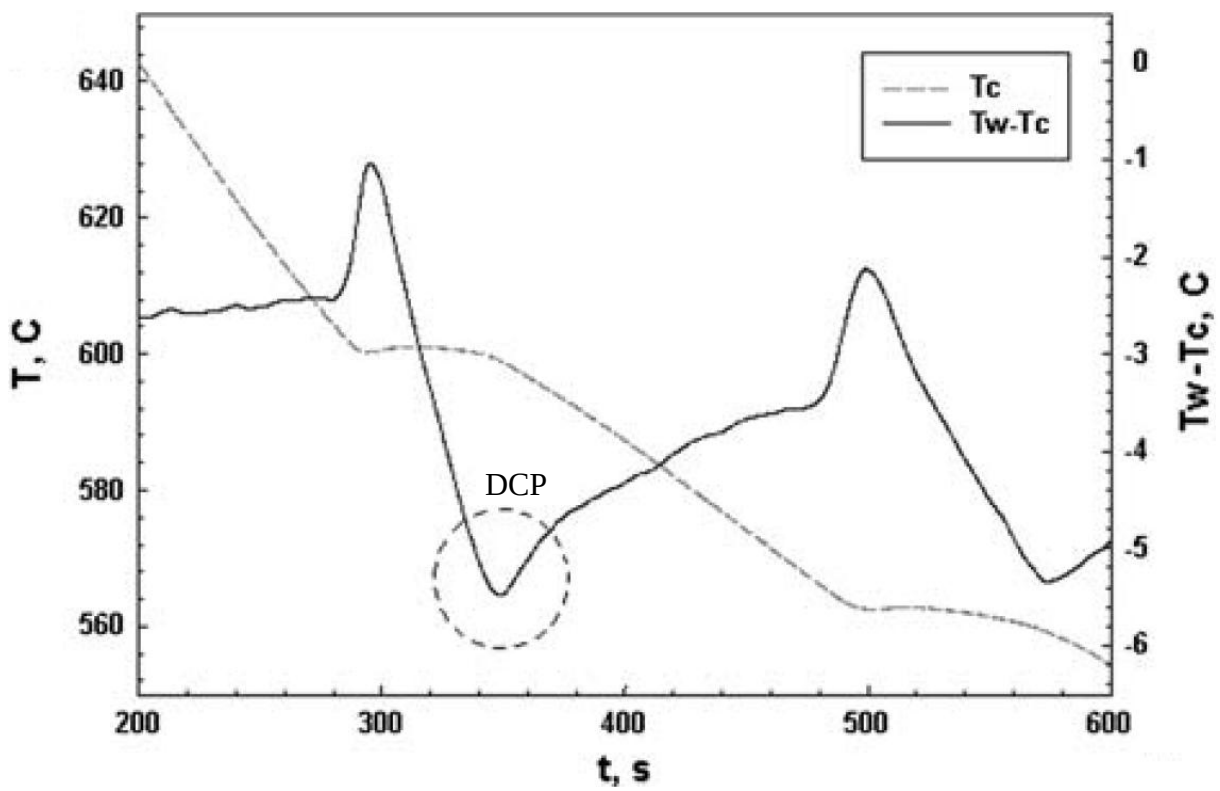

Figure 21. Thermal analysis for two-thermocouple method [23].

2.3.2.3 Comparison of Methods

The mechanical analysis approach is a direct method of detecting the DCP, whereas the thermal analysis approach is used to indirectly determine the DCP. A major advantage of the thermal analysis approach is that it is simple and far less intrusive. The thermal analysis approach however was found to generally produce significantly different results in comparison to the continuous torque methods [13, 15, 25]. Since the rheological approach determines the DCP directly, it is considered to be the superior method to accurately determine the DCP.

2.3.3 Factors Affecting the Dendrite Coherency Point

2.3.3.1 Effect of Cooling Rate

Different cooling rates can be obtained by altering the conditions under which the crucible cools. The crucible can be left to cool within the furnace for one scenario and cooled with compressed air for a different setting [26]. Insulation can be used to cover the crucible in order to reduce the cooling rate. The cooling rate of the molten metal has a significant effect on the DCP. The cooling rate of the melt is proportional to the dendrite growth rate [8]. An increase in dendrite growth rate subsequently leads to an earlier impingement of the dendrites. The formation of a dendritic network at an earlier stage in solidification results in a decrease in the solid fraction at the DCP. Consequently, the cooling rate is inversely proportional to the coherency solid fraction. The effect of cooling rate on the coherency solid fraction (determined using rheological method) for an Al alloy is shown in Table 1.

Table 1. Effect of cooling rate on coherency solid fraction in Al alloy 355 [8].

Cooling Rate [^{o}C/s]	Coherency Solid Fraction [%]
0.3	13-17
1	12-15
3	9-12

The secondary dendrite arm spacing (SDAS) decreases with increasing cooling rate, making the dendritic structure more branched (Figure 22). This phenomenon is a consequence of the decreased time for lateral diffusion with increasing cooling rate [17, 19]. Figure 23 shows the trend in SDAS with varying cooling rate for an $AlSi_7Cu_2$ (Al – 7 wt.% Si – 2 wt.% Cu) alloy. At the highest cooling rate, the dendritic structure was fine and the SDAS was minimal (~37 µm). When the sample was cooled at the lowest cooling rate, the SDAS was the largest (~87 µm). The SDAS has a strong influence on the tensile properties of the alloy. The ultimate tensile strength (UTS) increases with decreasing SDAS (Figure 23).

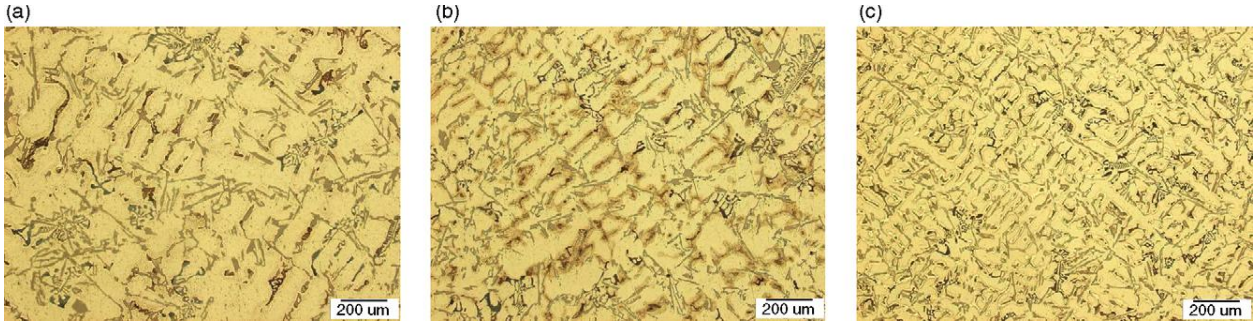

Figure 22. Micrographs showing the microstructures of $AlSi_7Cu_2$ that solidified: (a) 0.16 °C/s, (b) 0.46 °C/s, (c) 0.72 °C/s [22].

The increased growth rate and earlier dendrite coalescence at higher cooling rates also produce shorter primary dendrite arms. In the case of equiaxed dendrites, the grain radius is equal to the length of the primary dendrite arm [27]. As a consequence, an increase in the cooling rate corresponds to a finer grain structure (Figure 23).

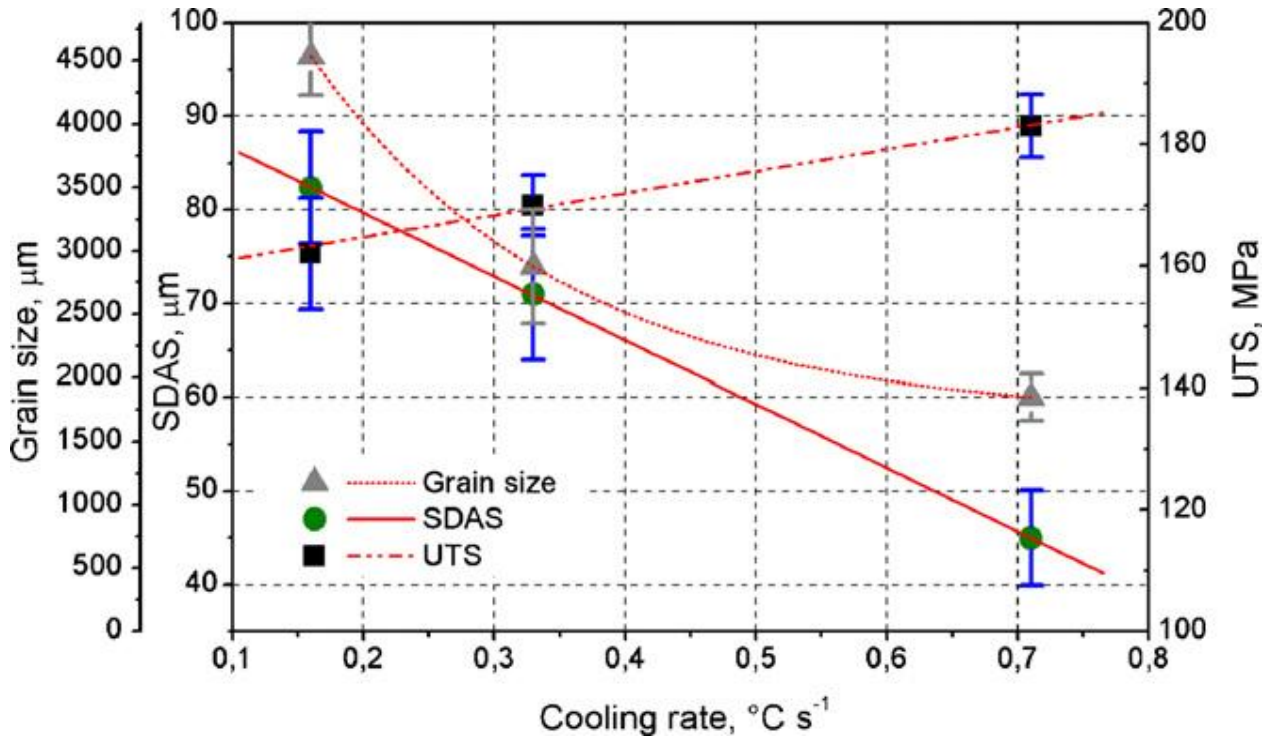

Figure 23. Cooling rate effect on grain size, SDAS and UTS of an $AlSi_7Cu_2$ alloy [22].

2.3.3.2 Effect of Alloying

The solubility of the alloying elements in the liquid state is higher relative to that in the solid state. As a consequence, there is a rejection of the alloying elements by the solidifying front. The rejected alloying elements create a diffusion layer in front of the dendrite arms. The thickness of the diffusion layer δ_c is given by

$$\delta_c \sim D/V \tag{5}$$

where D is the diffusion coefficient in the liquid and V is the dendrite growth rate [20]. The higher solute concentration of the diffusion layer causes the liquid in front of the dendrite to exist below its equilibrium freezing temperature. This phenomenon is known as constitutional undercooling. Further alloying additions increase the diffusion layer thickness and consequently lower the dendrite growth rate [17, 20].

The influence of alloying additions on the dendrite growth rate is measured by the growth restriction factor (GRF). The GRF is given by

$$GRF = m(k-1) \tag{6}$$

where m is the slope of the liquidus line and k is the equilibrium partition coefficient [28]. Values of GRF for typical alloying elements in magnesium are listed in Table 2.

Table 2. Values for m, k and GRF for various alloying elements in magnesium [28].

Element	m	k	GRF
Zr	6.90	6.55	38.29
Ca	-12.67	0.06	11.94
Si	-9.25	≈ 0.00	9.25
Ni	-6.13	≈ 0.00	6.13
Zn	-6.04	0.12	5.31
Cu	-5.37	0.02	5.28
Ge	-4.41	≈ 0.00	4.41
Al	-6.87	0.37	4.32
Sc	4.02	1.99	3.96
Sr	-3.53	0.006	3.51
Ce	-2.86	0.04	2.74
Yb	-3.07	1.17	2.53
Y	-3.40	0.50	1.70
Sn	-2.41	0.39	1.47
Pb	-2.75	0.62	1.03

The growth restricting effect of solute in the solvent seems to be additive in nature for low alloying levels [29]. An alloying addition with a high GRF should cause a greater decrease in the dendrite growth rate when compared to an alloying addition with a low GRF. There is a saturation level, however, above which further alloying additions do not affect the dendrite growth rate. For example, previous researchers observed that the dendrite growth rate decreased

with the addition of Al to Mg alloys for levels up to 5 wt.% Al. Levels beyond 5 wt.% Al in Mg alloys had a negligible effect on the dendrite growth rate [28].

Generally, the reduced dendrite growth rate caused by the increase in GRF should delay the DCP and consequently increase the coherency solid fraction. However, this is not always the case. If the element added leads to the formation of a new phase at a temperature below the coherency temperature, there may be less liquid metal solidified at the instance the DCP is reached. This phenomenon would consequently correspond to a lower coherency solid fraction. An example of such a phenomenon is seen when adding calcium (Ca) to Mg alloys. Liang et al. [15] found that the addition of Ca to Mg alloys caused a decrease in the solid fraction at the DCP, even though Ca had a growth restricting effect on Mg. Table 3 shows the change in the DCP solid fraction with the addition of Ca in the AZ91 alloy. The addition of Ca led to the formation of a new phase (Al_2Ca) before the eutectic reaction at approximately 483 ^oC for 1.03 wt.% Ca and at 514 ^oC for 2.05 wt.% Ca addition [15]. The coherency temperature was 584 ^oC with 1.03 wt.% Ca and 580 ^oC with 2.05 wt.% Ca. In both instances, the phase formed below the coherency temperature. Consequently, there was a substantial decrease in the coherency solid fraction as Ca was added to AZ91 alloy.

Table 3. Thermal analysis results for the coherency solid fractions for AZ91 alloy at various Ca levels [15].

Alloy	Coherency Solid fraction [%]
AZ91	50
AZ91 + 1.03 wt.% Ca	32
AZ91 + 2.05 wt.% Ca	25

2.3.3.3 Effect of Grain Refiner Addition

Magnesium alloys contain a limited number of active nucleating particles to initiate solidification [30]. A high degree of undercooling is required to initiate solidification in unrefined Mg alloys due to the poor nucleating strength of these particles [22]. An easier way to obtain effective nucleating particles is through the addition of grain refiners [30]. Grain refiners are commonly

used in the industry to improve the mechanical properties and castability of alloys. No research has been found with the focus of studying the effect of grain refiner addition on the dendritic structure, DCP, and castability of Mg alloys.

Grain refiners introduce active nucleating particles in the melt, thereby promoting heterogeneous nucleation. For heterogeneous nucleation to initiate there must be a low planar disregistry, typically less than 10%, between the potential nucleant and the crystal being formed. Ti-B compounds are suitable grain refiners in Mg-Al alloys due to a planar disregistry of 5.6% [18].

A sufficient number of potent nuclei may not be enough to achieve effective grain refinement, since the final grain size is determined by the subsequent growth rate of α-Mg crystals. A decrease in the growth rate of the α-Mg dendrites will produce a refined grain structure [27]. The decrease in growth rate may be achieved through the segregation of solute elements, like titanium, to the solid-liquid interface. The segregated solute elements create a constitutionally undercooled zone in front of the growing dendrite arm [29, 31]. The GRF of the grain refiner in the solvent is proportional to the segregating power of the element. Furthermore, the growth rate of the dendrites in grain refined alloys is also lower because of the larger specific surface area of the solid [20]. Wang *et al*. [18] noticed grain refinement of Mg-Al alloys through the addition of Ti-B compounds and attributed this to the high segregating power of the grain refiner. Elsayed [32] studied the effect of Al-5Ti-1B (TIBOR) grain refiner addition to AZ91E magnesium alloy and observed a reduction in grain size of 61% at the 0.005 wt.% Ti level.

The solid fraction at DCP through the addition of grain refiner cannot be estimated based on the decreased dendrite growth rate alone. The increase in nucleation sites corresponds to a shorter path for dendrites to travel before interlocking. If there is not a substantial decrease in growth rate, a smaller grain size can cause a decrease in the coherency solid fraction [20]. Dahle *et al.* [20] studied TIBOR grain refiner in two aluminum alloys (Al – 7 wt.% Si and Al – 11 wt.% Si) and noticed a significant improvement in the coherency solid fraction. In Al – 7 wt.% Si alloy, the coherency solid fraction increased from 17 to 25% with an addition level of 0.10 wt.% Ti. In Al – 11 wt.% Si alloy, the solid fraction at DCP increased from 9 to 13% with an addition level of 0.09 wt.% Ti.

2.4 Chapter Summary

The general microstructure and common defects associated with AZ91 alloy castings were presented. A brief background on the nucleation and growth processes in casting was provided. The relation between the dendrite coherency point (DCP) and casting defects was then analyzed. Further, two main approaches to determine the DCP (rheological method and thermal analysis method) were discussed in detail. Finally, the influence of cooling rate, alloying and grain refiner addition on the DCP was discussed.

At present, the coherency solid fraction for AZ91 has been studied using the rheological method. However, there was no research found on the effect of grain refinement to the dendritic structure, DCP, and porosity of AZ91 alloy. In view of this, the purpose of this thesis is to:

1) Optimize the experimental procedure to accurately detect the DCP in AZ91 alloy.
2) Analyze the effects of TIBOR grain refiner on the microstructure and dendritic morphology of AZ91E alloy.
3) Determine the DCP in AZ91E alloy and study the effect of grain refinement, through the addition of TIBOR, on the DCP.
4) Analyze changes in the porosity of the castings that were a consequence of changes in the DCP and coherency solid fraction.

CHAPTER 3. OPTIMIZATION OF RHEOLOGICAL EXPERIMENT

The experimental procedure for the rheological method had to be optimized before the experiments could be performed on AZ91E magnesium alloy, to ensure accurate and significant results. A319 aluminum alloy was used to perform the rheological experiments to optimize the procedure. A319 alloy was chosen since it is commonly used in the casting industry and has a liquidus temperature close to that of AZ91E. Aluminum also does not continuously oxidize as magnesium, and thus it was the ideal material for optimizing the rheological parameters. Virgin ingots of A319 alloy were used for each experiment. The chemical composition of the as-received A319 alloy is provided in Table 4.

Table 4. A319 alloy composition (wt.%).

Cu	Mn	Mg	Fe	Si	Ni	Zn	Ti	Others	Al
3.65	0.31	0.01	0.47	6.15	0.01	0.71	0.14	0.5	Bal.

3.1 Experimental Setup

The experimental apparatus and setup for the rheological analysis are shown in Figure 24 and Figure 25 respectively. A viscometer (Brookfield DV-II+ Pro) was used for torque measurements. The thermocouple and viscometer were connected to a data acquisition system to record temperature and torque data with time. Torque readings were recorded every second, while temperature readings were recorded every 1/6th second. Temperature and torque data were continuously measured and recorded. Torque and cooling curve plots were then constructed from the recorded data.

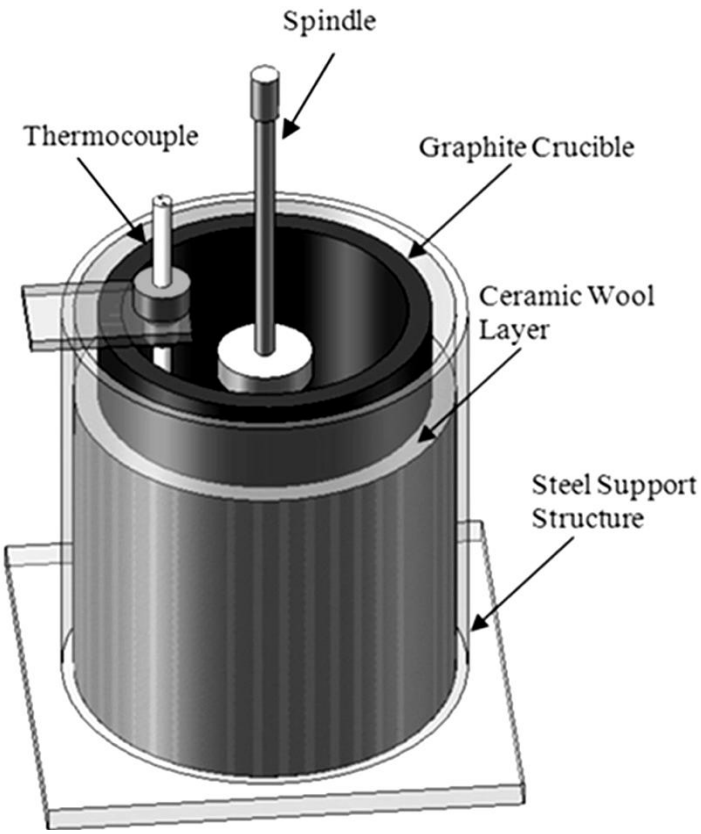

Figure 24. Schematic of apparatus used for rheological experiments.

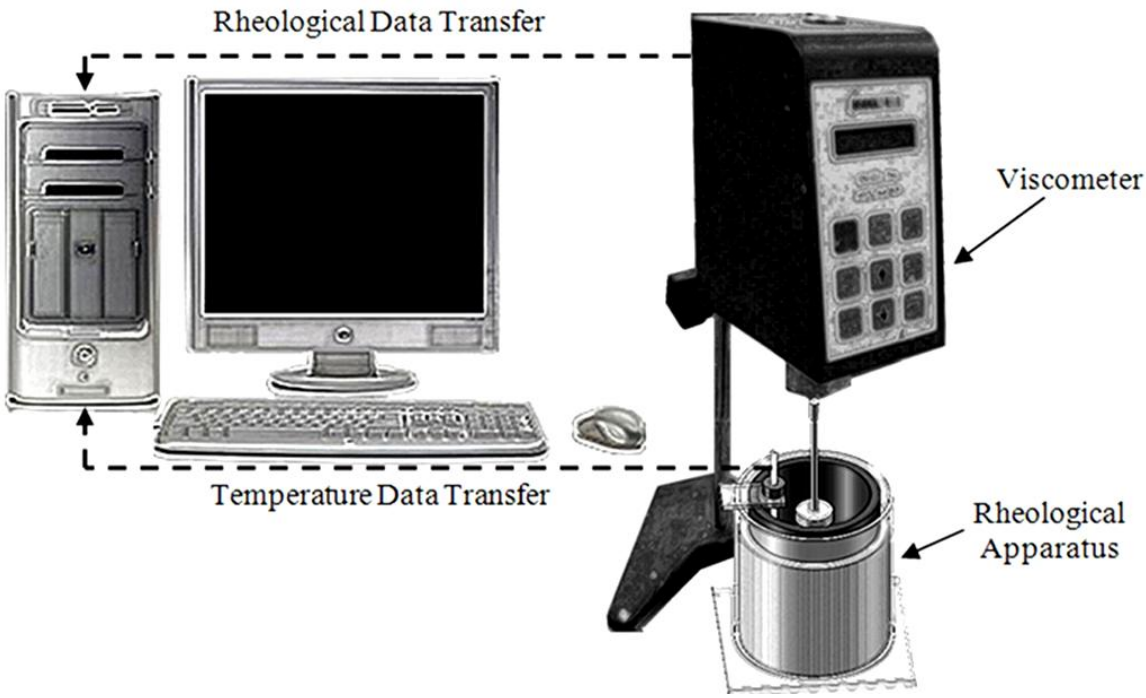

Figure 25. Schematic of experimental setup for rheological experiments.

3.2 Control of Cooling Rate

For the rheological experiments, it was important to maintain the same cooling rate for each experiment to remove the effect of cooling rate fluctuations on the DCP. To maintain a constant cooling rate, an identical mass of 550 g was used for each charge. The A319 alloy was melted in a graphite crucible inside an electric furnace. A layer of ceramic wool was used to insulate the graphite crucible to decrease the cooling rate. A low cooling rate was necessary to obtain an accurate coherency temperature and minimize the formation of columnar dendrites at the crucible wall. A cooling rate of 0.25 °C/s was maintained for each experiment. The dimensions of the crucible are shown in Figure 26. Once the charge reached 700 °C, the crucible was removed from the furnace and placed at the viscometer location. At this point, the temperature and rheological acquisition system was started.

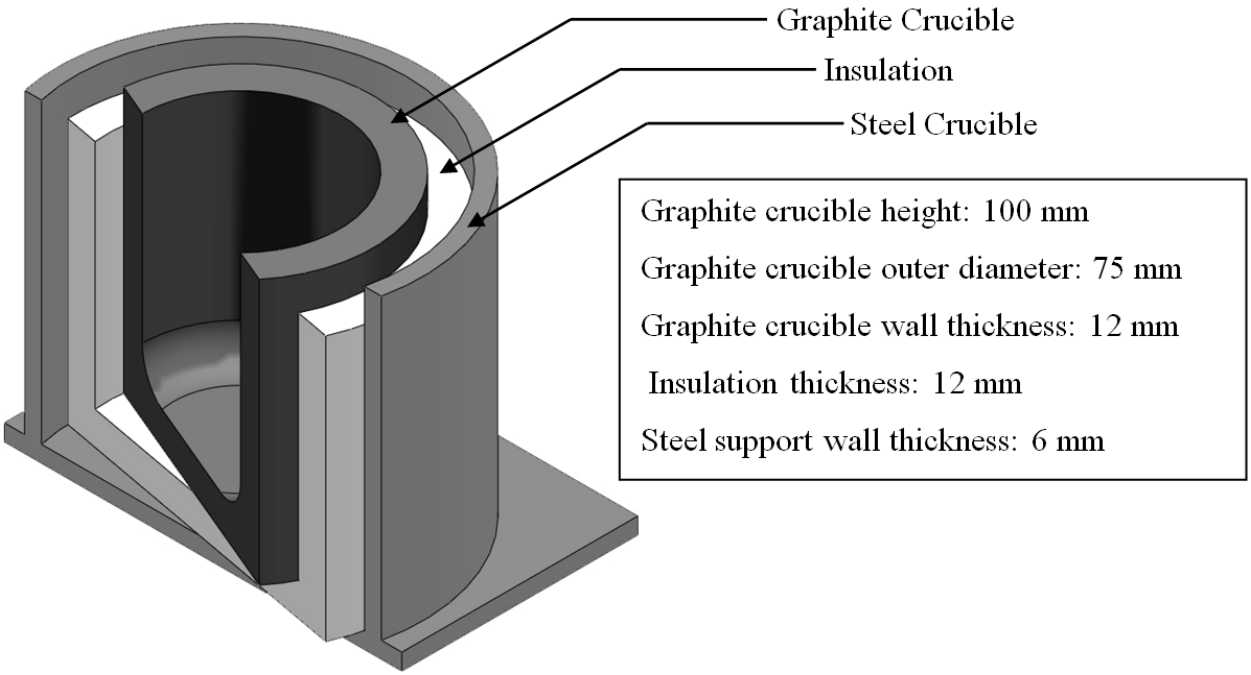

Figure 26. Crucible dimensions for rheological experiments.

3.3 Control of Spindle Rotation Speed

Spindle Speed: 5 RPM

The spindle rotation speed of the viscometer must be established for the rheological experiments. If the spindle speed is too high, the dendrite arms will break and consequently delay the DCP. The initial test conducted on A319 alloy used a spindle speed of 5 RPM.

The rheological data and cooling curve for A319 alloy at a spindle speed of 5 RPM is shown in Figure 27. At a spindle speed of 5 RPM, there was significant fluctuation in the torque values. The instance when there was a sudden increase in torque was taken as the DCP. The temperature corresponding to the DCP was labeled as the dendrite coherency temperature (DCT). The values for the liquidus temperature and DCT obtained from this experiment were approximately 610 °C and 585 °C respectively.

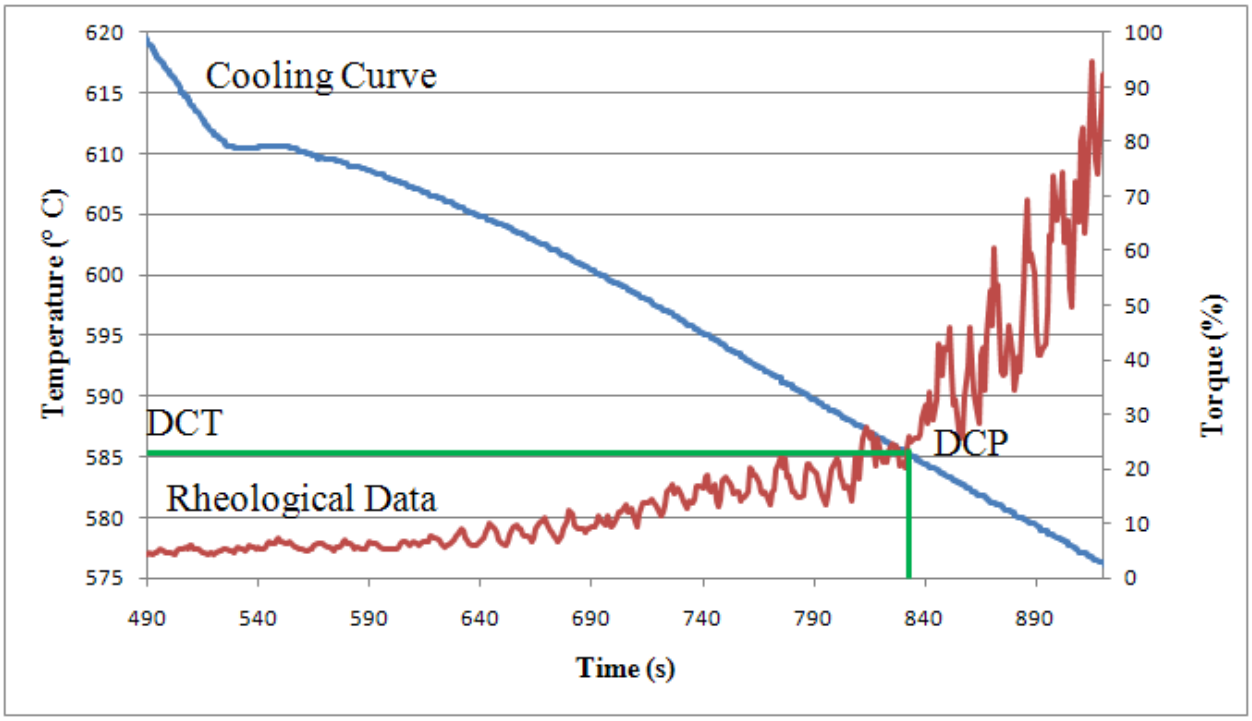

Figure 27. Rheological data and cooling curve for A319 alloy with 5 RPM spindle speed.

To determine whether the spindle rotation speed influenced the DCP, the DCT was compared to that obtained from dendrite coherency experiments performed on A319 by other researchers at a similar cooling rate. For an A319 alloy, the liquidus and DCT from literature were 609 °C and 605 °C respectively [33]. The DCT determined from this test was significantly lower as compared to the DCT found in literature. This decrease in the DCT was due to the breakage of dendrite arms by the spindle rotation, thus shifting the instance the dendrite arms coalesce to a lower temperature.

Spindle Speed: 1 RPM

In light of the rheological results obtained for A319 alloy at a spindle speed of 5 RPM, the rotation speed was decreased to 1 RPM with a view to eliminating the delay in the DCP caused by the spindle rotation. The results from this test are shown in Figure 28. At a 1 RPM spindle speed, there was a significant decrease in the fluctuation of the torque values. The liquidus and DCT were approximately 610 °C and 605 °C respectively, which are close to the values found in literature.

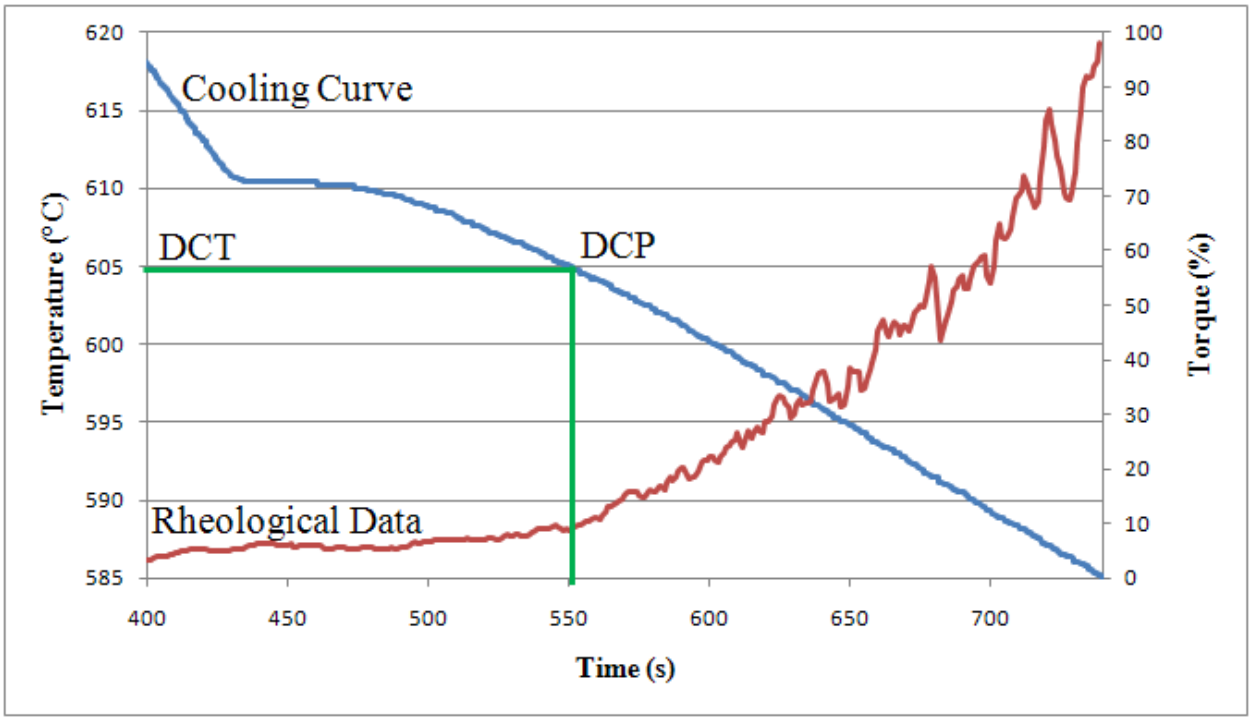

Figure 28. Rheological data and cooling curve for A319 alloy with 1 RPM spindle speed.

Spindle Speed: 0.5 RPM

A spindle speed of 0.5 RPM was also tested, to determine whether the fluctuations in the torque readings can be further decreased. The results of this test are shown in Figure 29. It was observed that the torque values fluctuated least at a spindle speed of 0.5 RPM. The liquidus and DCT were 609 °C and 604 °C respectively, which are close to the values obtained from the 1 RPM test and found in literature. Consequently, a rotation speed of 0.5 RPM was the ideal spindle speed for the rheological experiments.

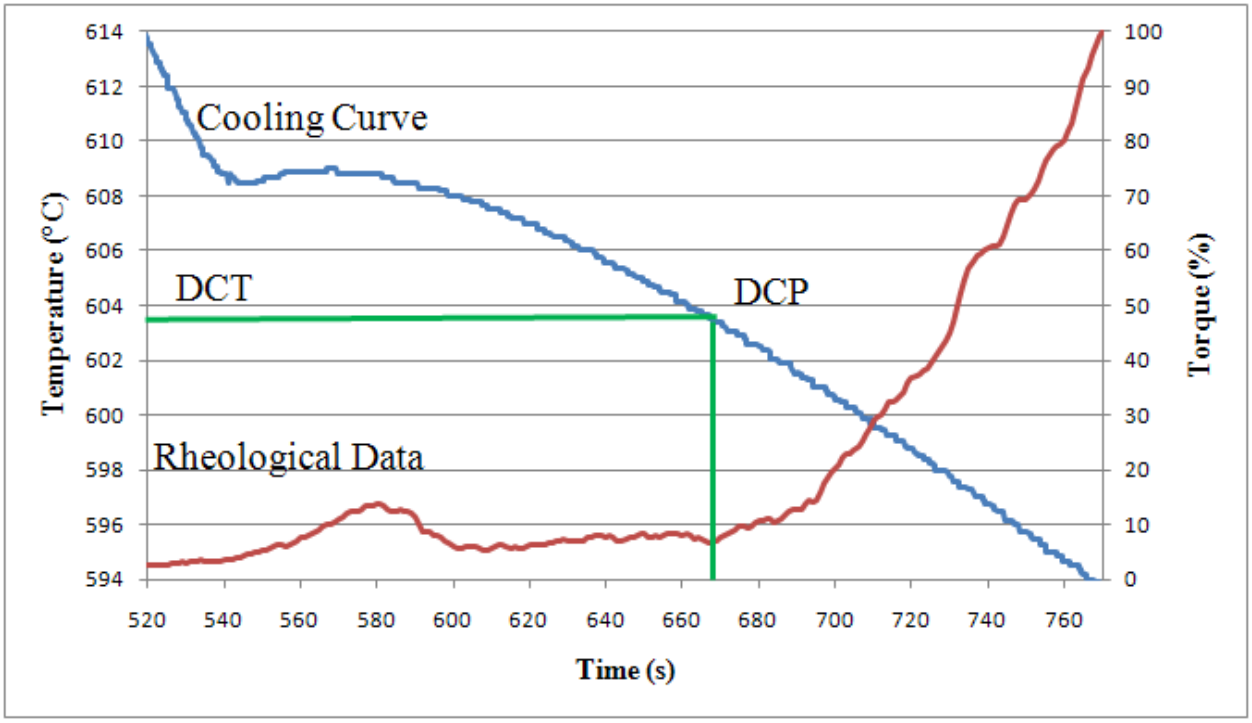

Figure 29. Rheological data and cooling curve for A319 alloy with 0.5 RPM spindle speed.

3.4 Control of Spindle Temperature

From the rheological test performed at a rotation speed of 0.5 RPM (Figure 29), an increase in torque was detected at approximately 560 seconds. Thirty seconds thereafter, the torque decreased and stayed almost asymptotic to the x-axis until the DCP was reached. This increase in torque at the 560 second mark was likely due to the liquid metal solidifying on the spindle, thus

increasing resistance to the stirrer rotation. Once the spindle reached the same temperature as the melt, the solidified metal that once restricted the rotation of the stirrer may have re-melted (around the 590 second mark) and consequently the torque readings decreased.

To prevent the spindle from acting as a chill and promoting the solidification of liquid metal on the spindle upon insertion, the viscometer spindle was preheated with a torch until the spindle changed color to bright red, indicating that it was approximately 800 °C [34]. Two tests were performed using a preheated spindle at a rotation speed of 0.5 RPM. The first plot is shown in Figure 30. When the spindle was preheated, no significant increase in torque was observed until the DCP was reached. Similar results were seen for the second test (Figure A.1.1).

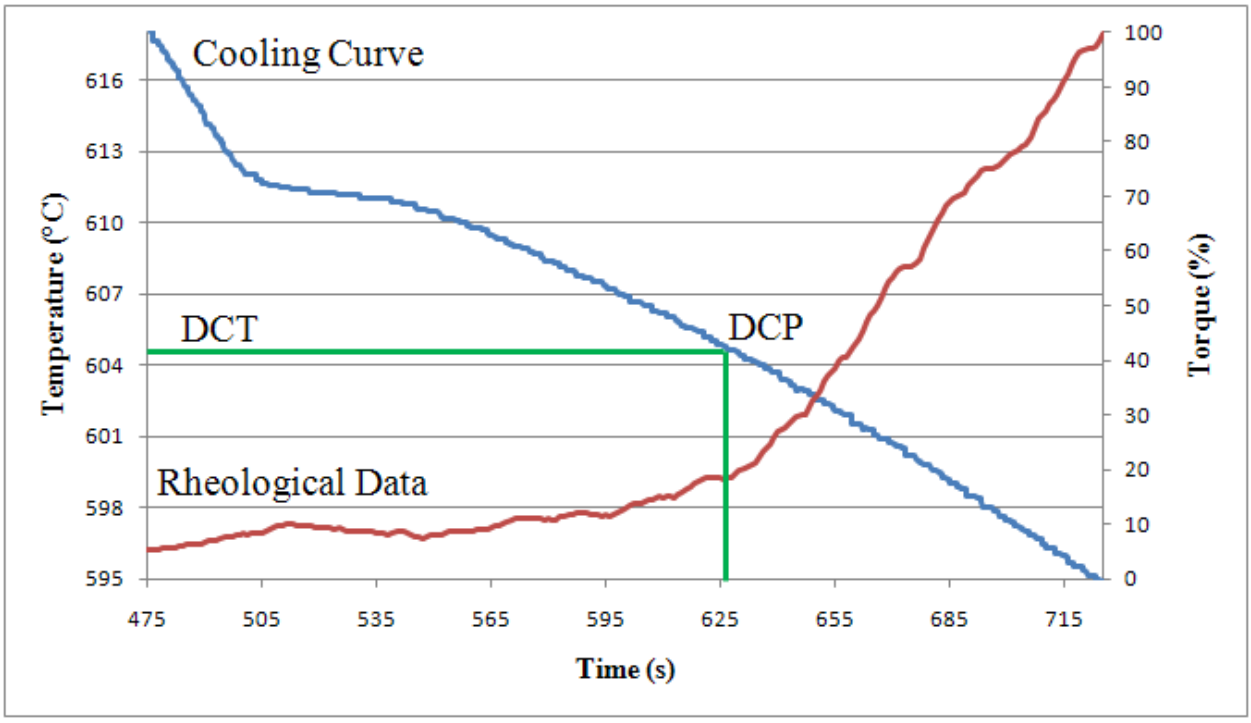

Figure 30. Rheological data and cooling curve for A319 alloy with preheated spindle at 0.5 RPM spindle speed.

3.5 Summary of Rheological Experiments

A summary of the experiments performed on A319 alloy along with the respective liquidus temperature and DCT obtained from each test are provided in Table 5. From the optimization experiments, it was concluded that a preheated spindle with a rotation speed of 0.5 RPM should be used for the rheological experiments on AZ91E magnesium alloy.

Table 5. Rheological experiments performed on A319 alloy.

Trial	Condition	Liquidus Temperature [°C]	Coherency Temperature [°C]
1	Non-preheated spindle at 5 RPM rotation	610	585
2	Non-preheated spindle at 1 RPM rotation	610	605
3	Non-preheated spindle at 0.5 RPM rotation	609	604
4	Preheated spindle at 0.5 RPM rotation	611	605
5	Repeat with preheated spindle at 0.5 RPM rotation	608	603

CHAPTER 4. EXPERIMENTAL PROCEDURE

The experimental procedure comprised of four sections. First, determination of the DCP by the rheological method is outlined. In the next section, the procedure for the quench experiments is described. The third section describes the methods used to prepare the quenched and rheological samples for microscopy analysis. Finally, the fourth section outlines the procedure used to determine the effect of grain refiner addition on the porosity.

4.1 Rheological Experiments

The procedure for the rheological experiments was comprised of three stages: pre-melting, melting, and post-melting. Using the rheological and thermal acquisition systems, the DCP and dendrite growth rate were obtained. The Ti addition levels investigated were 0.005, 0.05, 0.10, 0.20, and 0.30 wt.%. A minimum of three experiments per addition level along with ANOVA (analysis of variance) tests were performed in order to ensure the statistical significance of the results and conclusions. The null hypothesis for the ANOVA tests was rejected if $P_{\alpha max}$ was greater than 99%, thus indicating that there was a significant change in the dendrite growth rate and DCP with varying Ti addition level. After rheological measurements, samples were taken from the castings for microscopy analysis.

4.1.1 Pre-Melting Procedure

Virgin ingots of AZ91E were used for each experiment. The chemical composition of the as-received AZ91E alloy is provided in Table 6. The composition of the as-received Al-5Ti-1B (TIBOR) master alloy used for Ti additions is shown in Table 7.

Table 6. AZ91E alloy composition (wt.%).

Mg	Al	Zn	Mn	Si	Cu	Fe	Ni	Other
90.18	8.7	0.53	0.23	0.05	0.006	0.003	0.0008	< 0.3

Table 7. Al-5Ti-1B master alloy composition (wt.%).

Al	Ti	B	Fe	Si	V	Others
93.73	5	1	0.1	0.06	0.01	< 0.1

The total mass of each charge was 320 g. Identical mass for the charge in each experiment was crucial to ensure the same (constant) cooling rate. A cooling rate of 0.25 °C/s was maintained for each experiment to remove the effect of cooling rate fluctuations on the DCP (see Section 3.2). The apparatus (Figure 24) and experimental setup (Figure 25) were developed through optimization experiments for A319 alloy (see Section 3.1) and were used for the rheological tests on AZ91E alloy as well. Torque and temperature readings were recorded at the same time intervals as in the optimization experiments.

4.1.2 Melting Procedure

The AZ91E alloy was melted in a graphite crucible (Figure 26) inside an electric furnace. CO_2 cover gas was maintained at a flow rate of 0.3m^3/h to minimize the formation of Mg oxides that could affect the rheological and temperature readings. Once the charge reached 700°C, the grain refiner was added to the melt and held for five minutes. The melt was then stirred with a stainless steel propeller for 30 seconds. During this time, a spindle was attached to the viscometer and preheated with a torch until the spindle changed color to bright red, indicating that it was approximately 800 °C [34].

4.1.3 Post-Melting Procedure

Once stirring was complete, the graphite crucible was taken out of the furnace and placed at the viscometer location. The flow rate of the CO_2 gas was increased to 0.6m^3/h to account for the higher susceptibility of the melt to oxidation outside the furnace, due to greater exposure to oxygen. At this point, the temperature and rheological acquisition system was started. The preheated viscometer spindle was lowered into the charge and rotated at a constant rate of 0.5 RPM to enable minimal fluctuations in torque. The spindle and thermocouple were immersed

at the same depth for all experiments. Temperature and torque data were continuously measured and recorded. Torque and cooling curve plots were developed.

4.2 Quench Experiments

The quench experiments were conducted with a view to analyzing the microstructural development during solidification. All the Ti levels investigated for the rheological experiments were also investigated for the quench experiments in order to observe changes in the growth mechanism and dendritic structure that resulted from the variation in addition levels. The quench experiments were comprised of two stages: specimen casting and quenching. The first stage involved casting a specimen with the desired composition and shape required to fit in the quenching apparatus. The second stage consisted of assembling the quench apparatus and using it to quench the specimen at the desired temperature.

4.2.1 Specimen Casting

A 500 g charge of the base AZ91E alloy was melted in a steel crucible with CO_2 cover gas at a flow rate of $0.3m^3/h$. Once the melt reached 700°C, the Al-5Ti-1B grain refiner was added and held for five minutes. The melt was subsequently stirred for 30 seconds and then poured into a graphite mould (Figure 31).

4.2.2 Quenching

The castings produced in the previous section were cut into 75 mm long rods. The rods were then inserted into plain carbon steel tubes (technical drawing shown in Figure 32). These tubes were pressure sealed on both sides. The wall thickness of the tubes was designed such that it was thin enough to promote rapid quenching, but strong enough to resist the pressure forces produced during thermal expansion of the tube contents. Each pressure seal was tested by immersing the quench apparatus in water to observe if gas bubbles would appear on the surface. Once the seal was checked, the tubes were placed in an electric furnace and held until the liquid metal reached

700°C. The furnace was then lowered to a temperature slightly below the liquidus temperature of the modified alloy (determined from cooling curves of rheological experiments). The tubes were held at this temperature for one hour in order to ensure homogeneity of the microstructure. The test tubes were then removed from the furnace and quickly quenched in room temperature water. Three quench tests were conducted for each addition level in order to ensure the reproducibility of the results.

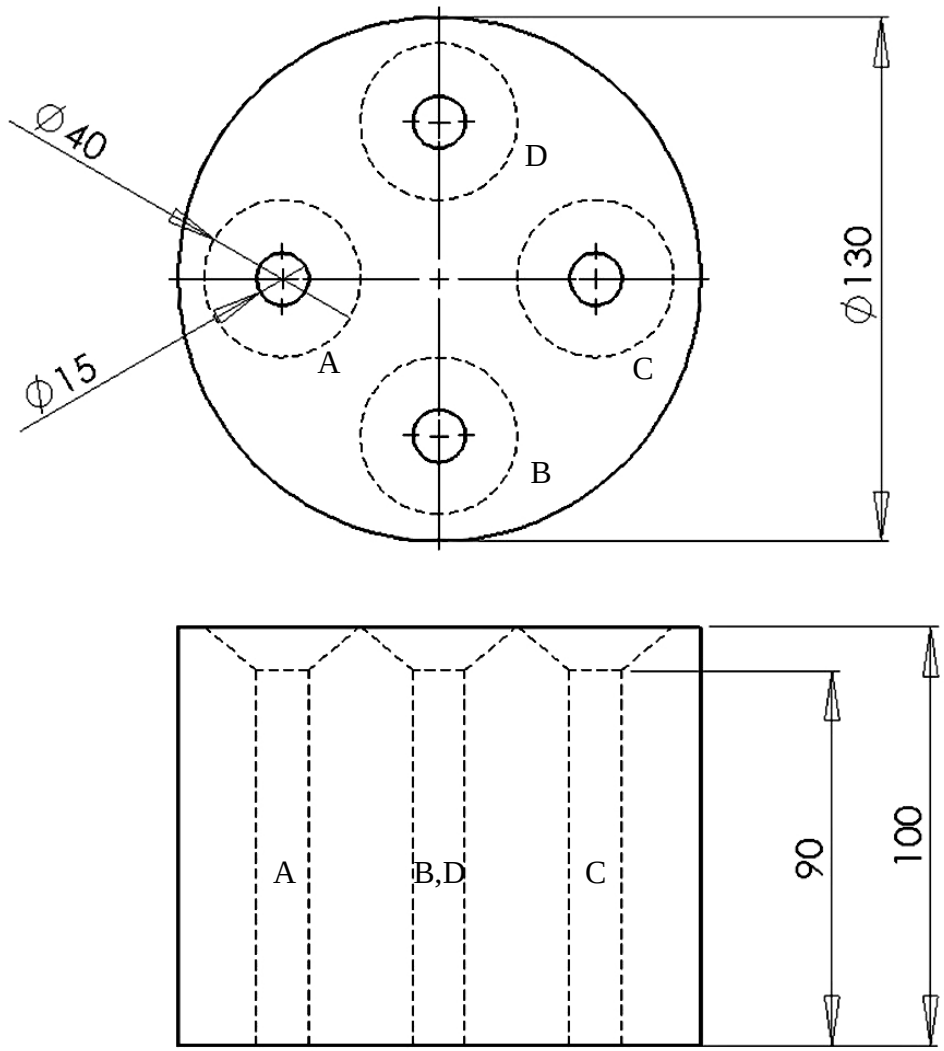

Figure 31. Schematic of the graphite mould used for quench experiments (units in mm).

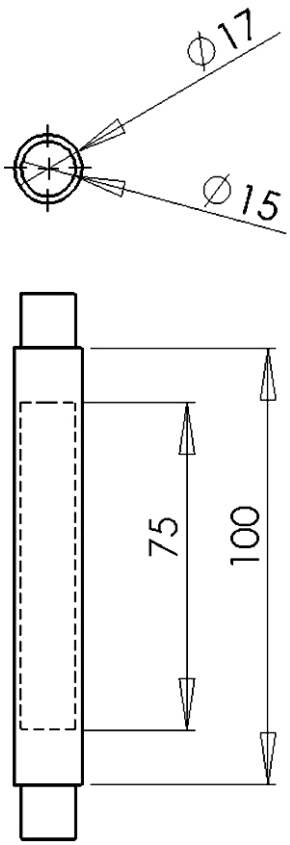

Figure 32. Schematic of tube apparatus used for quench experiments (units in mm).

4.3 Preparation for Microscopy and Grain Size Measurements

Samples for microstructure analysis were extracted from the rheological and quench specimens. Figure 33 illustrates the location of these extracted samples. Rheological samples were extracted just below the spindle location. Quench samples were extracted from the centre of the casting. The quenched samples were cold-mounted in order to prevent changes to the microstructure during the mounting process. The samples were polished using silicon carbide grinding paper starting at 120 grit size and progressing to finer grit sizes of 1200 grit. Finally, the samples were polished using 3 micron diamond as the suspension abrasive.

Rheological samples were etched for grain size measurements. The etchant was 75% ethyl alcohol, 15% acetic acid, and 10% distilled water by volume. Each sample was etched for two minutes. The linear intercept method was used to measure the grain size of the rheological

samples for each addition level. A minimum of 100 grains were measured for each sample (minimum two samples per addition level) using an optical microscope in conjunction with image analysis software. ANOVA tests were performed on the grain size values and the null hypothesis was rejected if $P_{\alpha max}$ was greater than 99%, thereby indicating that a significant change in grain size was observed with varying Ti level. The rheological and quench samples were subsequently analyzed using scanning electron microscopy (SEM) to examine the phases present, nucleating particles, and dendritic structure during solidification.

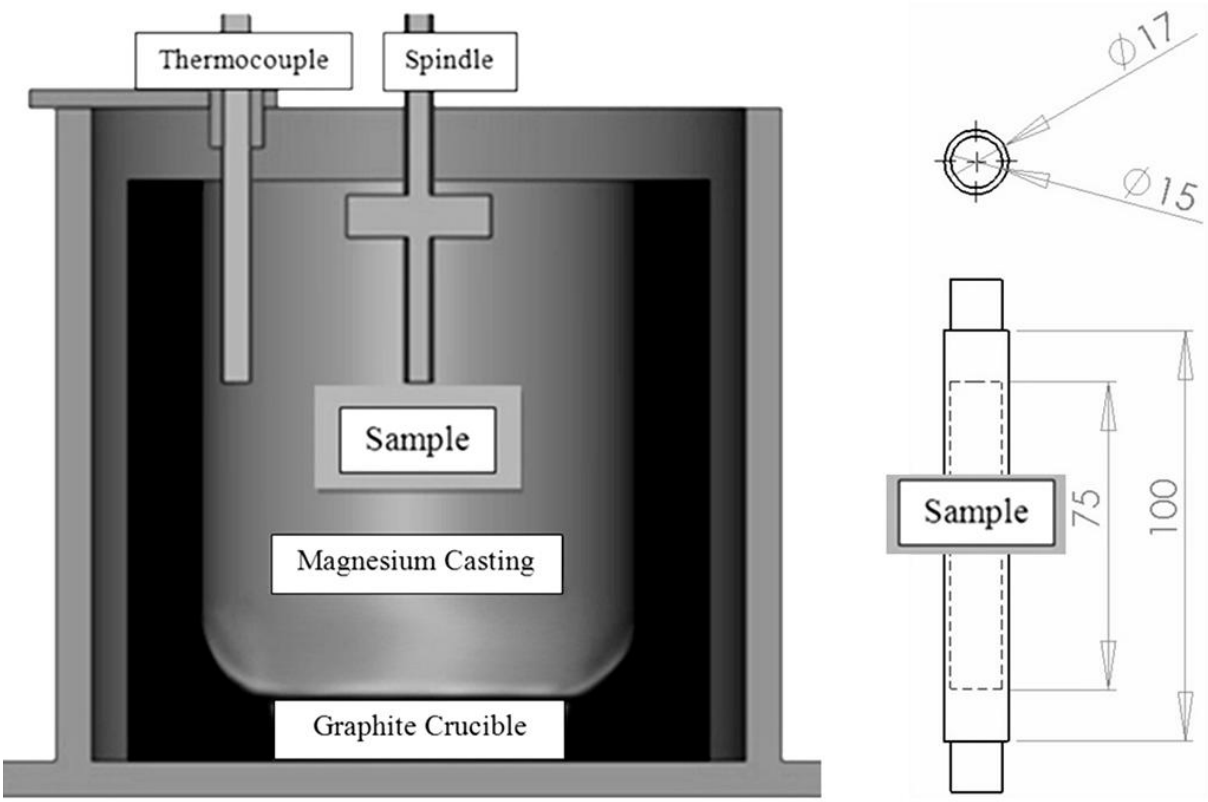

Figure 33. Microscopy sample location from rheological and quench experiments (units in mm).

4.4 Porosity Experiments

The purpose of the porosity experiments was to determine the effect of TIBOR refiner on the porosity of AZ91E alloy. New castings were produced for porosity analysis (mould shown in Figure 34). The pouring temperature and mould temperature were 700 °C and 500 °C respectively. A constant cooling rate of 1°C/s was maintained for all castings. Two castings were

produced for the base alloy and each addition level to ensure repeatability of the results. Casting porosity was determined using the Archimedes' principle according to ASTM D792 standard. ANOVA was conducted to ensure significant results. The null hypothesis was rejected if $P_{\alpha max}$ > 99%, thus indicating that the Ti addition level caused a significant change to the porosity of the casting.

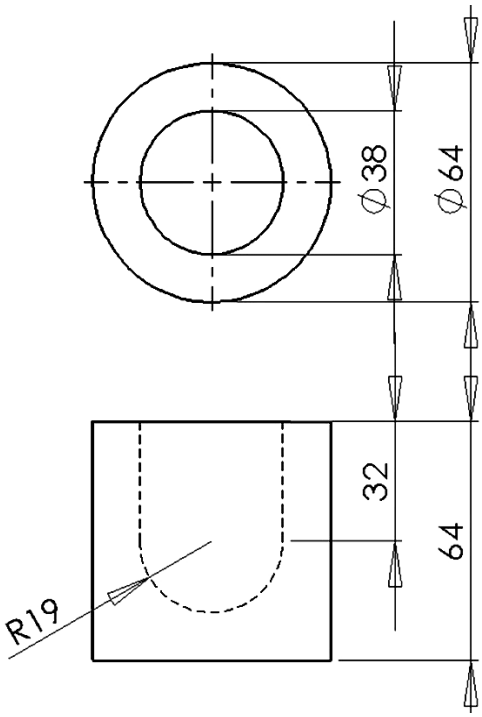

Figure 34. Graphite mould for porosity experiments (units in mm).

4.5 Summary of Experiments

The following tables provide a summary of the experiments conducted for this thesis. A minimum of three experiments per addition level were done at each addition level for the rheological experiments. If the standard deviation for the data at a particular addition level was too large, additional experiments were performed. For the quench experiments, three experiments were done per addition level. For the porosity experiments, two experiments were performed at each addition level.

Table 8. Rheological experiments performed on AZ91E alloy.

	Addition Level [wt.% Ti]	Number of Experiments
AZ91E Alloy Rheological Experiments	0	6
	0.005	3
	0.05	6
	0.1	4
	0.2	4
	0.3	3
Total Experiments	**26**	

Table 9. Quench experiments performed on AZ91E alloy.

	Addition Level [wt.% Ti]	Number of Experiments
AZ91E Alloy Quench Experiments	0	3
	0.005	3
	0.05	3
	0.1	3
	0.2	3
	0.3	3
Total Experiments	**18**	

Table 10. Porosity experiments performed on AZ91E alloy.

	Addition Level [wt.% Ti]	Number of Experiments
AZ91E Alloy Porosity Experiments	0	2
	0.005	2
	0.05	2
	0.1	2
	0.2	2
	0.3	2
Total Experiments	**12**	

CHAPTER 5. RESULTS AND DISCUSSION

The results are divided into three sections. In the first section, the microscopy results are presented with a view to analyzing the effect of Al-5Ti-1B (TIBOR) addition on the microstructure. The rheological data are examined in the second section to determine the impact of the TIBOR refiner on the dendrite growth rate and DCP. The final section presents the data from the porosity experiments and analyzes the relation between the DCP, microstructure, and porosity of the casting.

5.1 Microstructure

5.1.1 Grain Size Measurements

The optical micrographs of the samples obtained after rheological testing are shown in Figure 35. These micrographs were used to carry out the grain size measurements. The average grain size for each addition level is presented in Figure 36 (note that the length of the error bars is two sample standard deviations). The base alloy was observed to have an average grain size of 1630 µm. The maximum reduction in grain size was achieved at the lowest addition level (0.005 wt.% Ti). At this level, there was a 63% reduction in grain size relative to the base alloy, resulting in an average grain size of 606 µm (Pαmax = 99.74%, Appendix D: Table D.1.2). Past studies have shown that an increase in the Al content in AZ91 alloy does not result in any grain refinement [18, 28]. As a result, it is likely that the reduction in grain size was primarily a consequence of the Ti present in the TIBOR master alloy.

The addition level of Ti was increased to 0.05 wt.% and this resulted in a significant increase of the average grain size from 606 µm to 926 µm ($P_{\alpha max}$ = 99.99%, Appendix D: Table D.1.3). Addition levels beyond 0.05 wt.% Ti did not cause a significant change in grain size (Appendix D: Table D.1.4). Elsayed [32] also investigated the effect of TIBOR addition on the grain size of AZ91E alloy (for addition levels ranging from 0 to 0.05 wt.% Ti) and found that the maximum reduction (61%) in grain size was achieved at the 0.005 wt.% Ti level.

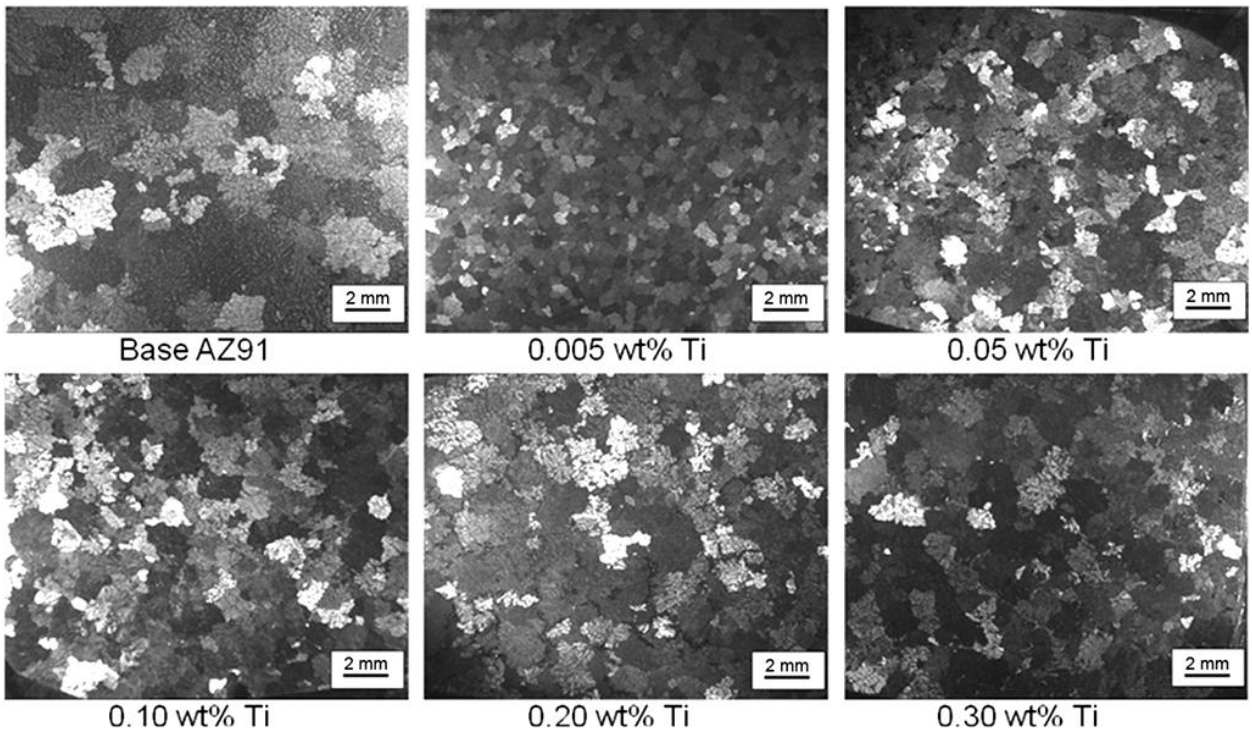

Figure 35. Optical micrographs of the grain size for AZ91E base alloy at various addition levels.

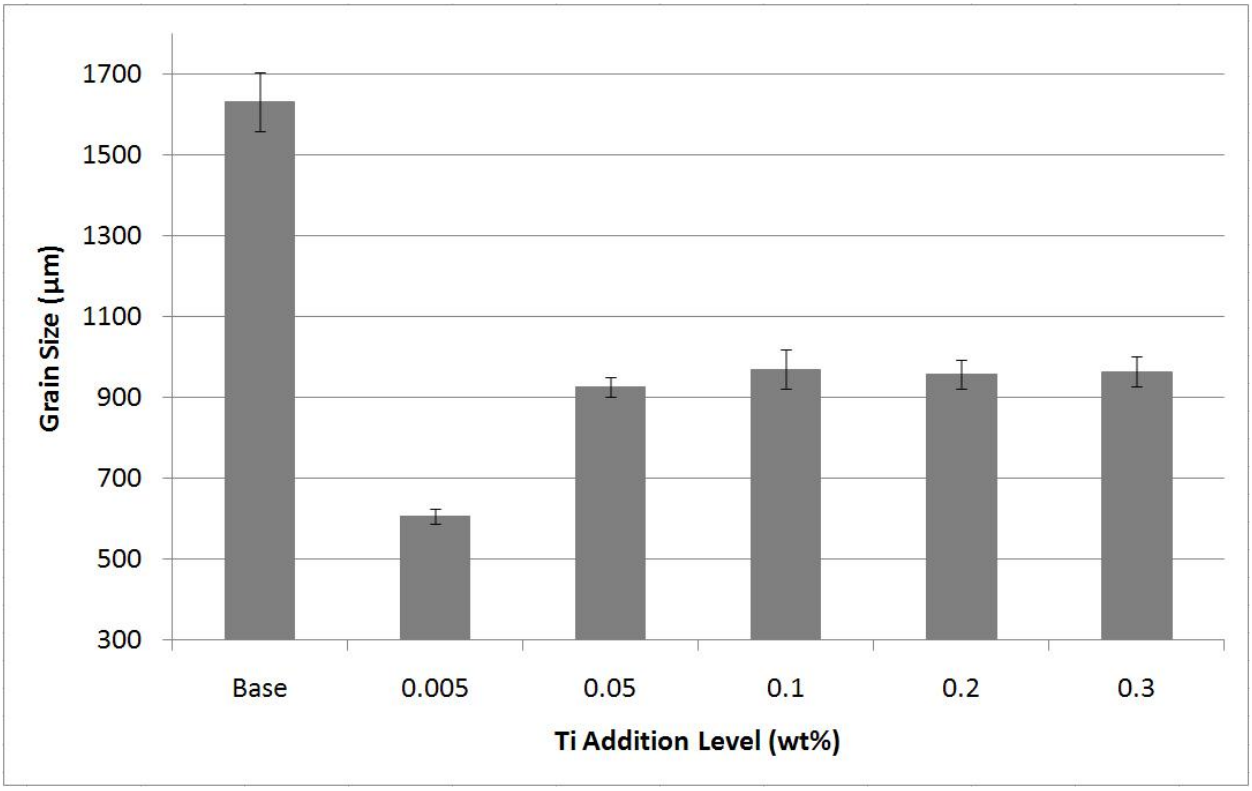

Figure 36. Effect of grain refiner addition on the average grain size of AZ91E alloy.

The reason for the significant reduction in grain size at the 0.005 wt.% Ti level cannot be understood through an analysis of the grain size alone. The optical micrographs of Figure 35 do not indicate whether grain refinement was a consequence of heterogeneous nucleation, a decrease in the dendrite growth rate, or both. Furthermore, these optical micrographs do not provide an explanation for the increase in grain size with further TIBOR addition.

Backerud *et al.* [31] found that when exceeding the addition level corresponding to the minimum grain size, the increasing constitutional effect of alloying elements may increase the driving force for growth to an extent where a successive penetration of the diffusion layer by lancet-like dendrite tips occurs. In turn, a major part of the diffusion takes place sidewise rather than in front of the growing dendrites. This phenomenon leads to an increase in the growth rate of the dendrites and consequent coarsening of the grain structure. It is likely that such a phenomenon was the cause for grain coarsening with higher Ti addition levels in this research.

5.1.2 AZ91E General Microstructure

The microstructure of the base alloy was examined to gain a better understanding of the effects of TIBOR addition. Unrefined AZ91E alloy was analyzed using scanning electron microscopy (SEM) in conjunction with energy dispersive X-ray spectroscopy (EDX) to observe the microstructure and identify the phases before the addition of the TIBOR grain refiner. An SEM micrograph of the base alloy is presented in Figure 37. EDX identified the α-Mg, $Mg_{17}Al_{12}$ and Mn_X-Al_Y phases for the base alloy. These phases were present at all addition levels (see Appendix B: Figure B.1.1).

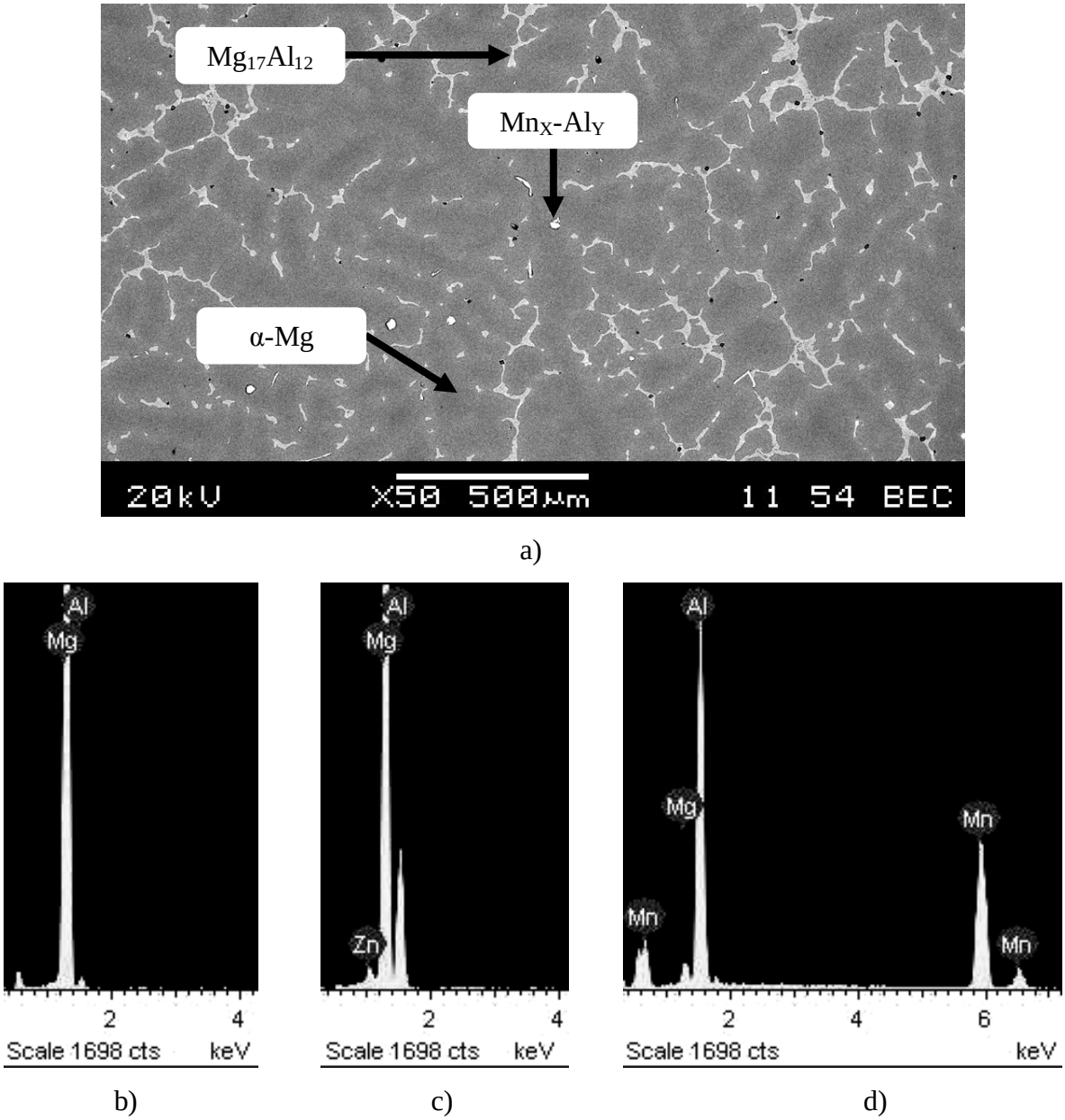

Figure 37. SEM micrograph of unrefined AZ91E alloy showing a) general microstructure and EDX scans of b) primary α-Mg, c) $Mg_{17}Al_{12}$, and d) Mn_X-Al_Y phases.

5.1.3 Nucleation of Grains

Samples of AZ91E with 0.005 wt.% Ti were examined to identify the nucleating particle. The core of the dendritic structure was examined using SEM and EDX to locate Ti particles acting as nuclei for grains. The SEM micrograph of the equiaxed dendritic structure in a quenched sample

at the 0.005 wt.% Ti addition level, along with EDX of the nucleating particle, are shown in Figure 38. EDX confirmed that the particle at the centre of the dendrite was indeed Ti, suggesting that Ti acted as a nucleant. SEM was performed on the remaining samples with identical observations (see Appendix C: Figure C.1.1 - Figure C.1.3). Thus, there is conclusive evidence that Ti particles become active nucleating sites in unrefined AZ91E alloy.

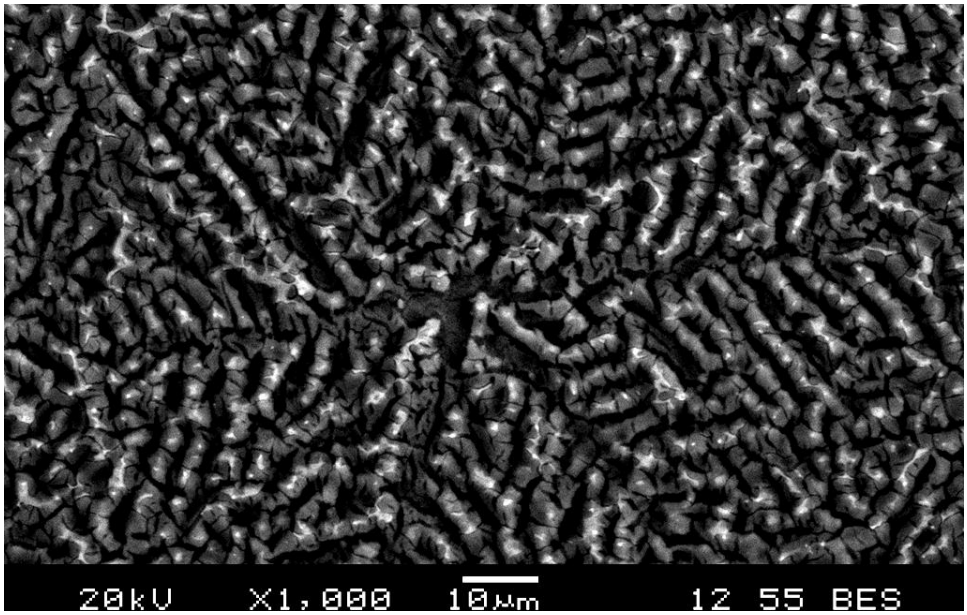

a)

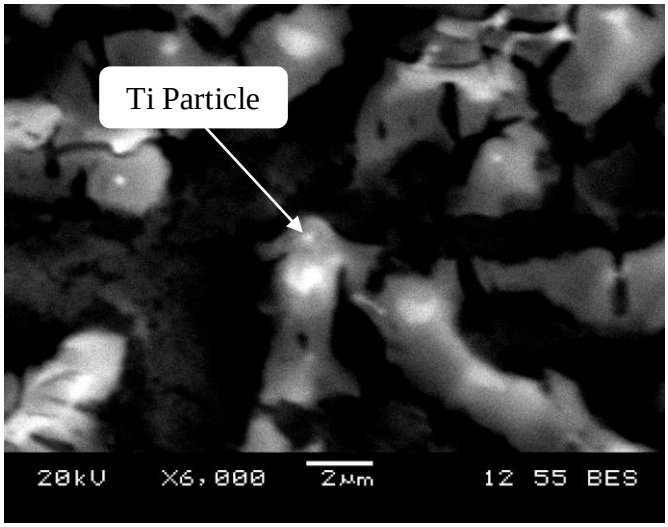

b)

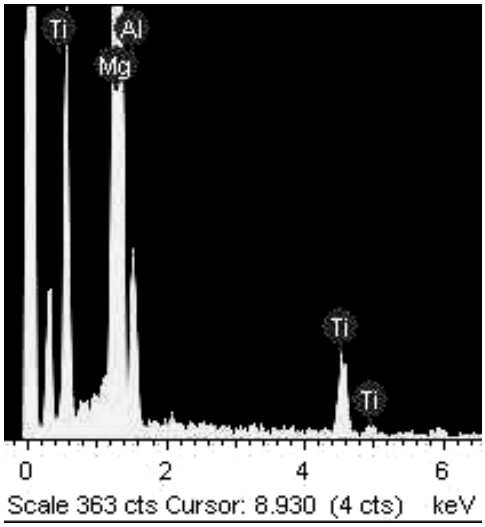

c)

Figure 38. SEM of quenched AZ91E at 0.005 wt.% Ti level illustrating a) equiaxed dendrite, b) enlarged view of Ti particle at the centre of dendrite, and c) EDX of the particle.

5.1.4 Growth of Dendrites

In addition to supplying the melt with active nucleating particles, the level of grain refinement in an alloy can be enhanced by increasing the GRF of the base alloy. If the Ti solute particles segregated in front of the solidifying dendrite arms, a constitutionally undercooled zone would be created at the solid-liquid interface that would consequently decrease the dendrite growth rate. The decrease in dendrite growth rate would in turn produce a finer grain structure since it would allot more time for new nucleating sites to develop in the constitutionally undercooled zones.

A SEM micrograph of a rheological sample at the 0.3 wt.% Ti level is shown in Figure 39 a). Titanium was identified at the eutectic location using EDX (Figure 39 b)). Identical observations were made in repeat samples (Appendix B: Figure B.1.2). Since the eutectic phase is the last to form during solidification, this finding supports the possibility that the solute particles, introduced through the addition of the grain refiner, segregated to the front of the dendrite tips and behaved as a growth restrictor. Another possibility however, is that the Ti particles may have formed as a phase with the eutectic and, as a result, Ti would not have had a growth restricting effect on the dendritic structure. Consequently, the SEM in Figure 39 does not provide conclusive evidence as to whether the Ti particles behaved as a growth restrictor.

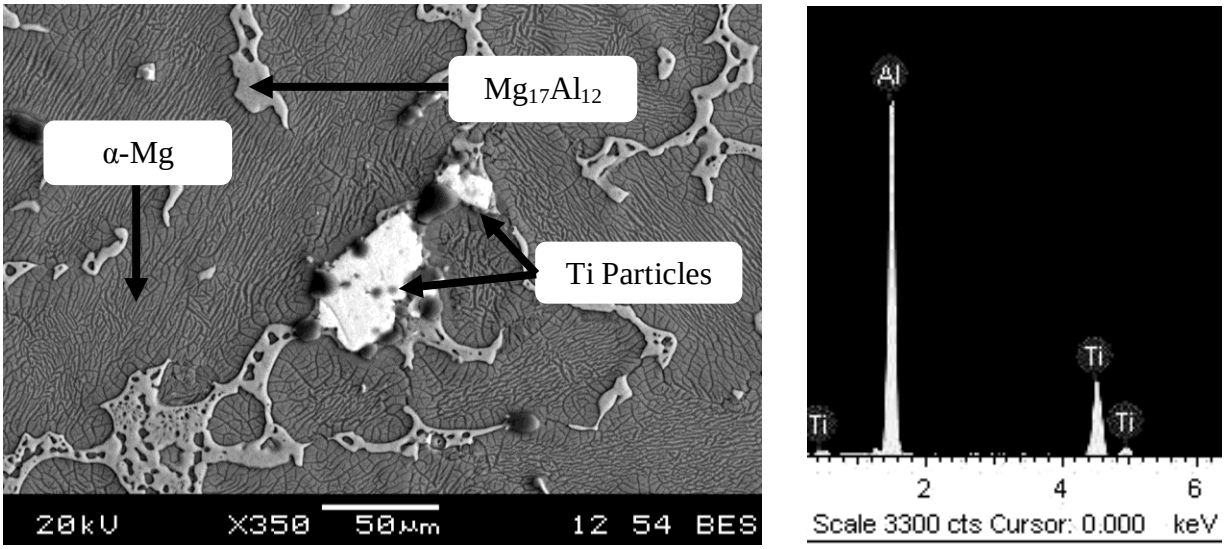

a) b)

Figure 39. a) SEM micrograph and b) EDX for a rhelogical sample at the 0.3 wt.% Ti addition level illustrating the segregation of Ti particles at the eutectic region.

To verify whether Ti behaved as a growth restrictor prior to the formation of the eutectic, SEM analysis was performed on a quenched sample at the 0.3 wt.% Ti level. For this addition level, the sample was quenched at a temperature slightly below the liquidus temperature which was determined from the cooling curves (Appendix A: Figure A.7.1 - Figure A.7.3). The SEM micrograph (Figure 40) of the quenched AZ91E sample with 0.3 wt.% Ti revealed the segregation of Ti particles at the solid-liquid interface during solidification. This suggests that the solute was pushed towards the dendrite tips during solidification, thereby increasing the GRF and consequently decreasing the growth rate of the dendrite arms. Thus, it is likely that the Ti particles have a growth restricting effect on the AZ91E alloy.

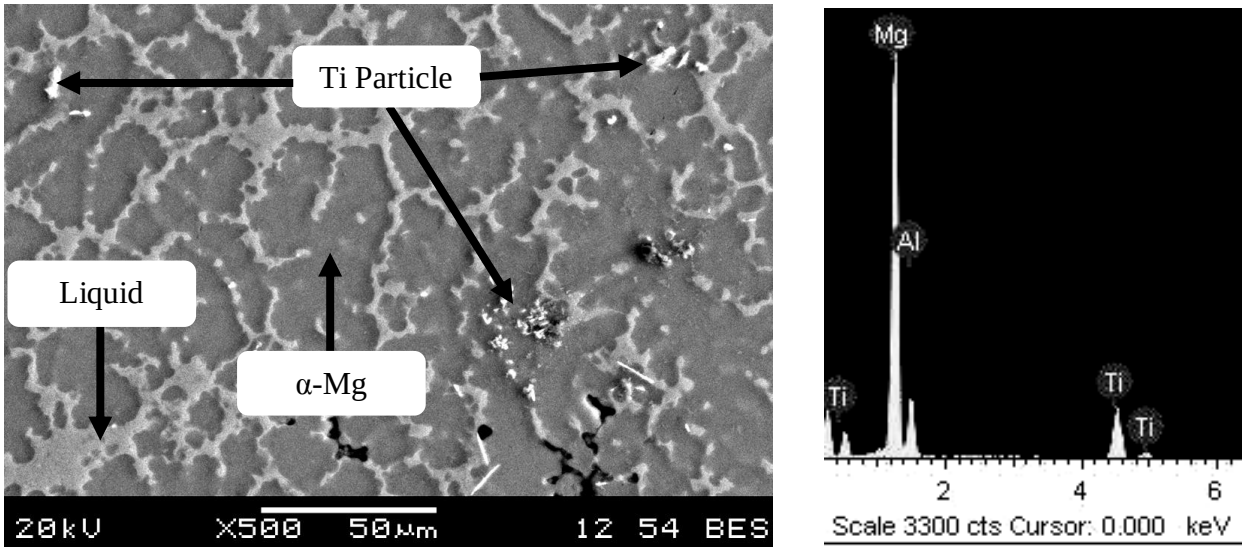

a) b)

Figure 40. a) SEM micrograph and b) EDX for a quenched sample at the 0.3 wt.% Ti addition level illustrating the segregation of Ti particles to the solid-liquid interface.

Quenched samples were also analyzed to determine whether there was a change in the growth mechanism that was responsible for the increased grain size at addition levels above 0.005 wt.% Ti. As suggested earlier, there is evidence suggesting that grain coarsening can occur as a result of a change in the morphology of the dendrites to a lancet-like form [31].

SEM analysis was performed on the quenched samples at all addition levels to investigate any change in the morphology of the dendrites that may have occurred as the grain refiner addition

level was increased. In fact, the SEM micrographs in Figure 41 show a change in the dendritic morphology from equiaxed to lancet-like with further grain refiner addition.

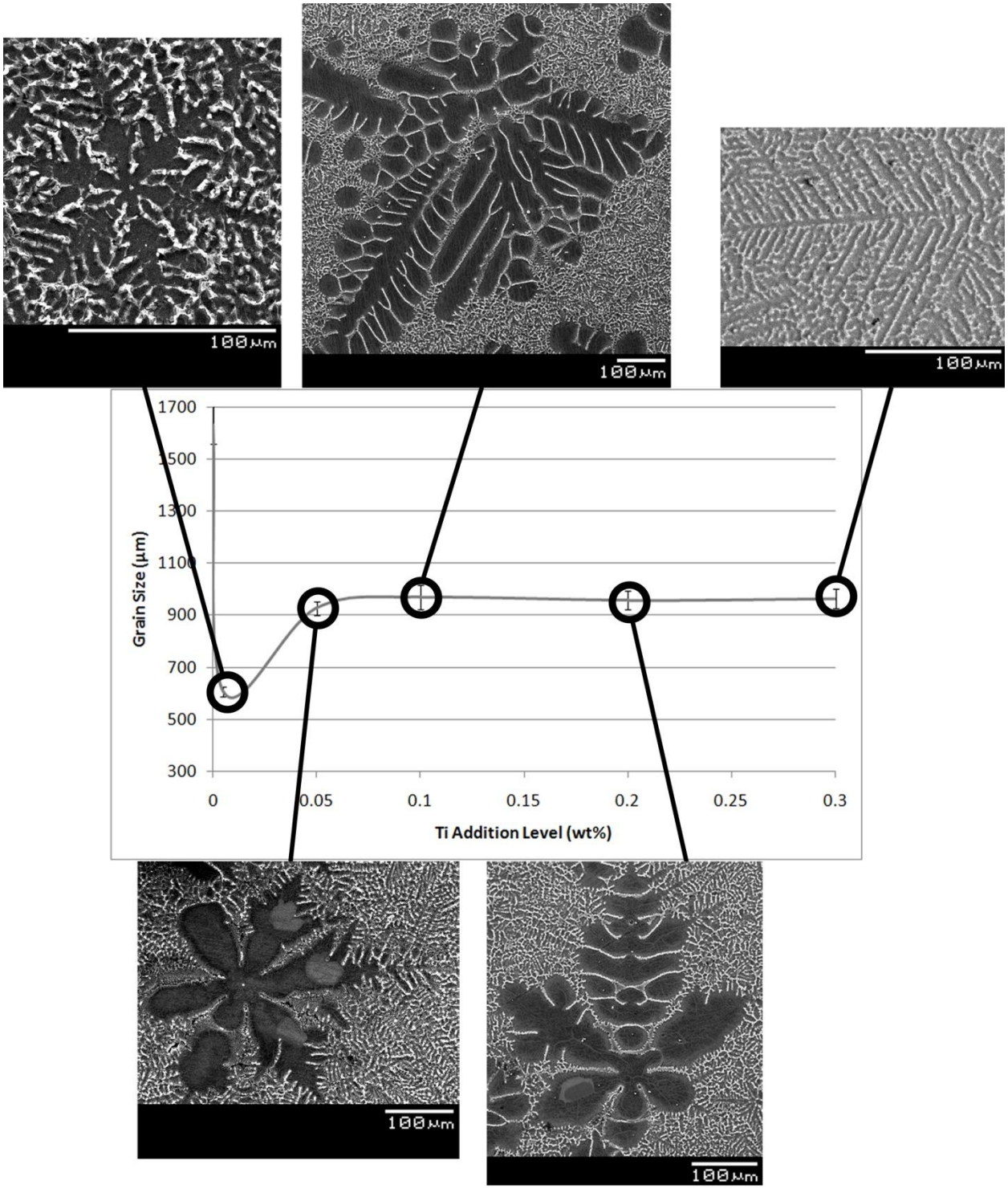

Figure 41. SEM micrographs illustrating the change from the equiaxed dendritic structure (at 0.005wt% Ti) to a progressively more lancet-like structure with further Ti additions.

For the lowest addition level (0.005 wt.% Ti), the solute was rejected in front of the dendrite tip, thereby increasing the diffusion layer and consequently reducing the growth rate. A stable, equiaxed, six-fold dendritic structure formed at the lowest addition level (Figure 41). This suggests that a uniform decrease in the growth rate of the dendrite arms resulted at the 0.005 wt.% Ti addition level. Researchers observed that as solute is added, the dendrite tip becomes thinner [19]. Further refiner addition may have decreased the dendrite tip radius to the extent that it caused solute to diffuse sidewise instead of in-front of the dendrite tip. This phenomenon decreased the diffusion boundary layer ahead of the dendrite tip and consequently caused an increase in the growth rate of the dendrite arms. The resultant instability in the dendrite growth rate caused a change in the dendritic morphology from equiaxed to a lancet-like structure. The transition in the dendritic structure from equiaxed to lancet-like is most evident at the 0.05 wt.% Ti level. The instability in the growth rate caused some of the dendrite arms (arms growing towards the right side) to grow at a faster rate than others (arms growing towards the left side). Further solute addition strengthened this behaviour. As can be seen from Figure 41, with increasing addition level, the dendritic structure becomes progressively more lancet-like in morphology. Additional micrographs illustrating this phenomenon are shown in Appendix C (Figure C.1.1 - Figure C.5.1).

5.2 Rheological Analysis

Rheological data and cooling curves were first analyzed to determine the dendrite growth rate for all the addition levels. Further, the relationship between the dendrite growth rate, the dendritic morphology and grain size was investigated. Finally, the rheological data and cooling curves were used to obtain the coherency solid fraction and, in so doing, determine the overall effect of TIBOR grain refiner on the DCP of AZ91E alloy. ANOVA tests were performed on the growth rate (Appendix D.2: Table D.2.1 - Table D.2.3) and coherency solid fraction (Appendix D.3: Table D.3.1 - Table D.3.3) in order to ensure the results were statistically significant.

5.2.1 Dendrite Growth Rate

The dendrite growth rate and DCP were identified from cooling curves and torque plots. A typical rheological data and cooling curve plot for unrefined AZ91E alloy is in Figure 42. All the cooling curves and rheological plots obtained from the experiments are provided in Appendix A. The initial torque for the solidifying AZ91E alloy (regardless of Ti addition level) was steady and almost asymptotic to the x-axis. At the DCP, there was a sudden increase in torque due to the coalescence of dendrite arms, which caused a restriction in the rotation of the spindle. The temperature corresponding to the DCP was labeled the dendrite coherency temperature (DCT) and the time elapsed from liquidus to the DCP was labeled the coherency time (t).

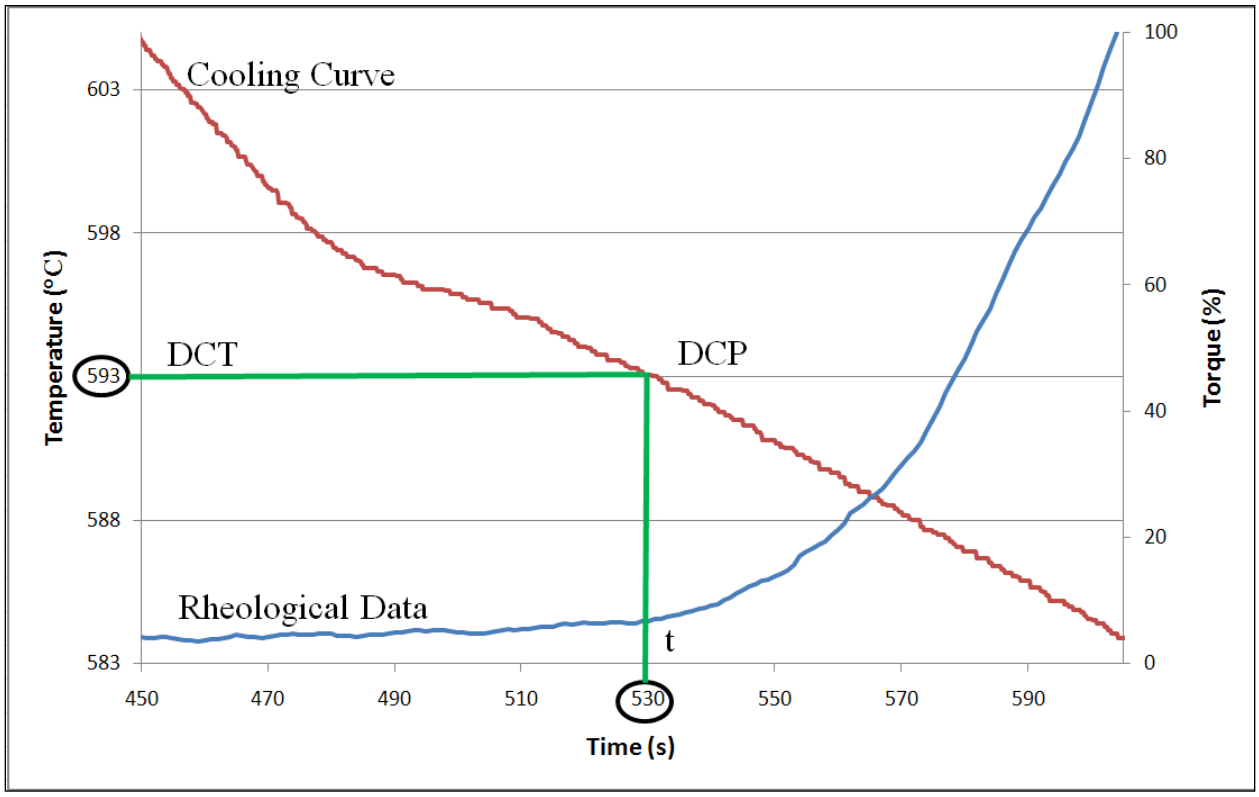

Figure 42. Typical rheological data and cooling curve obtained for AZ91E base alloy.

Table 11 provides a summary of the average liquidus temperature, average coherency temperature and average coherency time for the various Ti addition levels tested on AZ91E alloy.

Table 11. Rheological data obtained for AZ91E alloy at the tested addition levels.

Addition Level [wt.% Ti]	Average Liquidus Temperature [°C]	Average Coherency Temperature [°C]	Average Coherency Time [s]
0	598.0	593.3	50
0.005	599.3	589.7	89
0.05	592.5	585.5	66
0.10	586.8	578.0	68
0.20	576.0	571.0	42
0.30	567.0	561.7	46

At the DCP, the final grain size of the alloy is established. The dendrites cease to grow lengthwise, while the dendrite branches continue to thicken. The dendrite growth rate can be obtained from the grain size and coherency time using the following equation:

$$V = R / t \tag{7}$$

where V is the growth rate (µm/s), R is the grain radius (µm), and t is the time (s) from liquidus to the DCP [27].

The dendrite growth rate for each addition level is presented in Figure 43 (note that the length of the error bars is two sample standard deviations). There was a significant decrease in the dendrite growth rate at the 0.005 wt.% Ti level from 32.6 to 6.8 µm/s as compared to the base alloy ($P_{\alpha max}$ > 99.99%, Appendix D.2: Table D.2.2). At this addition level, an equiaxed dendritic structure (Figure 41) was present. The growth rate significantly increased from 6.8 to 14.1 µm/s when the addition level was raised to 0.05 wt.% Ti ($P_{\alpha max}$ > 99.99%, Appendix D.2: Table D.2.3). Addition levels above 0.05 wt.% Ti continued to increase the dendrite growth rate, ultimately producing a growth rate of 21.2 µm/s at the 0.3 wt.% Ti addition level. The increase in growth rate was a consequence of the reduced diffusion boundary layer in front of the dendrite tip. The reduction in the diffusion boundary layer was caused by a reduced dendrite tip radius. As mentioned in Section 5.1.4, the reduced dendrite tip radius led to instability in the growth rate of the dendrite arms that subsequently led to a transition in the dendritic morphology from equiaxed

to a lancet structure. The trend in the dendrite growth rate corresponds to the progressively more lancet-like structures observed with increasing addition levels (shown in the micrographs of Figure 41).

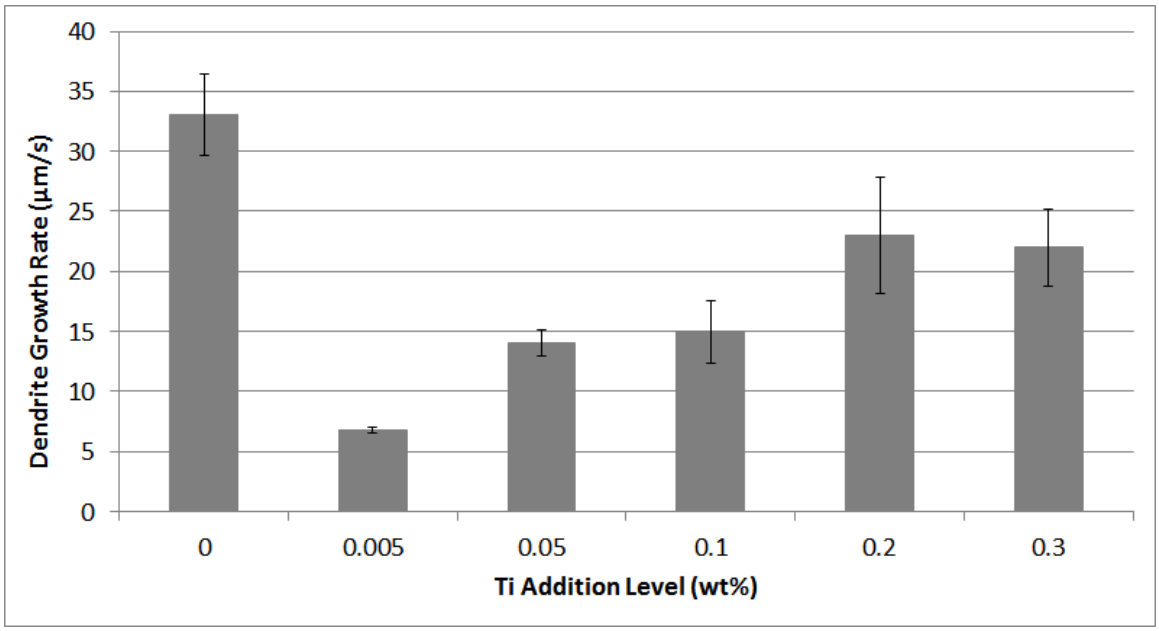

Figure 43. Effect of Ti level on the average dendrite growth rate of AZ91E.

5.2.2 Coherency Solid Fraction

A decrease in growth rate generally delays the coherency point [20, 22, 31]. The introduction of active nucleants through grain refinement however reduces the distance traveled by dendrites, which may consequently cause earlier impingement. The overall effect on the DCP was determined by analyzing the coherency solid fraction. The solid fraction f_s^{Sch} at the coherency temperature DCT was calculated using the Scheil equation, shown below:

$$f_s^{Sch} = 1 - \left(\frac{T_M - DCT}{T_M - T_L}\right)^{-\frac{1}{1-k}} \tag{8}$$

$$k = \frac{T_M - T_L}{T_M - T_S} \tag{9}$$

where T_M is the melting point of pure magnesium, T_L is the liquidus temperature of the alloy, k is the partition coefficient of the alloy calculated using Equation 8, and T_S is the solidus temperature of the alloy [35]. The parameters DCT, T_L and T_S were determined from the cooling curve plots (Appendix A). The value used for T_M was 650°C (obtained from literature) [1].

The effect of Ti addition level on the coherency solid fraction is presented in Figure 44 (note that the length of the error bars is two sample standard deviations). It was found that the 0.005 wt.% Ti addition level had the highest coherency solid fraction. At this addition level, the solid fraction as compared to the base alloy increased significantly from 10.3% to 20.3% ($P_{\alpha max}$ > 99.99%, Appendix D: Table D.3.2). The increase in the solid fraction at the DCP suggests that the increase in the GRF, and consequent decrease in growth rate, had a greater influence on the coherency solid fraction as compared to the reduced distance between nucleating sites.

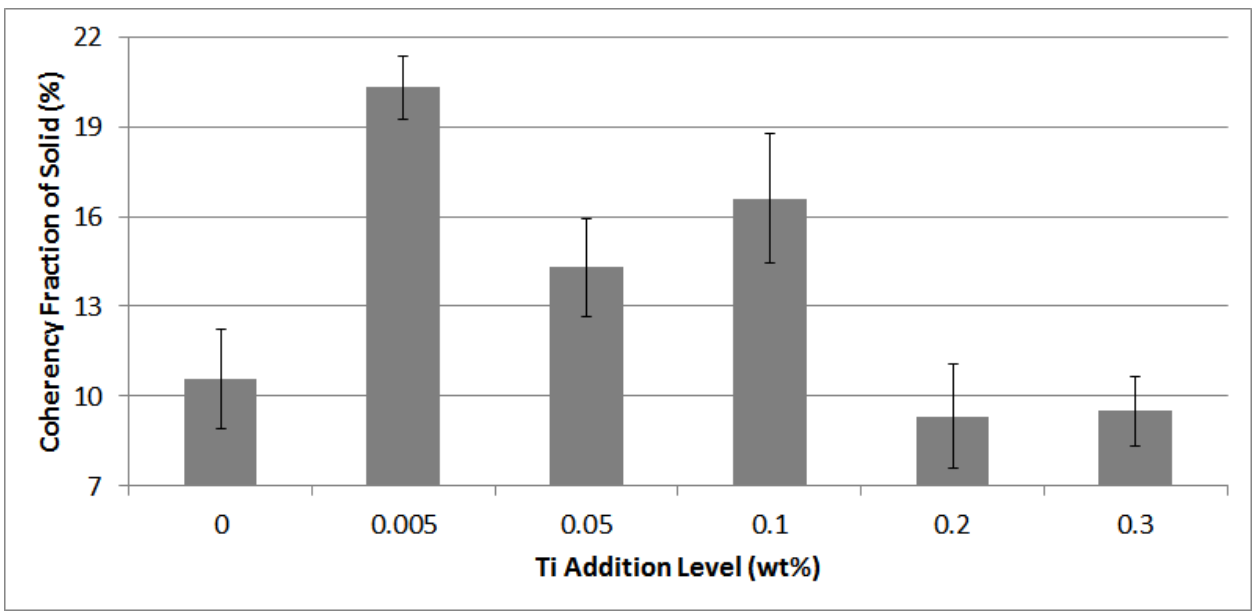

Figure 44. Effect of Ti level on the average coherency solid fraction of AZ91E.

An increase in the refiner addition level from 0.005 wt.% Ti to 0.05 wt.% Ti caused a significant decrease in the coherency solid fraction from 20.3% to 14.3% ($P_{\alpha max}$ = 99.97%, Appendix D: Table D.3.3). The decrease in the coherency solid fraction was a consequence of the change in morphology to a lancet-like structure and subsequent increase in the dendrite growth rate for addition levels above 0.005 wt.% Ti. Moreover, although the growth rate was lower than the

base alloy for the 0.2 wt.% Ti and 0.3 wt.% Ti addition levels, the increase in the number of nucleating sites shortened the distance for dendrites to travel before impingement. The combination of the decreased growth rate and increased number of nucleants did not cause a significant change in the coherency solid fraction at the 0.2 wt.% Ti and 0.3 wt.% Ti levels as compared to the base alloy.

5.3 Porosity Analysis

The porosity in the castings was measured using Archimedes' principle according to ASTM D792 standard. Two castings were analyzed per addition level and ANOVA tests were conducted to ensure the statistical significance of the results and conclusions. Figure 45 illustrates the porosity measurements for the castings at the various Ti addition levels (note that the length of the error bars is two sample standard deviations). The porosity measurements were in agreement with the coherency fractions of solid. This was expected since the porosity of a casting is strongly influenced by the coherency solid fraction [4, 5].

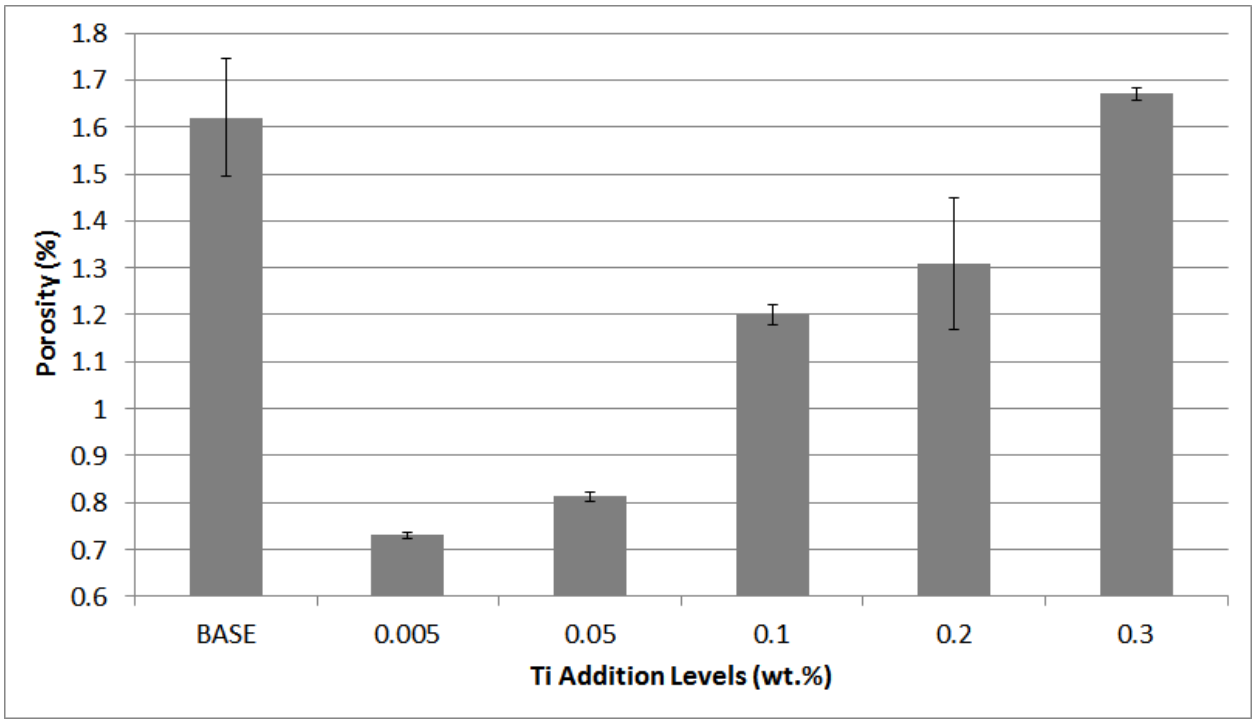

Figure 45. Effect of Ti addition level on the average porosity of cast AZ91E.

The porosity in the castings at the 0.005 wt.% Ti addition level decreased from 1.62% to 0.73% as compared to the base alloy ($P_{\alpha max}$ = 99.03%, Appendix D: Table D.4.2). This level also corresponded to the greatest increase in the coherency solid fraction. The increase in the coherency solid fraction compared to the base alloy at the 0.005 wt.% Ti addition level (from 10.3% to 20.3%) caused a reduction in the amount of blocked interdendritic liquid. As a consequence, there was less interdendritic shrinkage and the casting porosity decreased.

With further refiner addition beyond 0.005 w.% Ti, the porosity in the castings increased significantly. At the 0.05 wt.% Ti level, there was a significant increase in casting porosity from 0.73% to 0.81% ($P_{\alpha max}$ = 99.06%, Appendix D: Table D.4.3). The increase in porosity was due to the decreased solid fraction at the DCP.

A summary of the grain size, dendrite growth rate, coherency solid fraction and casting porosity for each addition level is provided in Table 12, where values of the sample mean plus/minus the sample standard deviation are listed.

Table 12. Influence of Ti level in AZ91E on the average grain size, growth rate, coherency solid fraction, and porosity.

Addition Level [wt.% Ti]	Grain Size [µm]	Growth Rate [µm/s]	DCP Solid fraction(f_{s-coh}) using Scheil Eq. [%]	Porosity [%]
0	1630 ± 72	33 ± 3.4	10.6 ± 1.66	1.62 ± 0.12
0.005	**606 ± 19**	**6.8 ± 0.21**	**20.3 ± 1.04**	**0.730 ± 0.006**
0.05	926 ± 25	14 ± 1.1	14.3 ± 1.63	0.813 ± 0.010
0.10	969 ± 48	15 ± 2.6	16.6 ± 2.15	1.20 ± 0.021
0.20	957 ± 37	23 ± 4.9	9.34 ± 1.75	1.31 ± 0.140
0.30	964 ± 36	22 ± 3.2	9.50 ± 1.18	1.67 ± 0.014

CHAPTER 6. CONCLUSIONS AND SUGGESTIONS FOR FUTURE WORK

6.1 Conclusions

The scope of this thesis was to examine the effect of Al-5Ti-1B (TIBOR) grain refiner to the dendrite coherency point (DCP), dendritic morphology, and porosity of AZ91E magnesium alloy, in an effort to improve the castability. Before any analysis was performed on AZ91E, the experimental setup was optimized using A319 aluminum alloy. Optimizing the experimental procedure ensured that significant data, and consequently observations, could be gathered from the tests performed on AZ91E. The observations and results gathered from the rheological, quench and porosity experiments are summarized below.

Microstructure Analysis:

1. Titanium acted as a nucleant and a growth restrictor when added to unrefined AZ91E alloy. The grain size of the base alloy decreased by 63% (from 1630 µm to 606 µm) with the addition of 0.005 wt.% Ti (added in the form of Al-5Ti-1B master alloy).

2. At higher addition levels, there was a change in the morphology of the dendritic structure from equiaxed to lancet, which consequently led to an increase in the dendrite growth rate. The increase in growth rate was a cause for the increased grain size at addition levels above 0.005 wt.% Ti.

Rheological Analysis:

1. At the 0.005 wt.% Ti addition level, the DCP was delayed and the coherency solid fraction significantly increased as compared to the base AZ91E alloy (from 10.6% to 20.3%). This suggests that the reduced dendrite growth rate had a greater effect on the DCP as compared to the shortened distance between nucleating sites that was a consequence of the increased number of active nucleants.

2. At higher addition levels, the coherency solid fraction decreased in comparison to the 0.005 wt.% Ti addition level. This phenomenon was a result of the increased dendrite growth rate.

Porosity Analysis:

1. At an addition level of 0.005 wt.% Ti, the porosity in the castings significantly decreased as compared to unrefined AZ91E alloy (from 1.62% to 0.73%). This decrease in porosity was caused by the significant increase in the coherency solid fraction achieved through the addition of the TIBOR grain refiner.

2. The trend in the porosity with varying Ti addition level closely resembles the trend in the coherency solid fraction. This similarity was due to the strong dependence of porosity on the DCP.

In conclusion, the DCP in AZ91E magnesium alloy can be significantly delayed. With only 0.005 wt.% Ti addition in the form of TIBOR grain refiner, the coherency solid fraction doubled as compared to the base alloy. This caused a considerable decrease of 45% in the porosity of the castings, and consequently improved the castability of AZ91E alloy.

6.2 Suggestions for Future Work

1. There exist other grain refiners such as ZnO, Al-3Ti-1B, Al-5TiB_2 and Al-Al_4C_3, whose effects on the dendrite coherency point (DCP) of cast AZ91E alloy have not been investigated. Although TIBOR was successful in delaying the DCP, it remains unknown as to whether TIBOR is the best grain refiner for AZ91E alloy. Possible future work involves examining the effects that other grain refiners have on the dendritic morphology, DCP and porosity of cast AZ91E alloy. In so doing, the optimal grain refiner that produces the highest coherency solid fraction and greatest improvement in the alloy castability can be determined.

2. A change in the morphology of the dendrites from equiaxed to lancet is indicative that a sudden increase in the dendrite growth rate occurred. The highest coherency solid fraction is generally obtained at the addition level slightly below the one corresponding to the transition in the dendrite morphology. This transition in morphology is due to the addition of solute particles that reduces the dendrite tip radius to the extent that solute is no longer diffused in front of the dendrite tip, but is rather diffused sidewise. A possible research topic involves measuring the critical dendrite tip radius. Obtaining the critical dendrite tip radius is beneficial to ensure that the alloying addition does not reduce the tip radius past the critical limit.

3. The porosity of a casting is one manifestation of castability. The castability of an alloy is also manifested in the fluidity. Fluidity is a measure of the capability of an alloy to flow into and fill a mold before solidifying. The fluidity of a material is determined by measuring the flow length. Improved fluidity corresponds to a longer flow length. The effect of TIBOR on the fluidity of AZ91E alloy can be measured for future work and compared to the respective coherency solid fraction.

REFERENCES

1. Avedesian, M. and Baker, H., Magnesium and Magnesium Alloys. 1999, Materials Park: ASM International.
2. Davis, J. R., Aluminum and Aluminum Alloys. 1994, Materials Park: ASM International.
3. Callister, W. D., Materials Science and Engineering: An Introduction. 6th ed. 2006, New York: John Wiley and Sons Inc.
4. Arnberg, L., Solidification Characteristics of Aluminum Alloys. Volume 3: Dendrite Coherency. 1996, Des Plaines: American Foundrymen's Society Inc.
5. Rappaz, M., Drezet, J. M. and Gremaud, M., *A New Hot Tearing Criterion.* Metallurgical and Materials Transactions A, 1999. **A30**: p. 449-455.
6. Dahle, A. K., Tondel, P. A., Paradies, C. J. and Arnberg, L., *Effect of Grain Refinement on the Fludity of Two Commercial Al-Si Foundry Alloys.* Metallurgical and Materials Transactions A, 1996. **A27**: p. 2305-2313.
7. Sumitomo, T., StJohn, D. H. and Steinberg, T., *The Shear Behavior of Partially Solidified Al-Si-Cu Alloys.* Materials Science and Engineering A, 2000. **A289**: p. 18-29.
8. Arnberg, L., Chai, G. and Backerud, L., *Determination of Dendritic Coherency in Solidifying Melts by Rheological Measurements.* Materials Science and Engineering A, 1993. **A173**: p. 101-103.
9. Dahle, A. K. and Arnberg, L., *Development of Strength in Solidifying Aluminium Alloys.* Acta Metallurgica, 1997. **45**: p. 547-559.
10. Vernede, S. and Rappaz, M., *Transition of the Mushy Zone from Continuous Liquid Films to a Coherent Solid.* Philosophical Magazine, 2006. **86**: p. 3779-3794.
11. Gourlay, C. M., Meylan, B. and Dahle, A. K., *Rheological Transitions at Low Solid Fraction in Solidifying Magnesium Alloy AZ91.* Materials Science Forum, 2007. **561-565**: p. 1067-1070.
12. Liu, Z., Xu, Q. and Liu, B., *Dendrite Growth Modelling of Cast Magnesium Alloy.* International Journal of Cast Metals Research, 2007. **20**(3): p. 109-112.
13. Barber, L. P., *Characterization of the Solidification Behavior and Resultant Microstructures of Magnesium-Aluminum Alloys*. Thesis (Masters). 2004, Worcester Polytechnic Institute. p. 108.

14. Medved, J. and Mrvar, P., *Thermal Analysis of the Mg-Al Alloys.* Materials Science Forum, 2006. **508**: p. 603-608.

15. Liang, S., Chen, R., Blandin, J., Suery, M. and Jan, E., *Thermal Analysis and Solidification Pathways of Mg-Al-Ca System Alloys.* Materials Science and Engineering A, 2008. **A480**: p. 365-372.

16. Mehl, R. F., Atlas of Microstructures of Industrial Alloys. 8th ed. Metals Handbook. Vol. 7. 1972, Metals Park: American Society of Metals.

17. Porter, D. E. and Easterling, K. E., Phase Transformations in Metals and Alloys. 1996, Cornwall: T.J. Press.

18. Wang, Y., Zeng, X. and Ding, W., *Effect of Al-4Ti-5B Master Alloy on the Grain Refinement of AZ31 Magnesium Alloy.* Acta Materialia, 2005. **54**: p. 269-273.

19. Kurz, W. and Fisher, D. J., Fundamentals of Solidification. 4th ed. 1998, Aedermannsdorf: Trans-Tech. Publications.

20. Dahle, A. K. and Arnberg, L., *On the Assumption of an Additive Effect of Solute Elements in Dendrite Growth.* Materials Science and Engineering A, 1997. **A225**: p. 38-46.

21. Gourlay, C. M. and Dahle, A. K., *Dilatant Shear Bands in Solidifying Metals.* Nature, 2007. **445**: p. 70-73.

22. Dobrzanski, L. A., Maniara, R., Sokolowski, J. and Kasprzak, W., *Effect of Cooling Rate on the Solidification Behavior of AC AlSi7Cu2 Alloy.* Journal of Materials Processing Technology, 2007. **191**: p. 317-320.

23. Chavez-Zamarripa, R., Ramos-Salas, J. A., Talamantes-Silva, J., Valtierra, S. and Colas, R., *Determination of the Dendrite Coherency Point During Solidification by Means of Thermal Diffusivity Analysis.* Metallurgical and Materials Transactions A, 2007. **A38**: p. 1875-1879.

24. Malekan, M. and Shabestari, S., *Effect of Grain Refinement on the Dendrite Coherency Point During Solidification of the A319 Aluminum Alloy.* Metallurgical and Materials Transactions A, 2009. **A40**: p. 3196-3203.

25. Veldman, N., Dahle, A. K., StJohn, D. and Arnberg, L., *Dendrite Coherency of Al-Si-Cu Alloys.* Metallurgical and Materials Transactions A, 2001. **A32**(1): p. 147-155.

26. Backerud, L., Krol, E. and Tamminen, J., Solidification Characteristics of Aluminum Alloys. Volume 1: Wrought Alloys. 1986, Des Plaines: Tangen Trykk.

27. Chai, G., Backerud, L. and Arnberg, L., *Relation Between Grain size and Coherency Parameters in Aluminium Alloys.* Materials Science and Technology, 1995. **11**: p. 1099-1103.

28. Lee, Y. C., Dahle, A. K. and StJohn, D. H., *The Role of Solute in Grain Refinement of Magnesium.* Metallurgical and Materials Transactions A, 2000. **A31**: p. 2895-2906.

29. Chandrashekar, T., Muralidhara, M. K., Kashyap, K. T. and Ragothama Rao, P., *Effect of Growth Restricting Factor on Grain Refinement in Aluminum Alloys.* International Journal of Advanced Manufacturing Technology, 2009. **40**: p. 234-241.

30. Emley, F. E., Principles of Magnesium Technology. 1966, London: Pergamon Press.

31. Backerud, L. and Johnsson, M., *The Relative Importance of Nucleation and Growth Mechanisms to Control Grain Size in Various Aluminum Alloys.* Light Metals, 1996. : p. 679-685.

32. Elsayed, A., *Novel Grain Refinement of AZ91E Magnesium Alloy and the Effect on Hot Tearing During Solidification*. Thesis (Masters). 2010, Ryerson University. p. 102.

33. Backerud, L., Chai, G. and Tamminen, J., Solidification Characteristics of Aluminum Alloys. Volume 2: Foundry Alloys. 1990, Des Plaines: American Foundrymen's Society Inc.

34. Tempil. *Basic Guide to Ferrous Metallurgy*. February 1, 2011; Available from: <http://www.tempil.com/PDF/Basic_Guide.pdf>.

35. Tzimas, E. and Zavaliangos, A., *Evaluation of Volume Fraction of Solid in Alloys Formed by Semisolid Processing.* Journal of Materials Science, 2000. **35**: p. 5319-5329.

APPENDIX A COOLING CURVES AND RHEOLOGICAL PLOTS

A.1 A319 Alloy

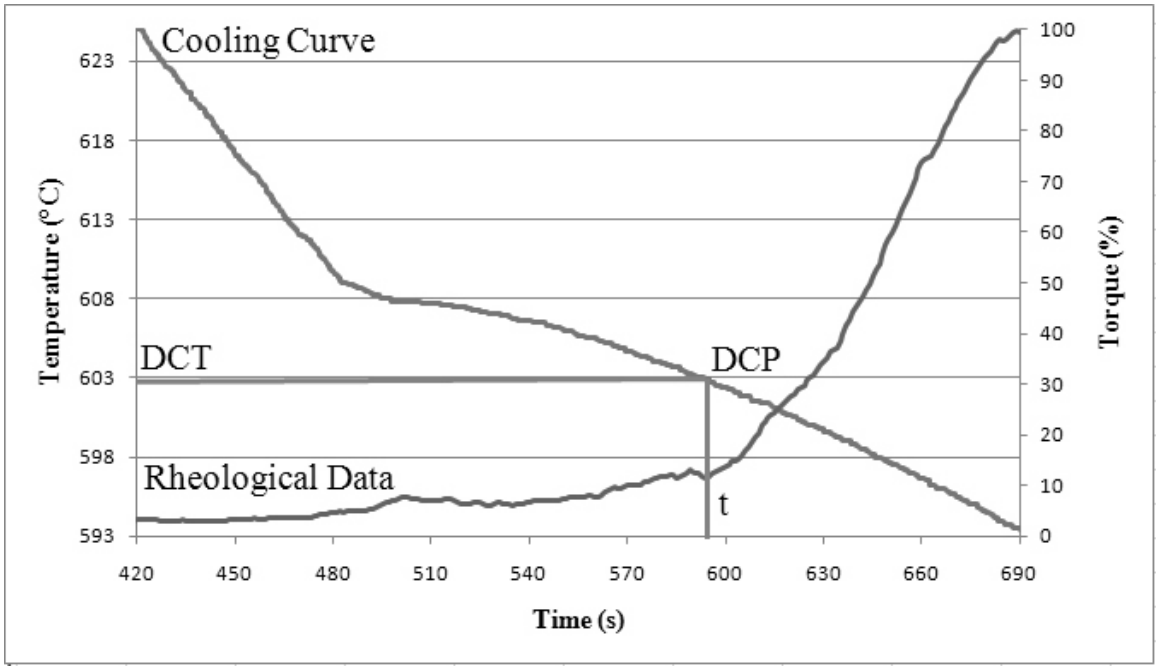

Figure A.1.1. Repeat rheological data and cooling curve for preheated spindle at 0.5 RPM spindle speed.

A.2 AZ91 Base Alloy

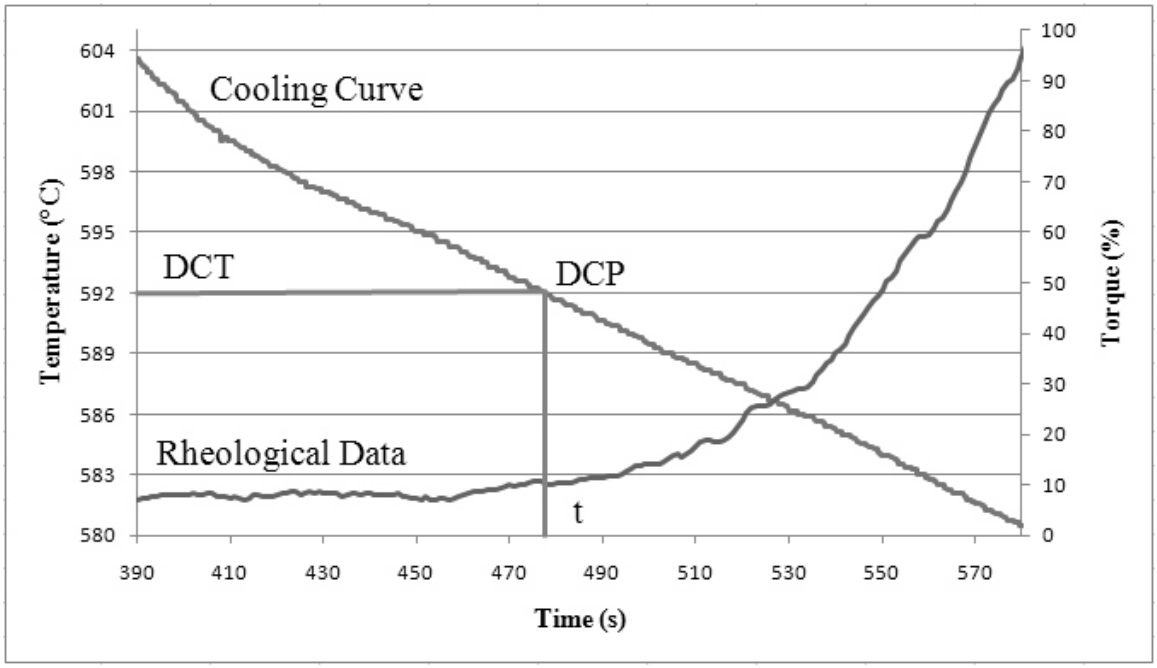

Figure A.2.1. First rheological data and cooling curve for AZ91 base alloy.

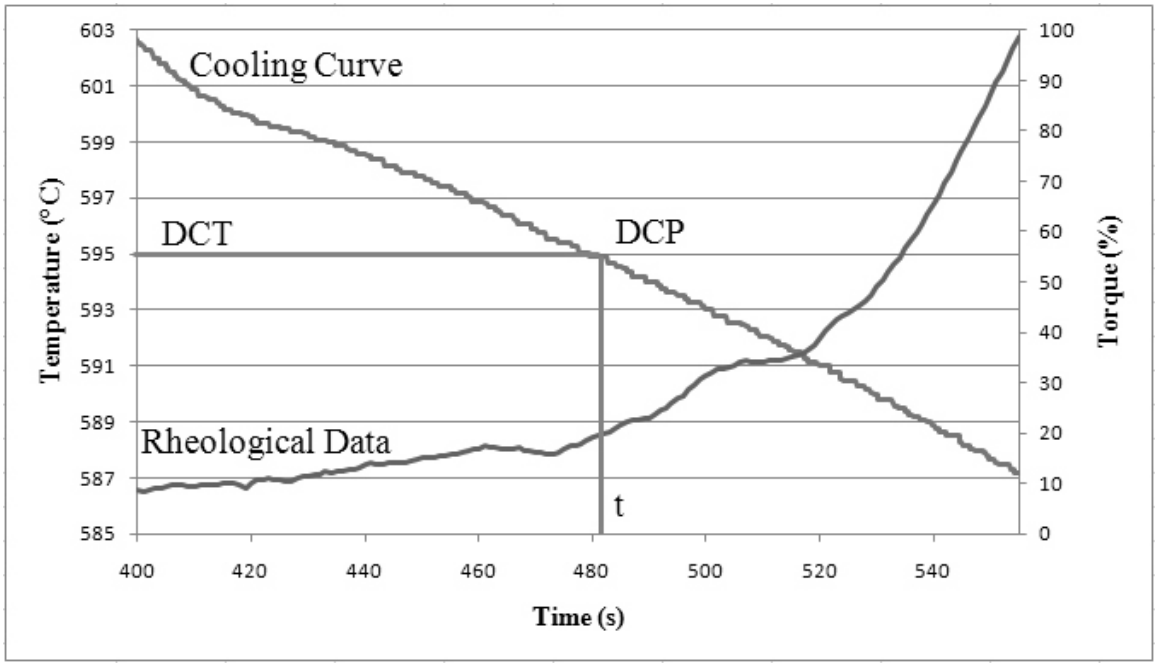

Figure A.2.2. Second rheological data and cooling curve for AZ91 base alloy.

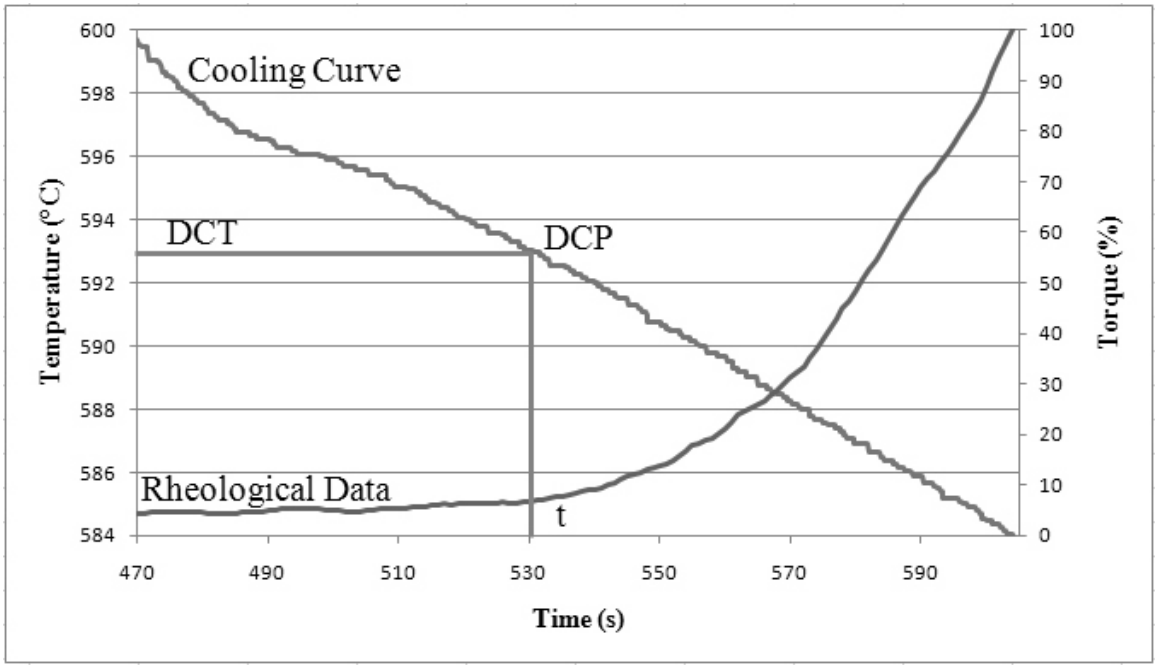

Figure A.2.3. Third rheological data and cooling curve for AZ91 base alloy.

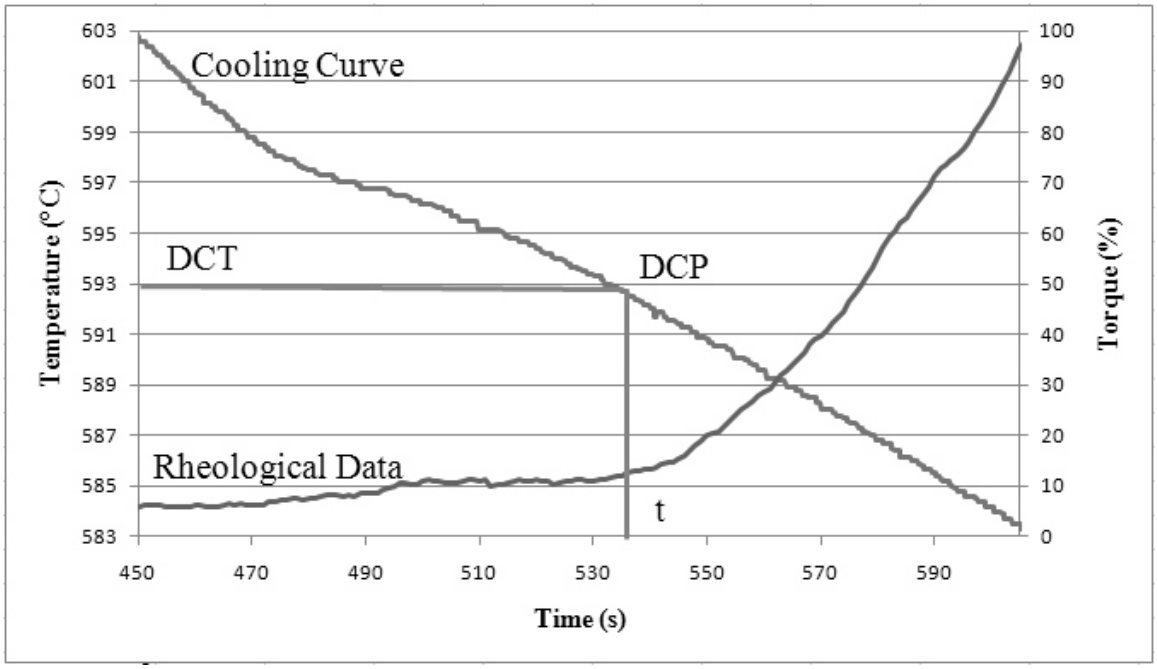

Figure A.2.4. Fourth rheological data and cooling curve for AZ91 base alloy.

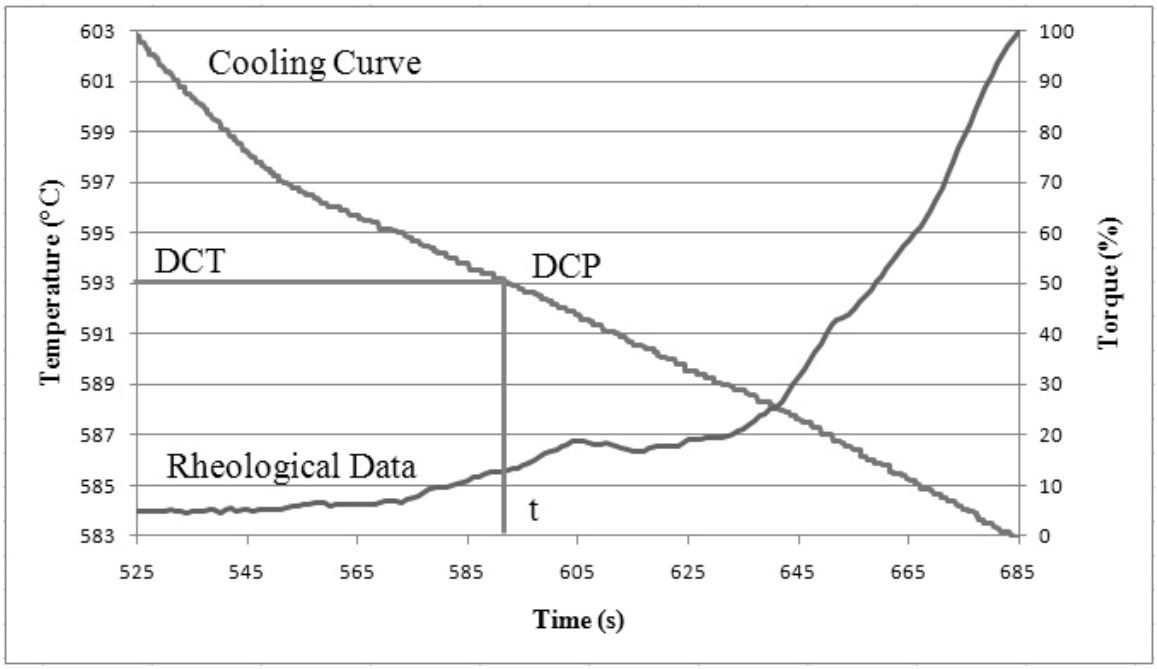

Figure A.2.5. Fifth rheological data and cooling curve for AZ91 base alloy.

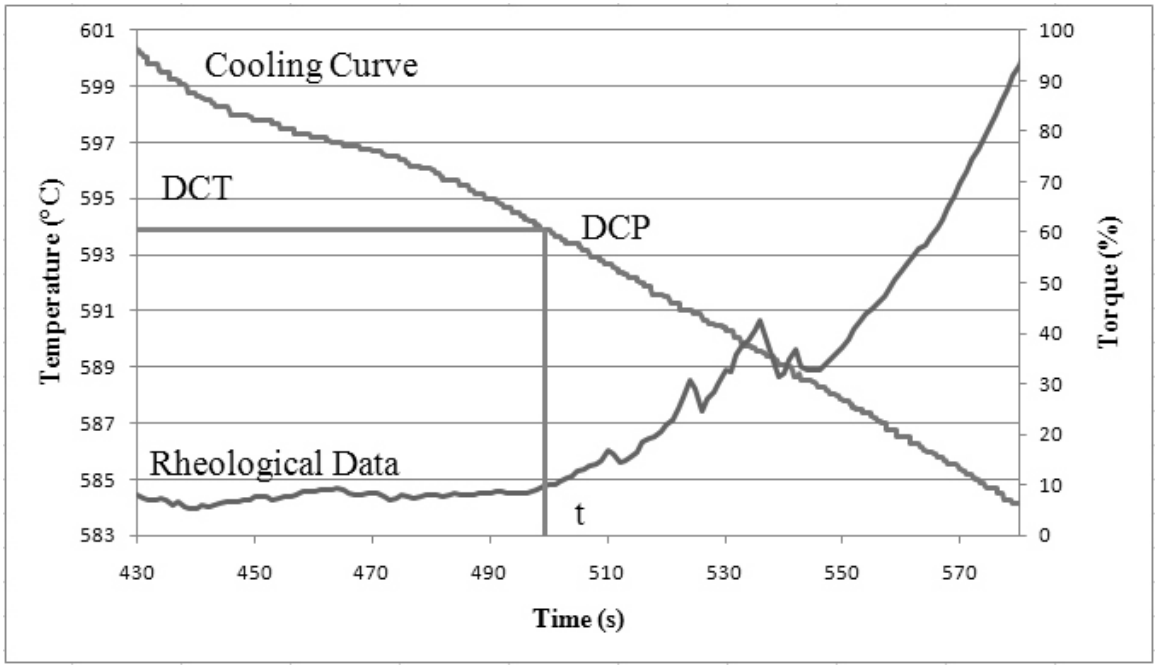

Figure A.2.6. Sixth rheological data and cooling curve for AZ91 base alloy.

A.3 AZ91 Base Alloy at 0.005 wt.% Ti Addition Level

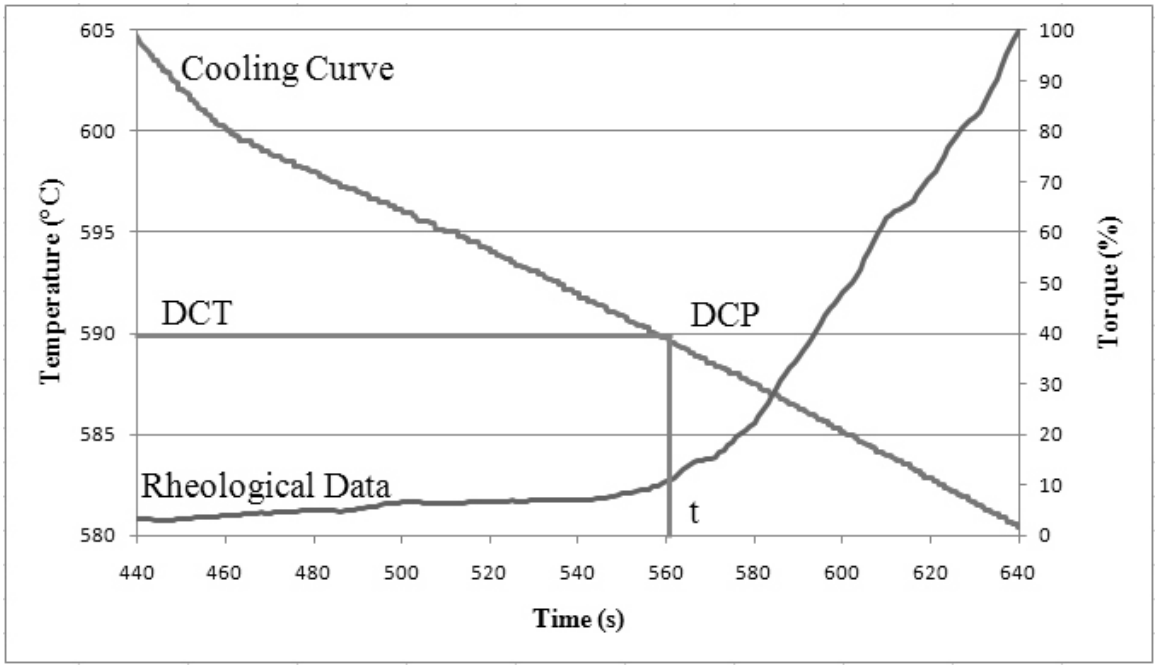

Figure A.3.1. First rheological data and cooling curve for AZ91 alloy at 0.005 wt.% Ti level.

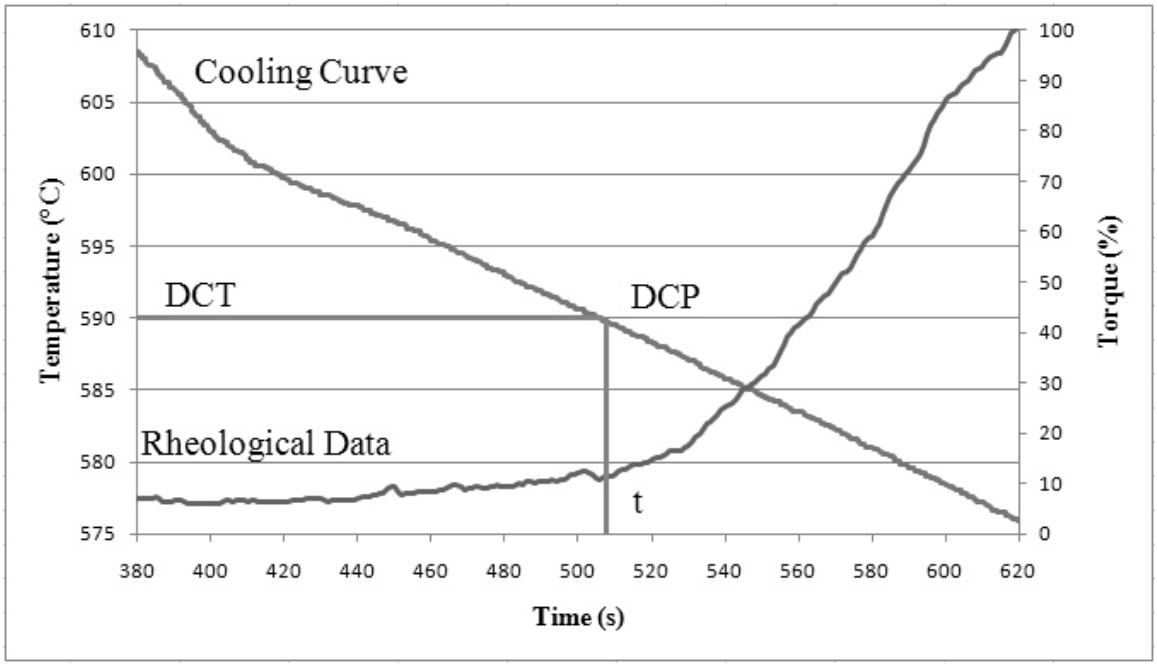

Figure A.3.2. Second rheological data and cooling curve for AZ91 alloy at 0.005 wt.% Ti level.

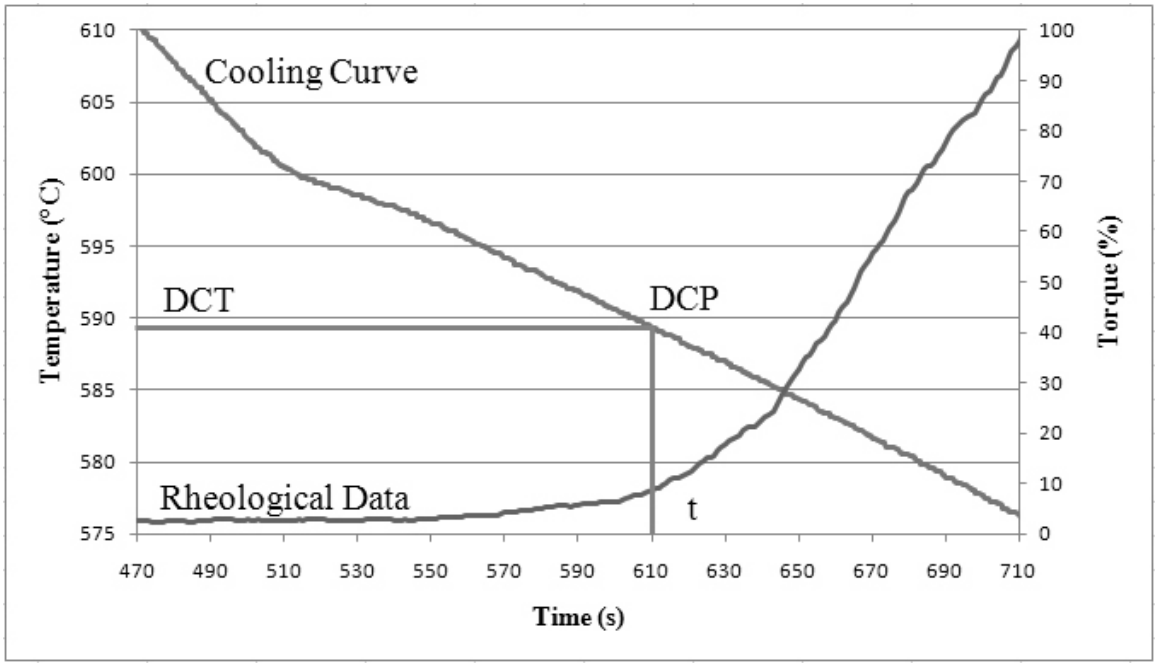

Figure A.3.3. Third rheological data and cooling curve for AZ91 alloy at 0.005 wt.% Ti level.

A.4 AZ91 Base Alloy at 0.05 wt.% Ti Addition Level

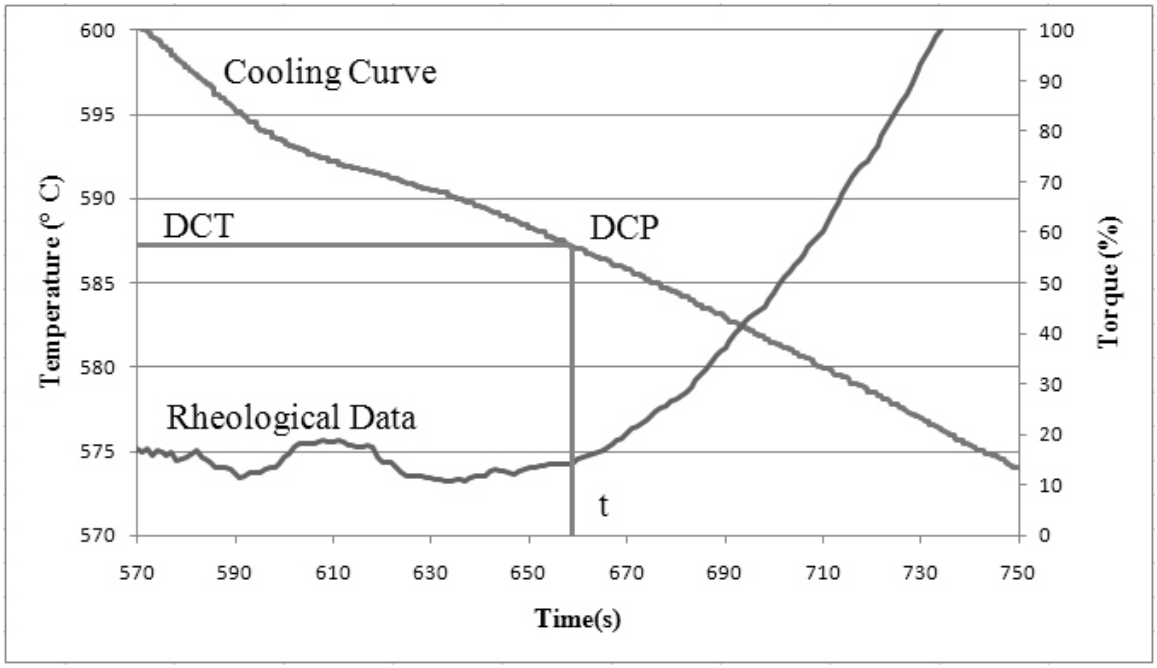

Figure A.4.1. First rheological data and cooling curve for AZ91 alloy at 0.05 wt.% Ti level.

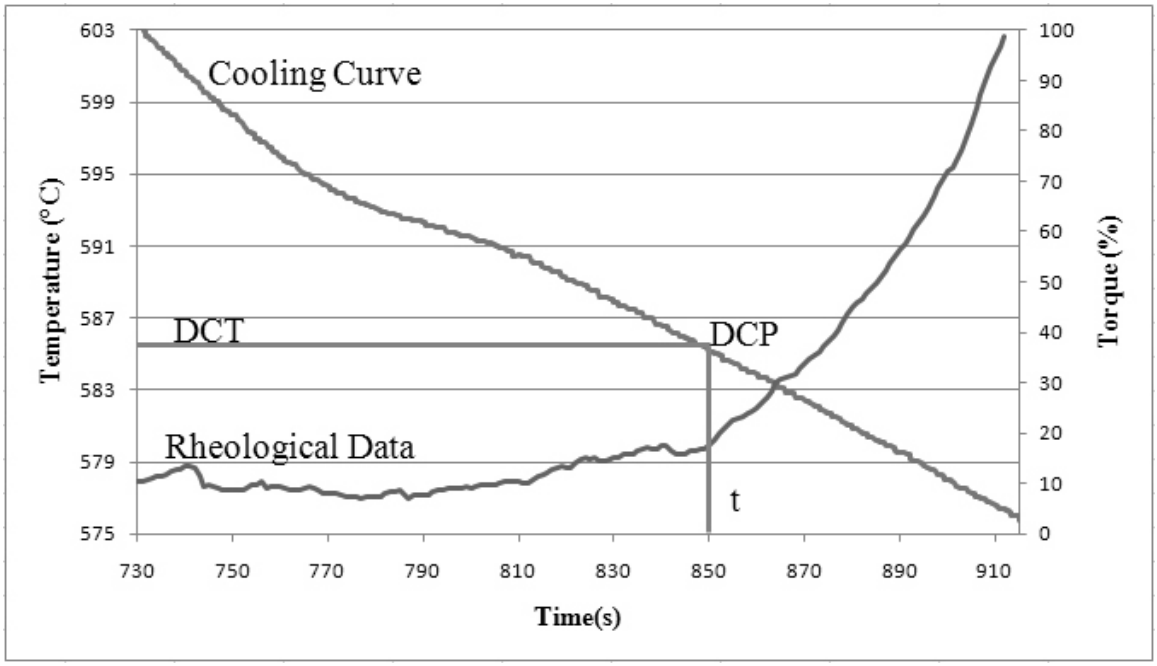

Figure A.4.2. Second rheological data and cooling curve for AZ91 alloy at 0.05 wt.% Ti level.

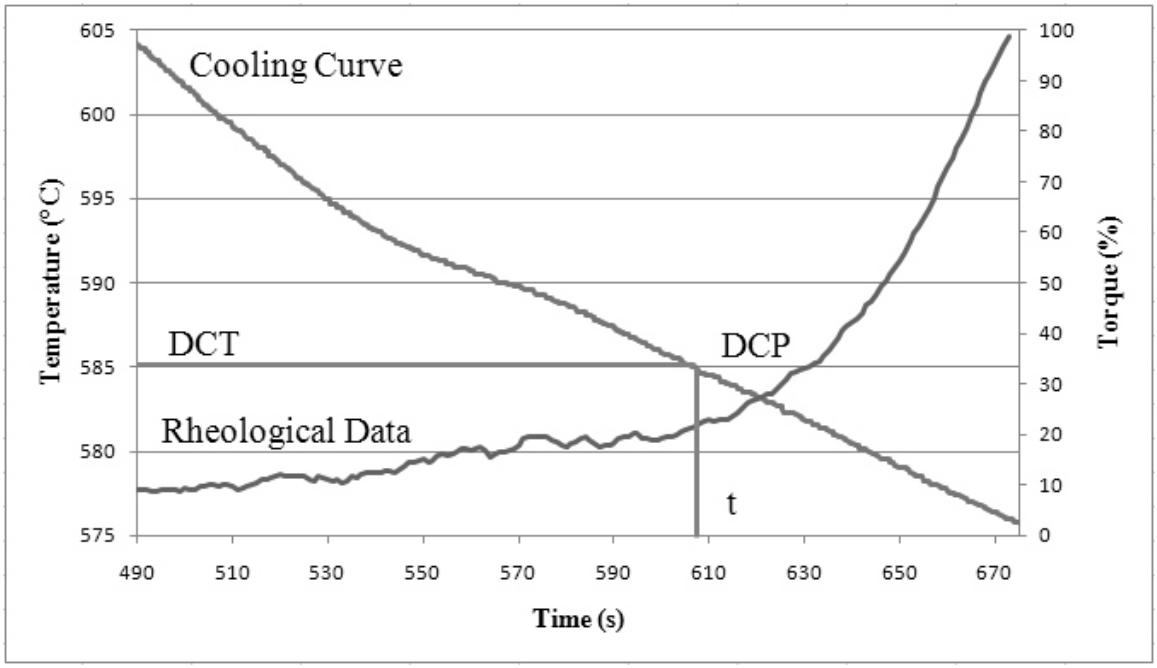

Figure A.4.3. Third rheological data and cooling curve for AZ91 alloy at 0.05 wt.% Ti level.

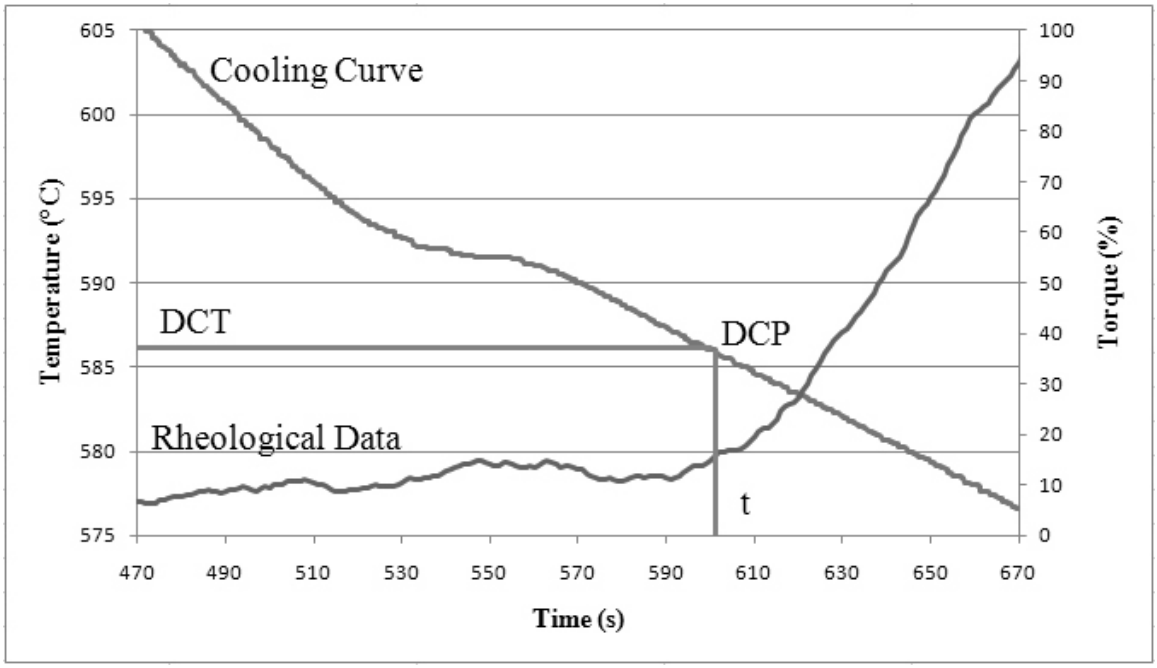

Figure A.4.4. Fourth rheological data and cooling curve for AZ91 alloy at 0.05 wt.% Ti level.

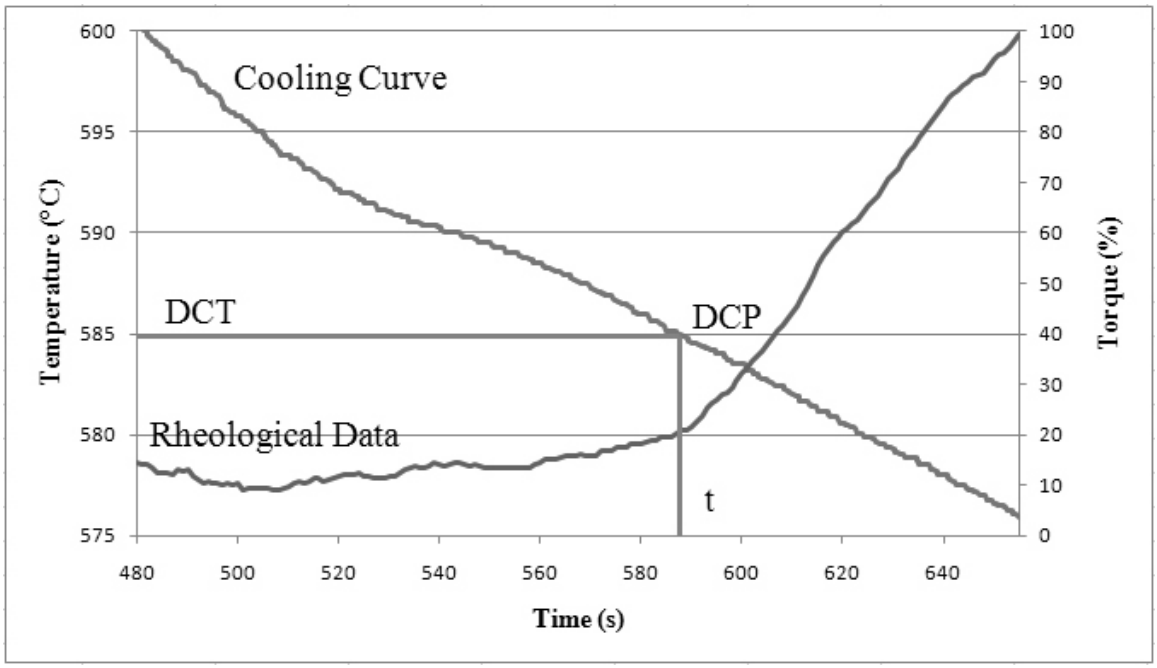

Figure A.4.5. Fifth rheological data and cooling curve for AZ91 alloy at 0.05 wt.% Ti level.

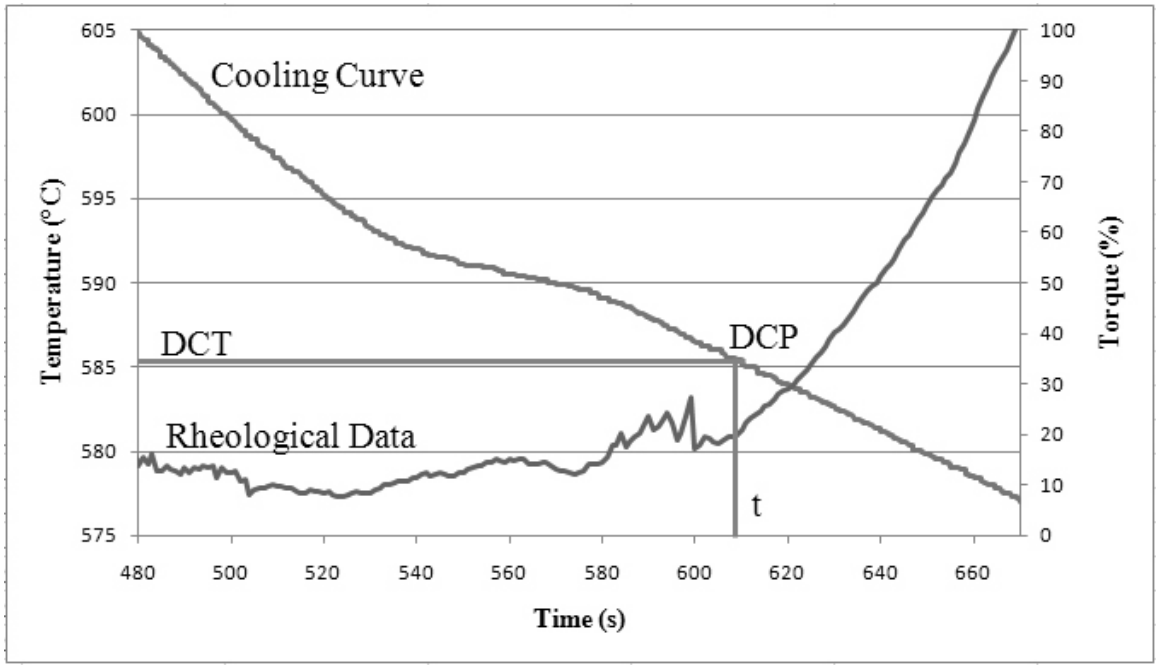

Figure A.4.6. Sixth rheological data and cooling curve for AZ91 alloy at 0.05 wt.% Ti level.

A.5 AZ91 Base Alloy at 0.10 wt.% Ti Addition Level

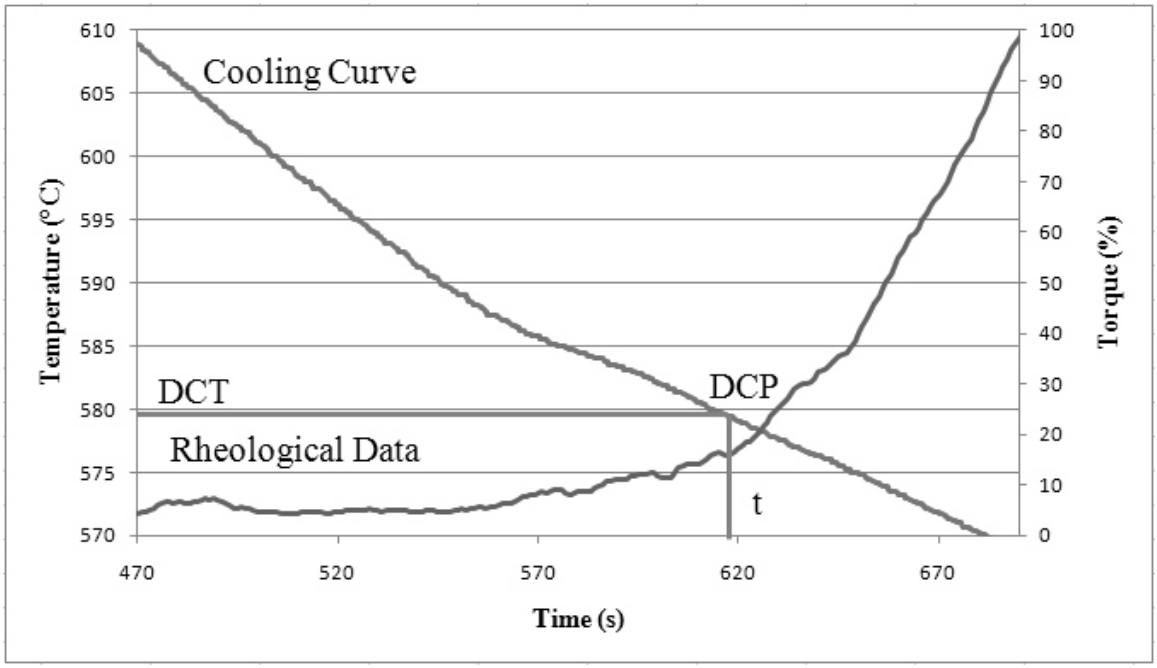

Figure A.5.1. First rheological data and cooling curve for AZ91 alloy at 0.10 wt.% Ti level.

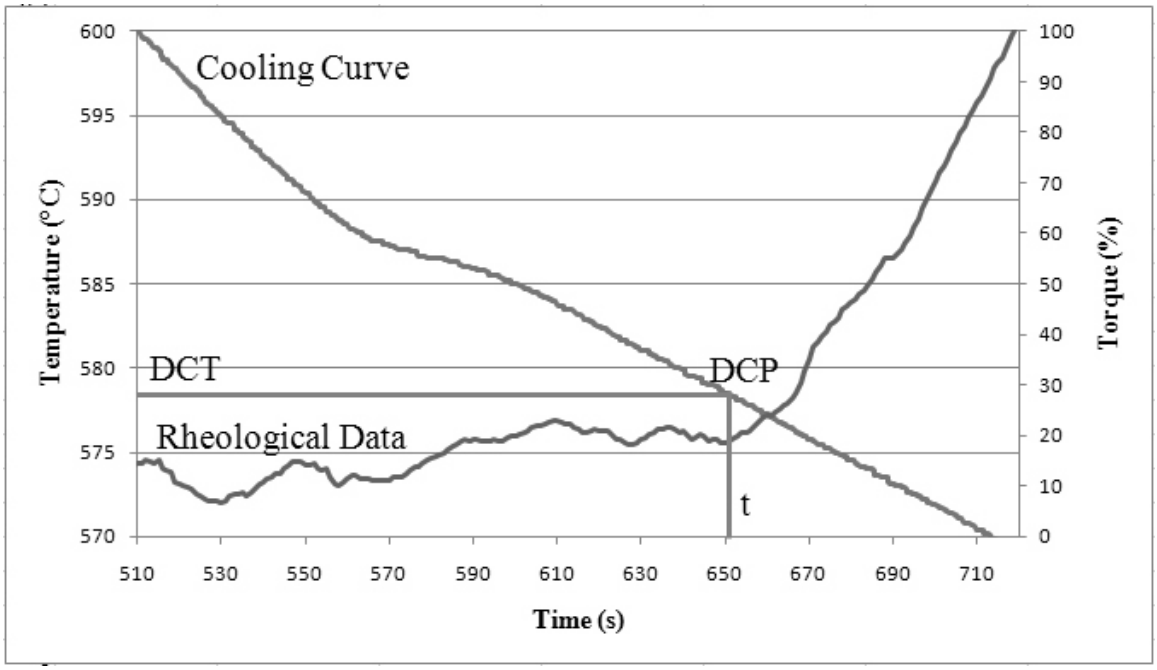

Figure A.5.2. Second rheological data and cooling curve for AZ91 alloy at 0.10 wt.% Ti level.

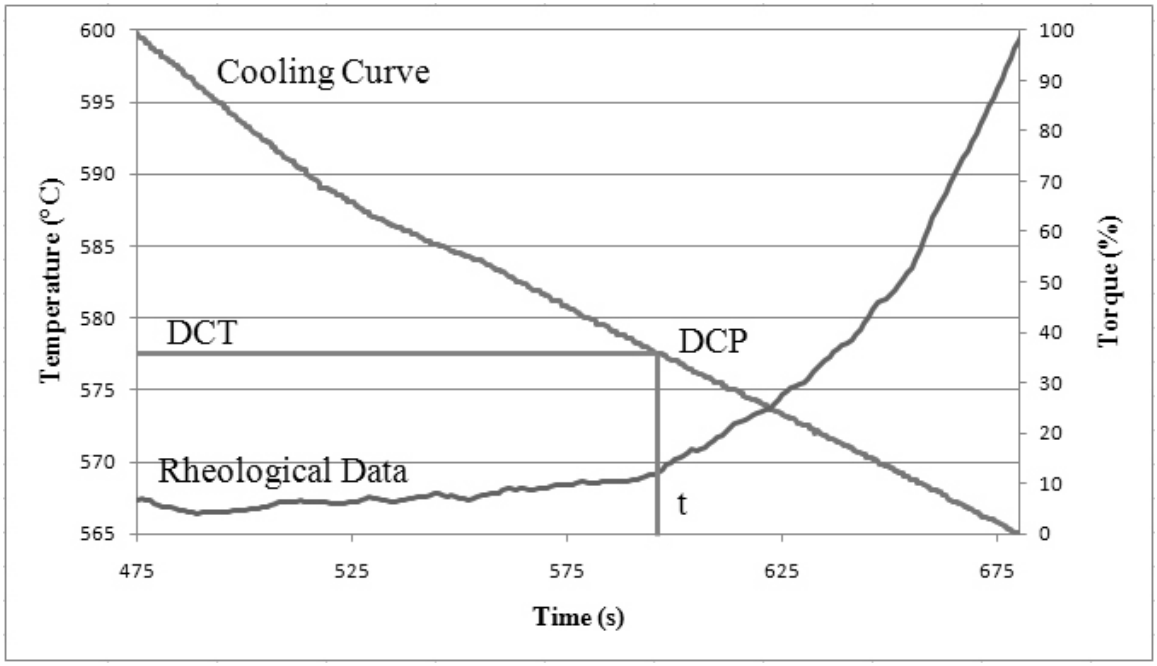

Figure A.5.3. Third rheological data and cooling curve for AZ91 alloy at 0.10 wt.% Ti level.

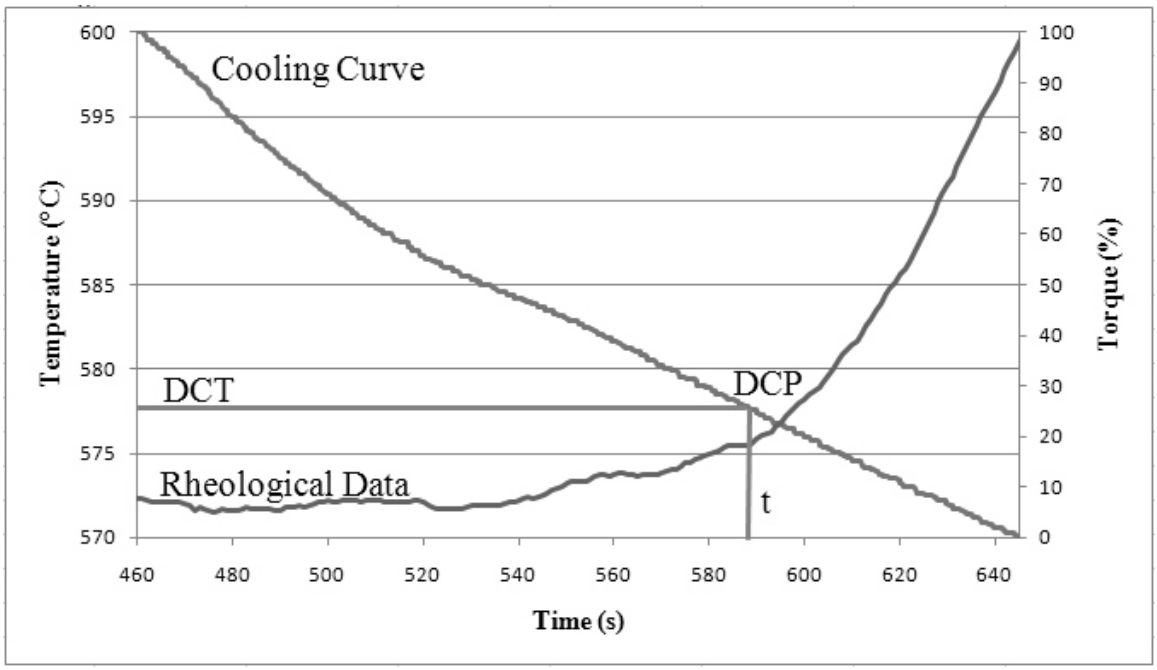

Figure A.5.4. Fourth rheological data and cooling curve for AZ91 alloy at 0.10 wt.% Ti level.

A.6 AZ91 Base Alloy at 0.20 wt.% Ti Addition Level

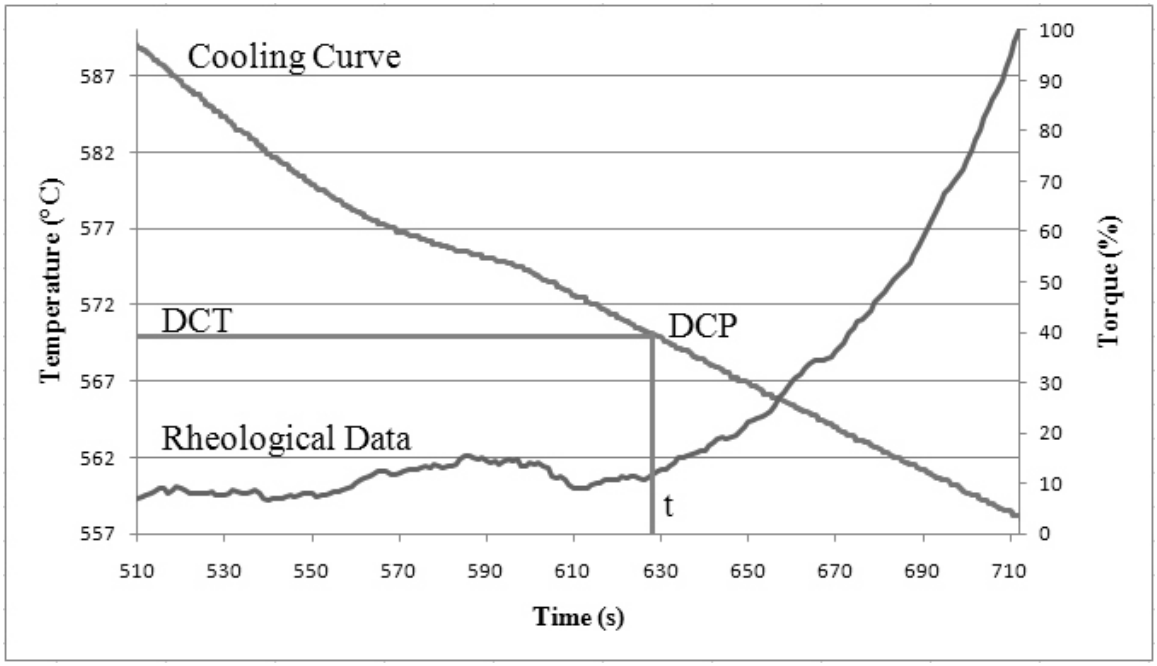

Figure A.6.1. First rheological data and cooling curve for AZ91 alloy at 0.20 wt.% Ti level.

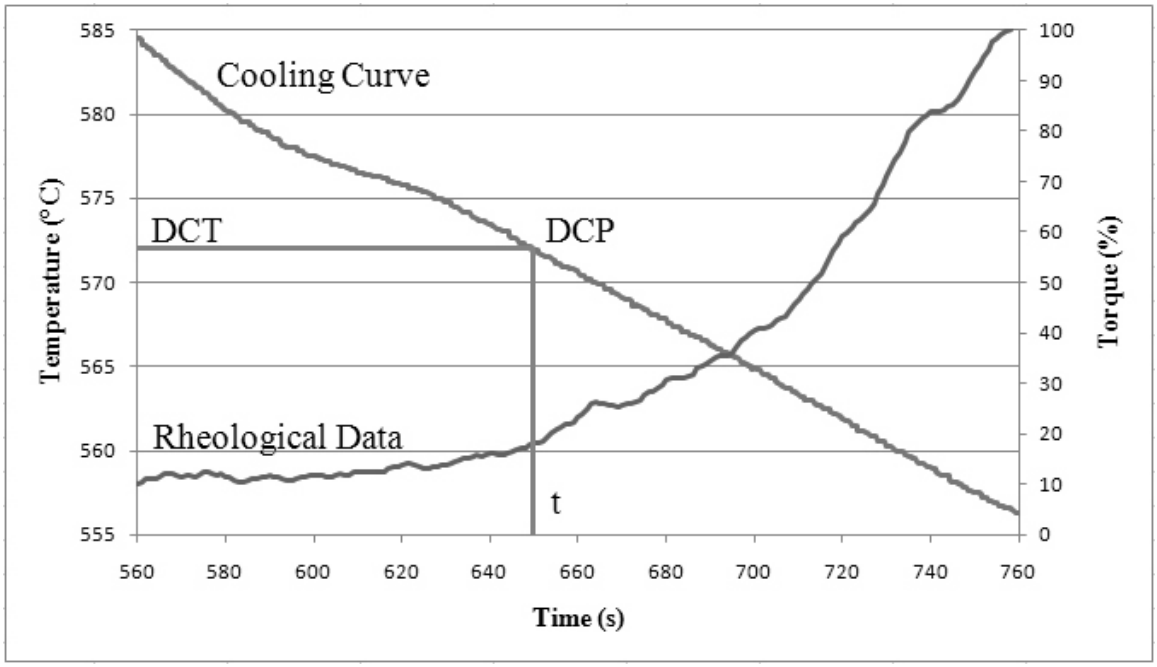

Figure A.6.2. Second rheological data and cooling curve for AZ91 alloy at 0.20 wt.% Ti level.

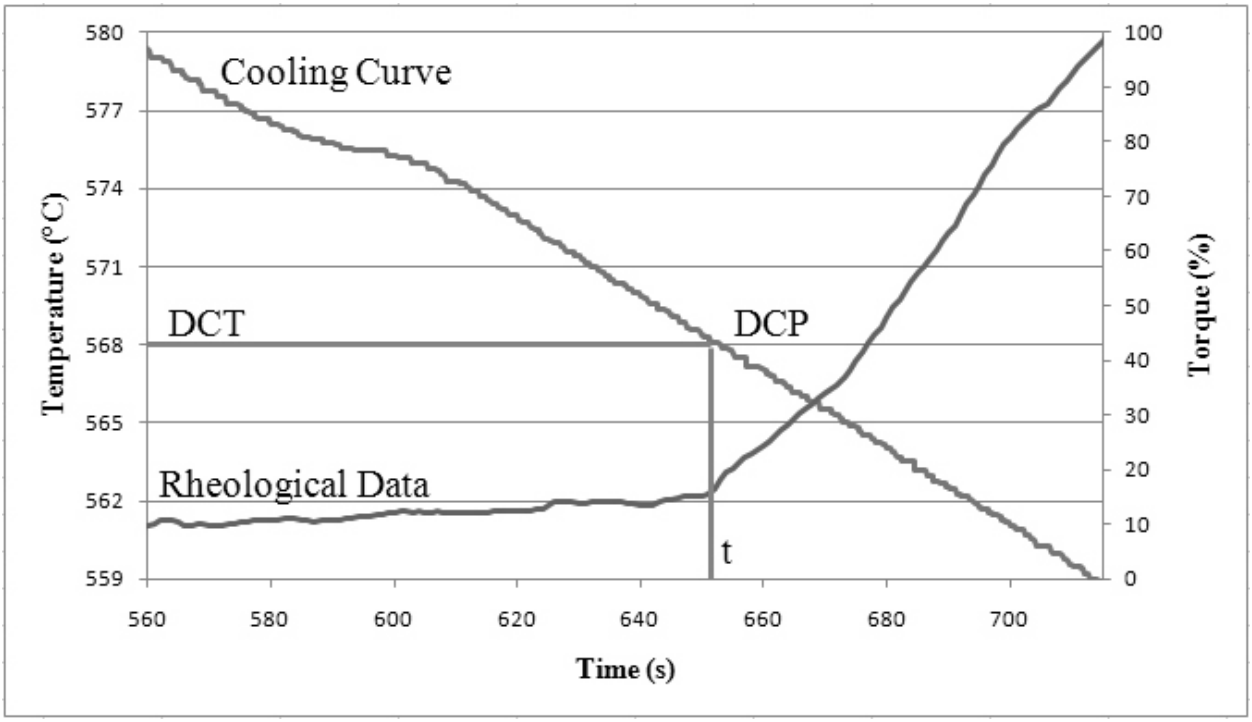

Figure A.6.3. Third rheological data and cooling curve for AZ91 alloy at 0.20 wt.% Ti level.

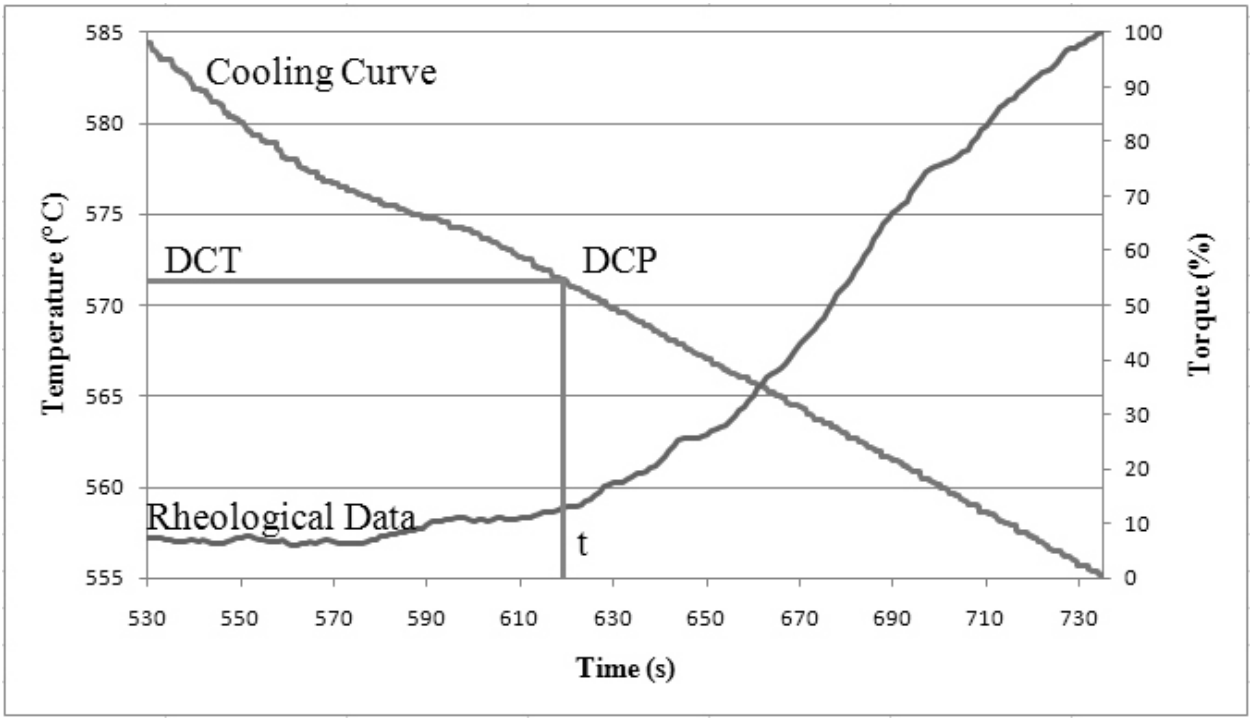

Figure A.6.4. Fourth rheological data and cooling curve for AZ91 alloy at 0.20 wt.% Ti level.

A.7 AZ91 Base Alloy at 0.30 wt.% Ti Addition Level

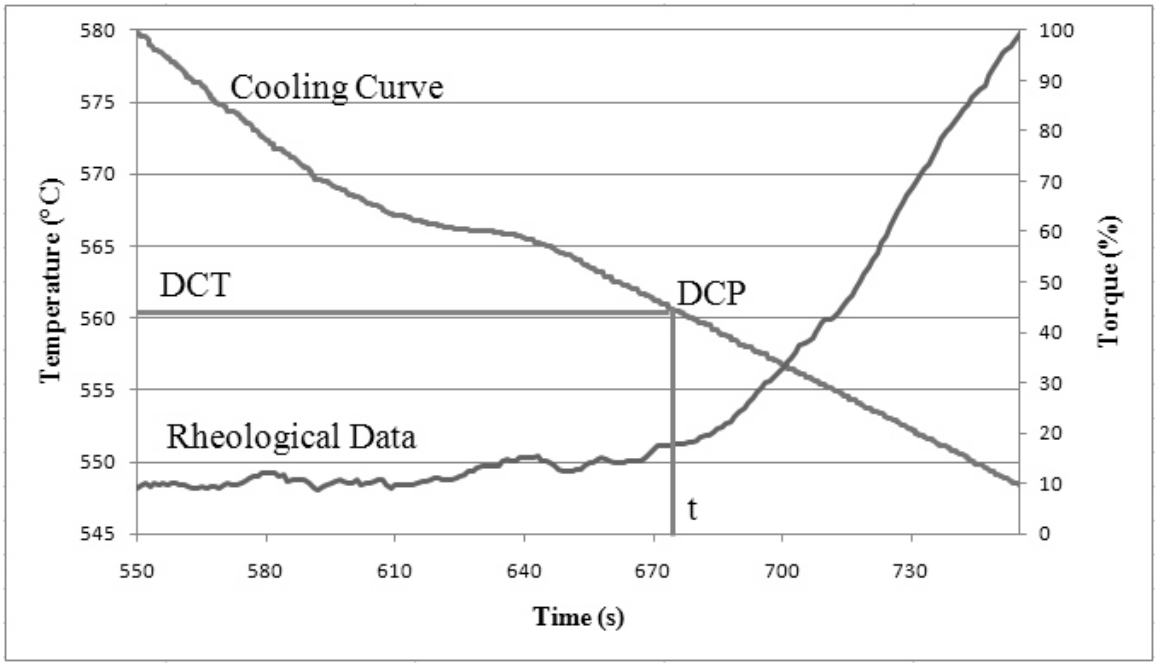

Figure A.7.1. First rheological data and cooling curve for AZ91 alloy at 0.30 wt.% Ti level.

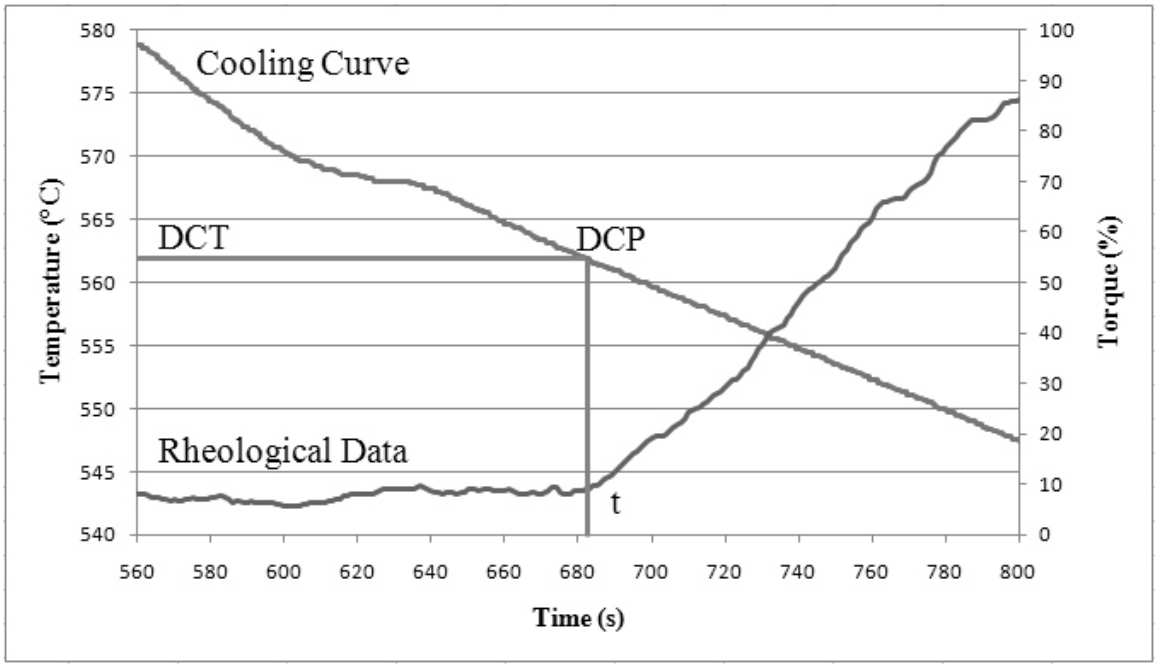

Figure A.7.2. Second rheological data and cooling curve for AZ91 alloy at 0.30 wt.% Ti level.

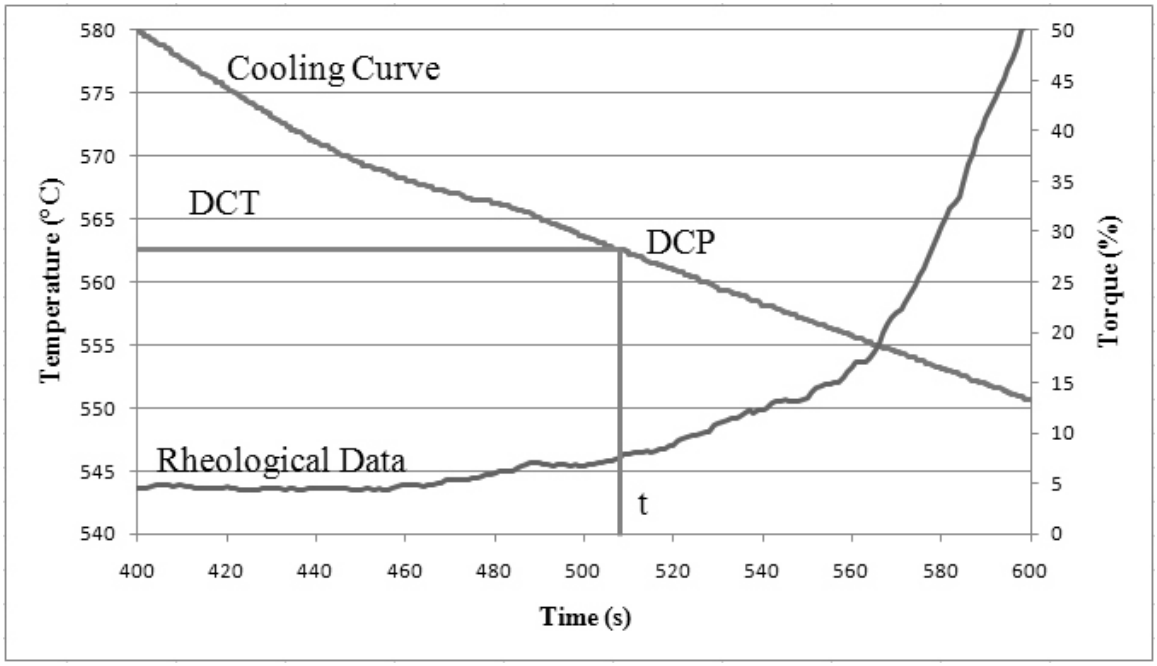

Figure A.7.3. Third rheological data and cooling curve for AZ91 alloy at 0.30 wt.% Ti level.

APPENDIX B RHEOLOGICAL EXPERIMENTS SEM

B.1 AZ91 Base Alloy at 0.30 wt.% Ti Addition Level

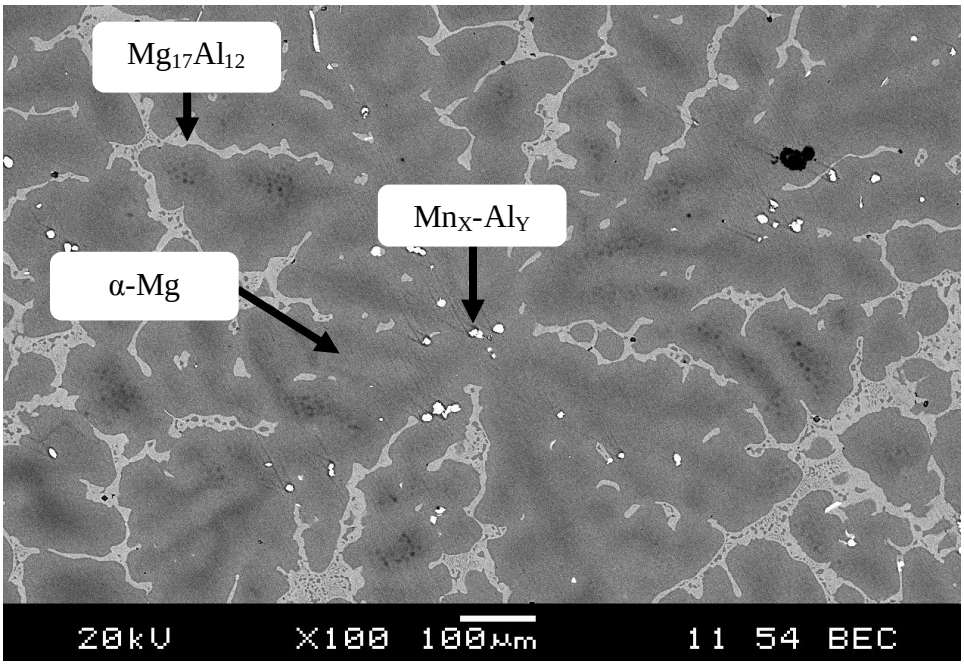

a)

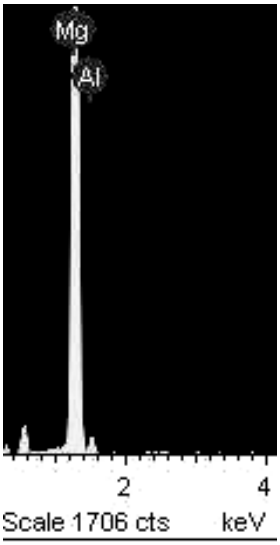

b)

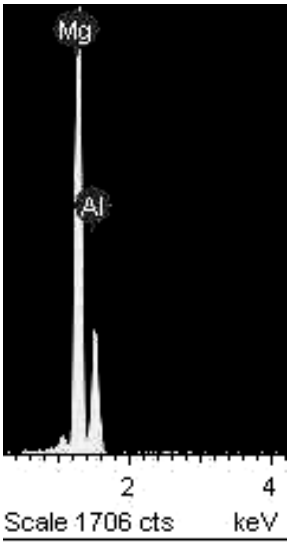

c)

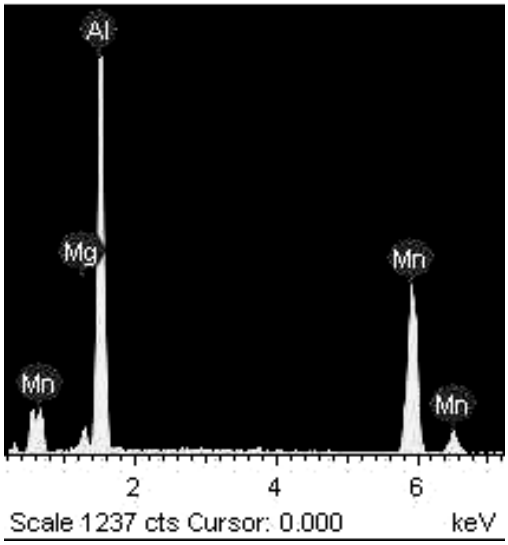

d)

Figure B.1.1. SEM micrograph of AZ91E alloy at the 0.3 wt.% Ti addition level showing a) general microstructure and EDX scans of b) primary α-Mg, c) $Mg_{17}Al_{12}$, and d) Mn_X-Al_Y phases.

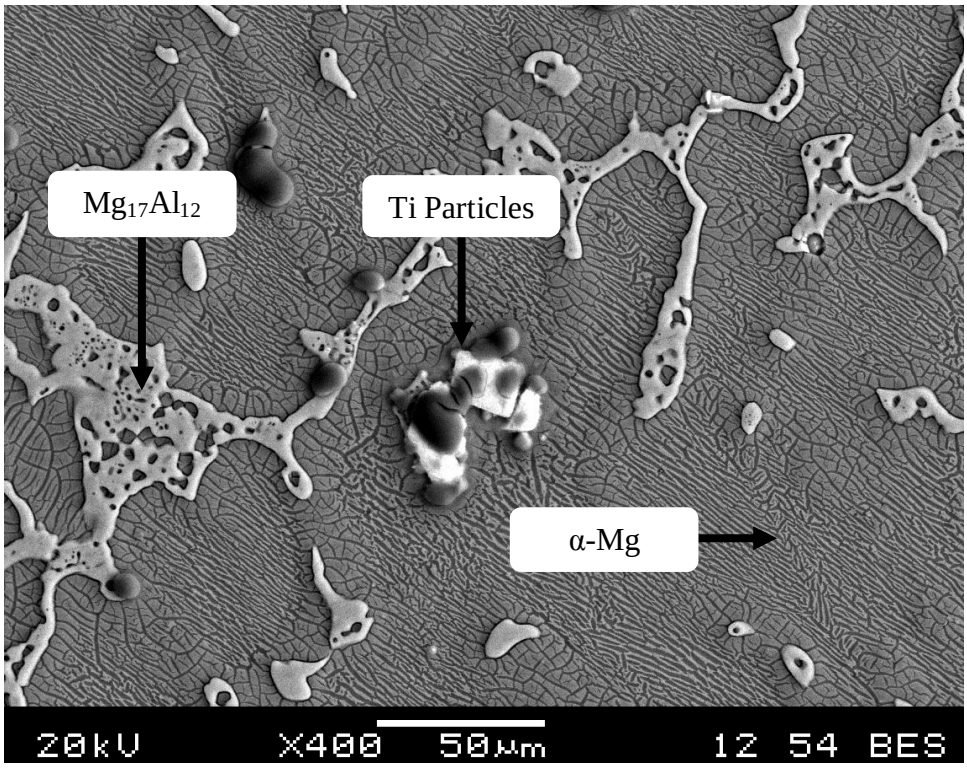

a)

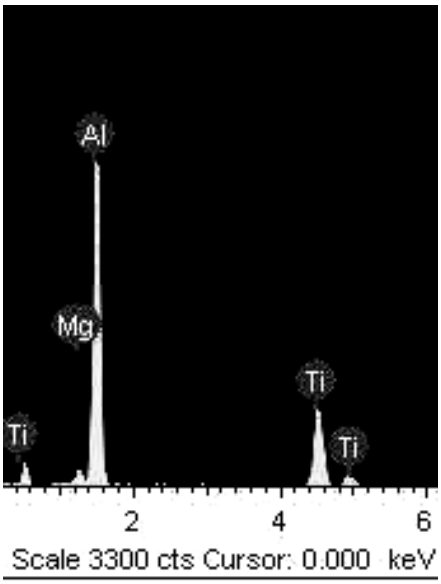

b)

Figure B.1.2. a) SEM micrograph and b) EDX for a rhelogical sample at the 0.3 wt.% Ti addition level illustrating the segregation of Ti particles at the eutectic region.

APPENDIX C QUENCH EXPERIMENTS SEM

C.1 AZ91 Base Alloy at 0.005 wt.% Ti Addition Level

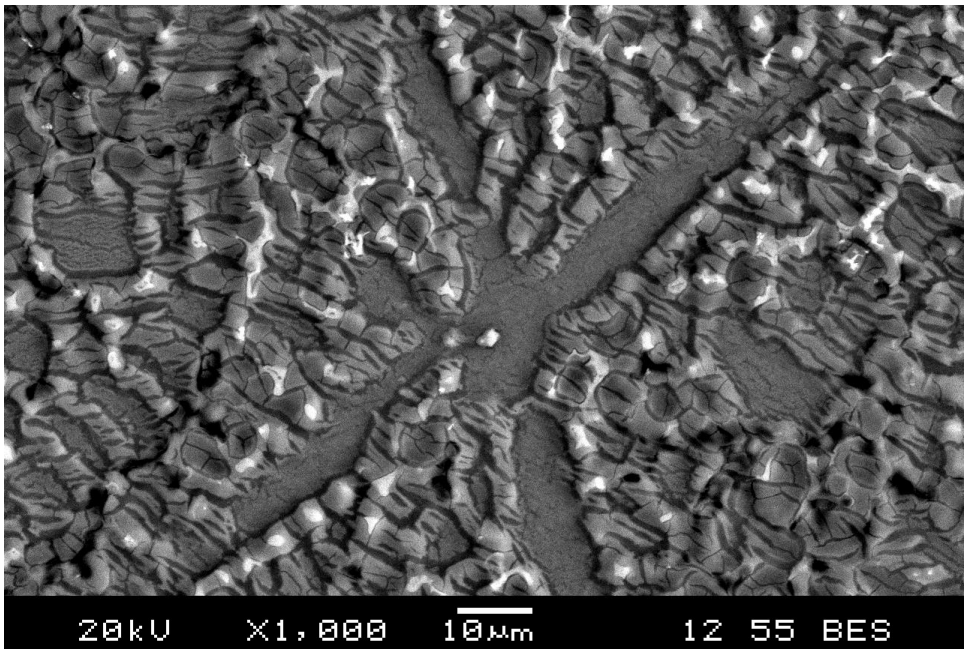

a)

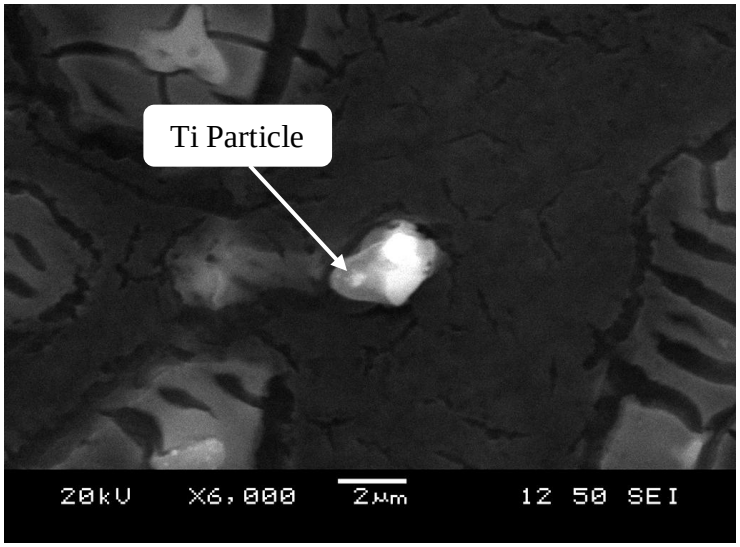

b)

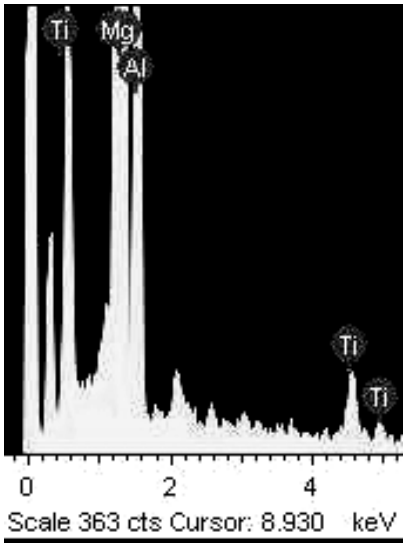

c)

Figure C.1.1. SEM micrograph at one location illustrating a) dendritic structure, b) enlarged view of Ti particle at the centre of dendrite, and c) EDX of Ti particle.

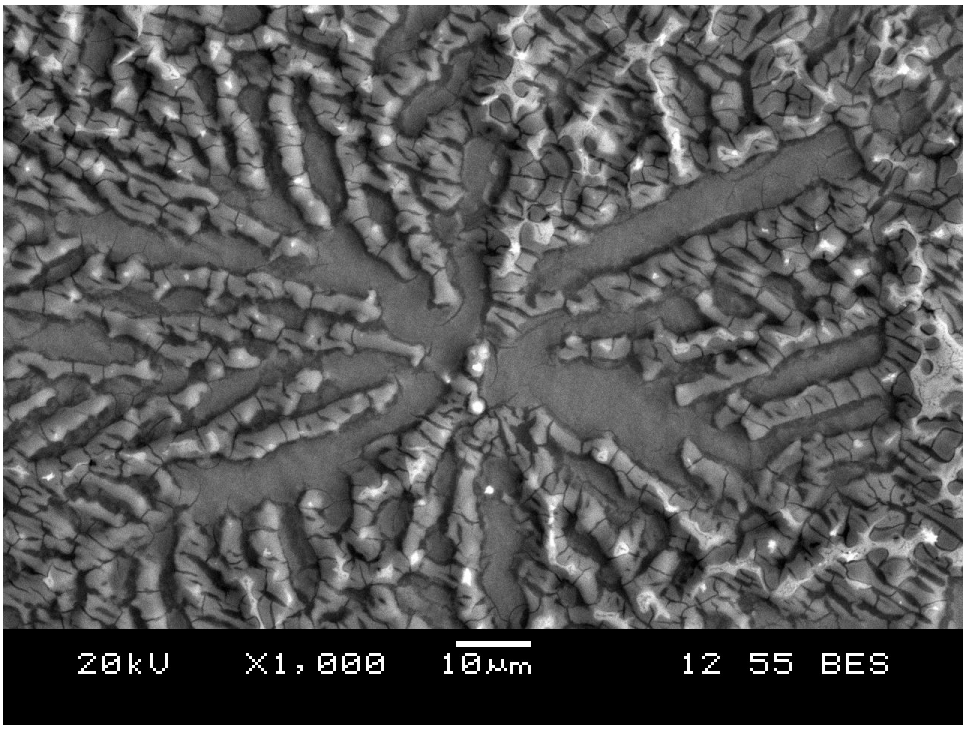

a)

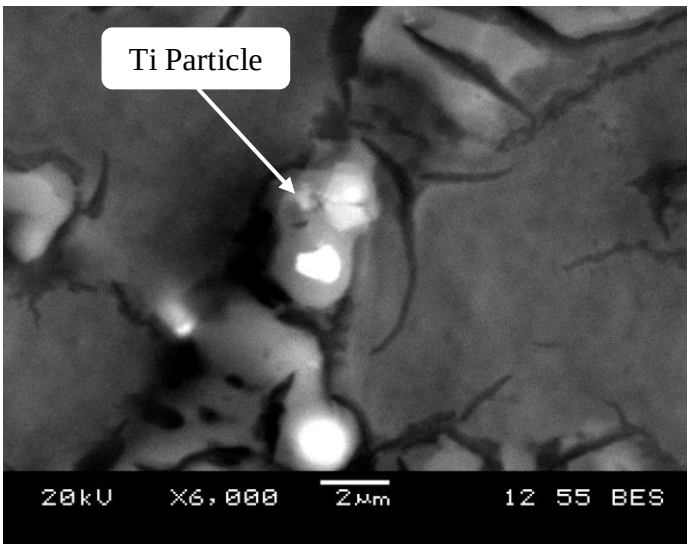

c)

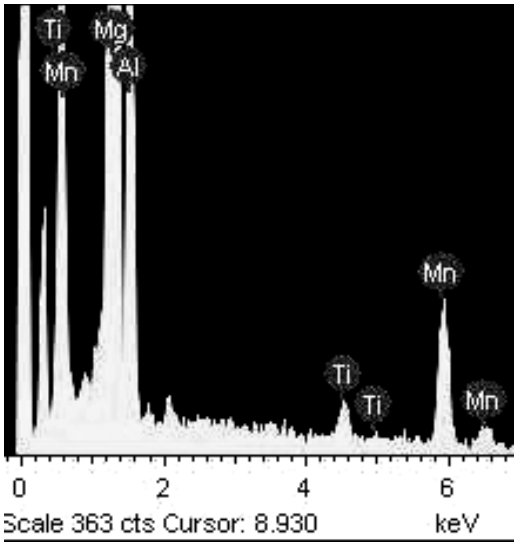

d)

Figure C.1.2. SEM micrograph at a second location illustrating a) dendritic structure, b) enlarged view of Ti particle at the centre of dendrite, and c) EDX of Ti particle.

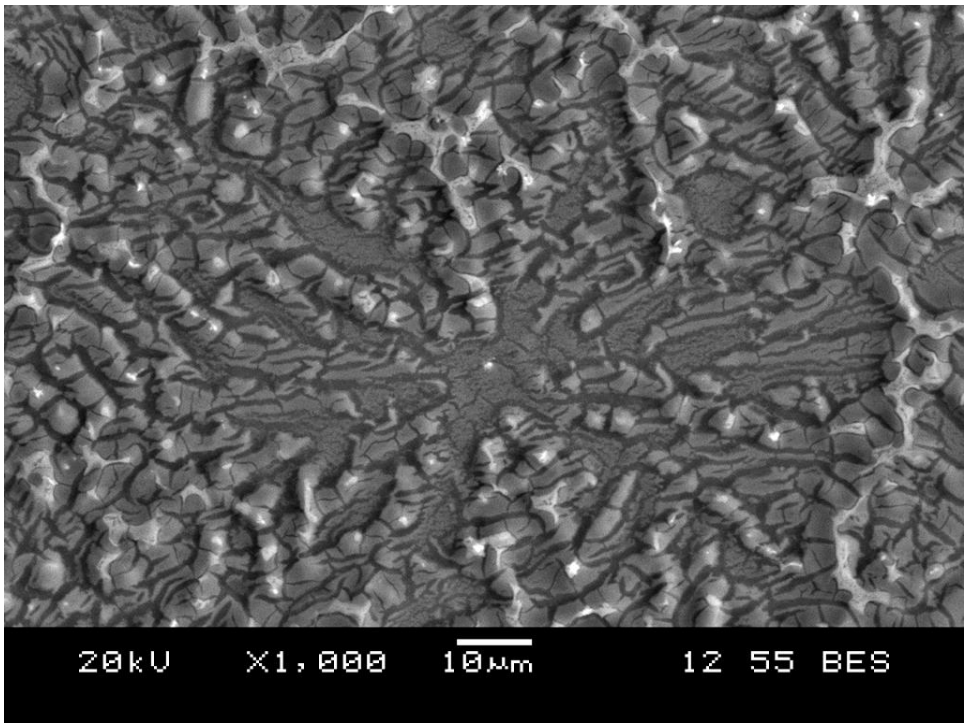

a)

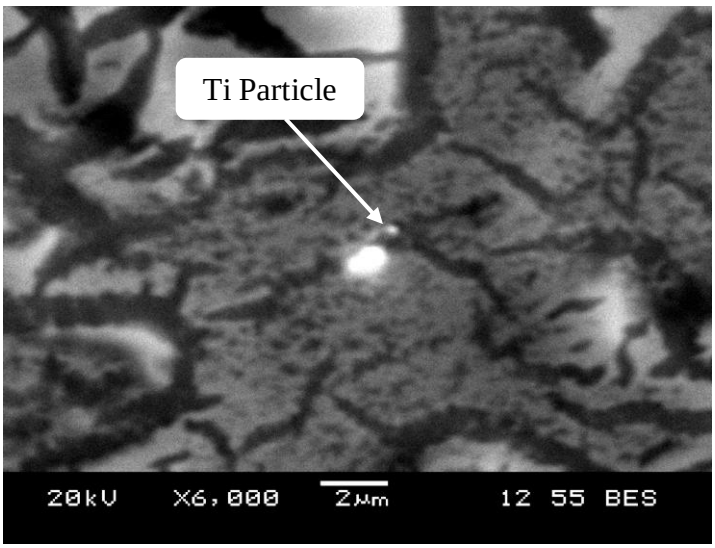

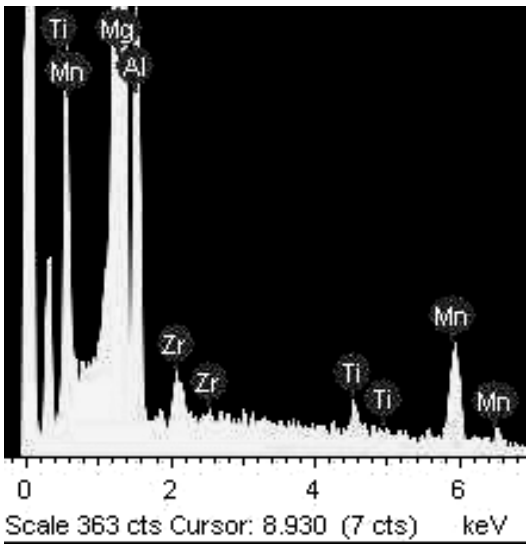

b) c)

Figure C.1.3. SEM micrograph at a third location illustrating a) dendritic structure, b) enlarged view of Ti particle at the centre of dendrite, and c) EDX of Ti particle.

C.2 AZ91 Base Alloy at 0.05 wt.% Ti Addition Level

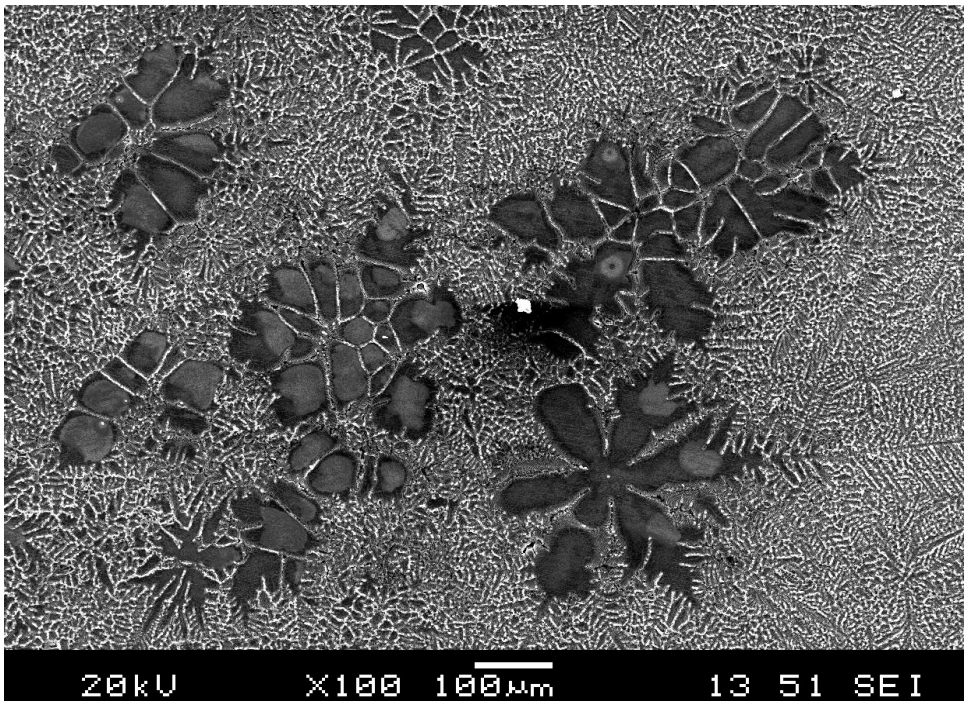

Figure C.2.1. SEM micrograph at the transition stage from equiaxed to lancet dendrites.

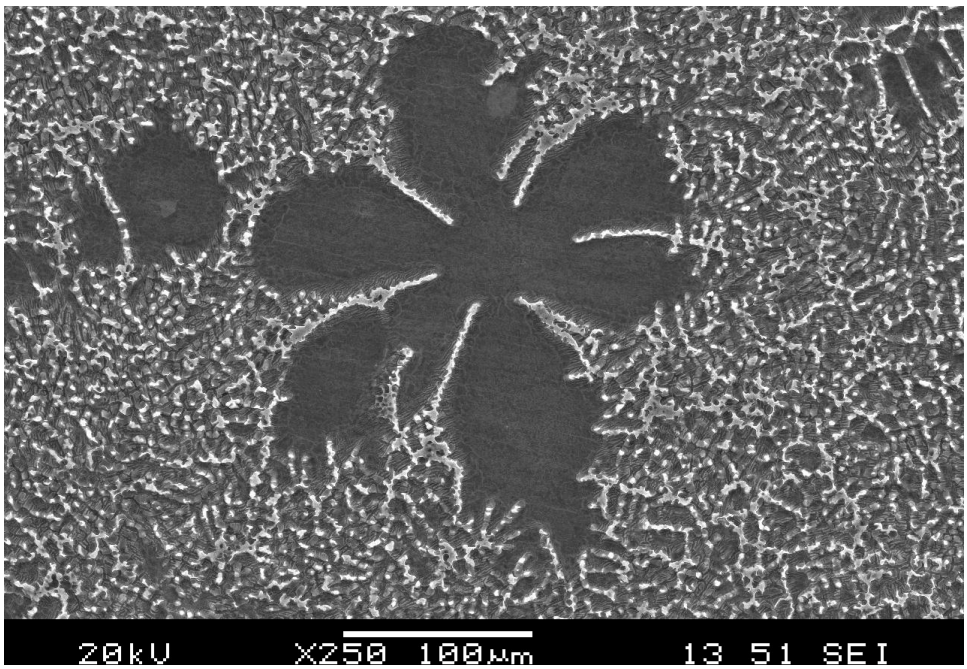

Figure C.2.2. A second SEM micrograph at the transition stage from equiaxed to lancet dendrites.

C.3 AZ91 Base Alloy at 0.10 wt.% Ti Addition Level

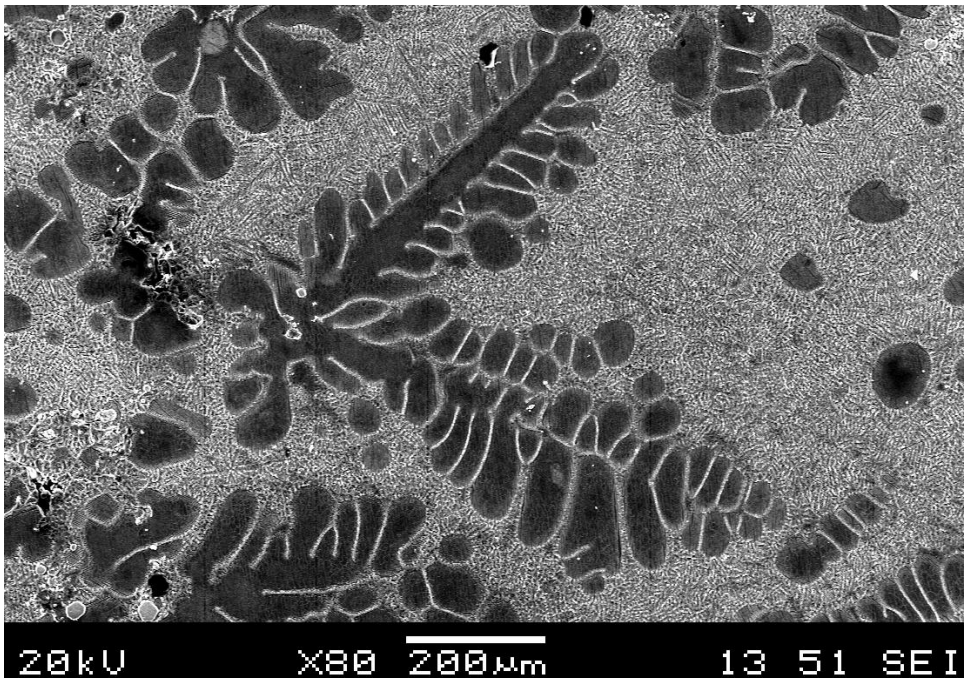

Figure C.3.1. SEM micrograph illustrating progressively more lancet dendritic structure.

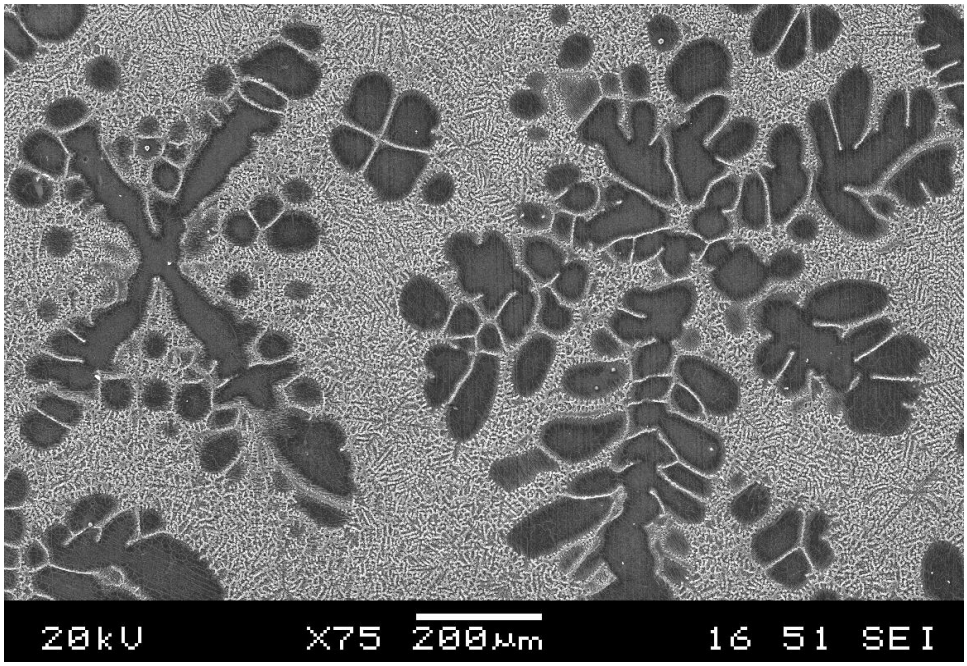

Figure C.3.2. A second SEM micrograph illustrating progressively more lancet dendritic structure.

C.4 AZ91 Base Alloy at 0.20 wt.% Ti Addition Level

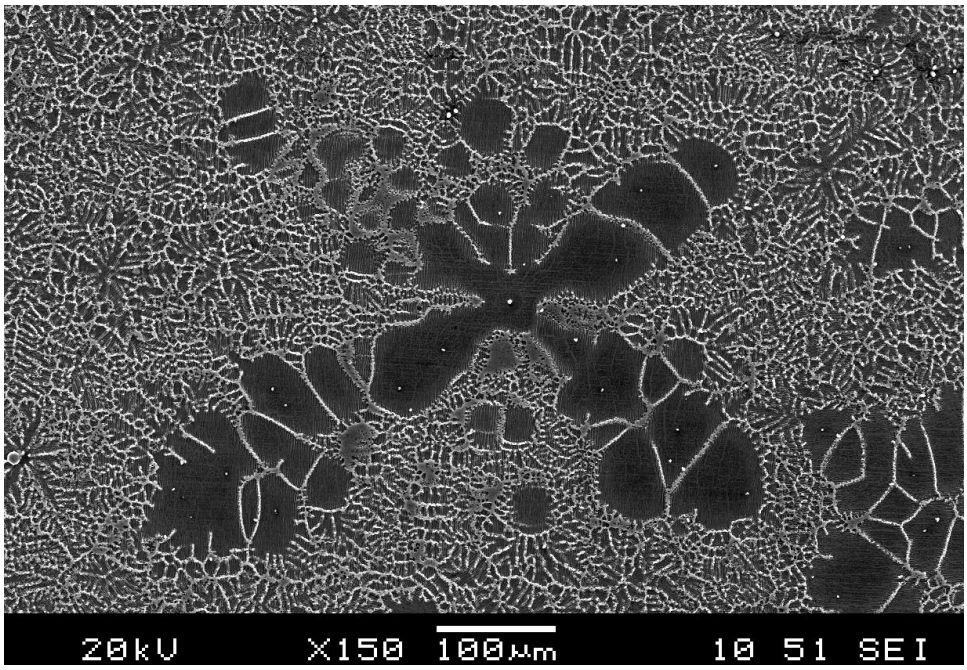

Figure C.4.1. SEM micrograph illustrating the lancet dendritic morphology.

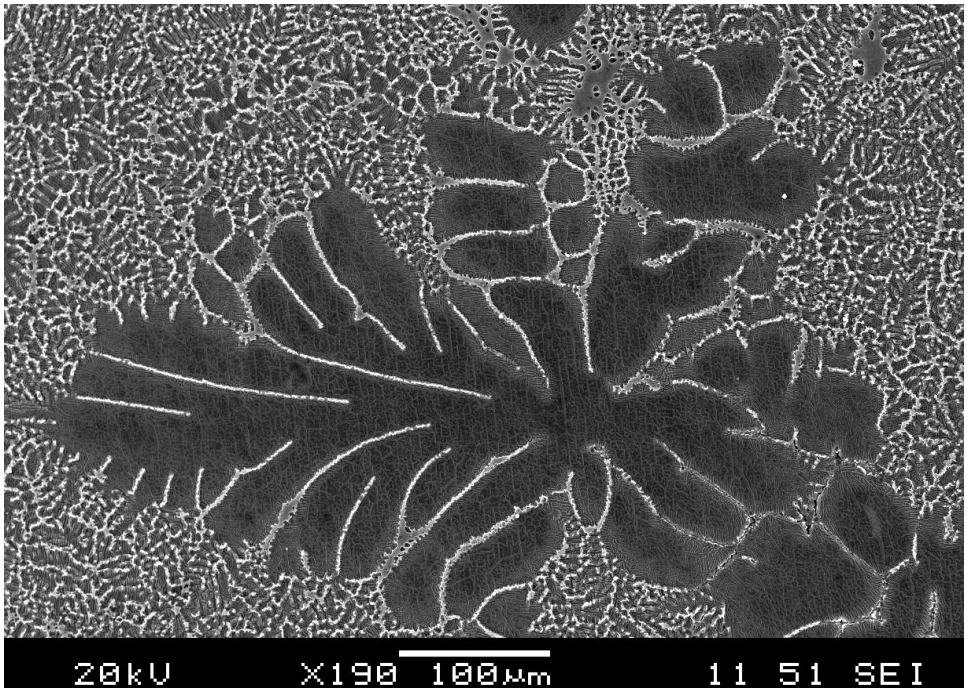

Figure C.4.2. A second SEM micrograph illustrating the lancet dendritic morphology.

C.5 AZ91 Base Alloy at 0.30 wt.% Ti Addition Level

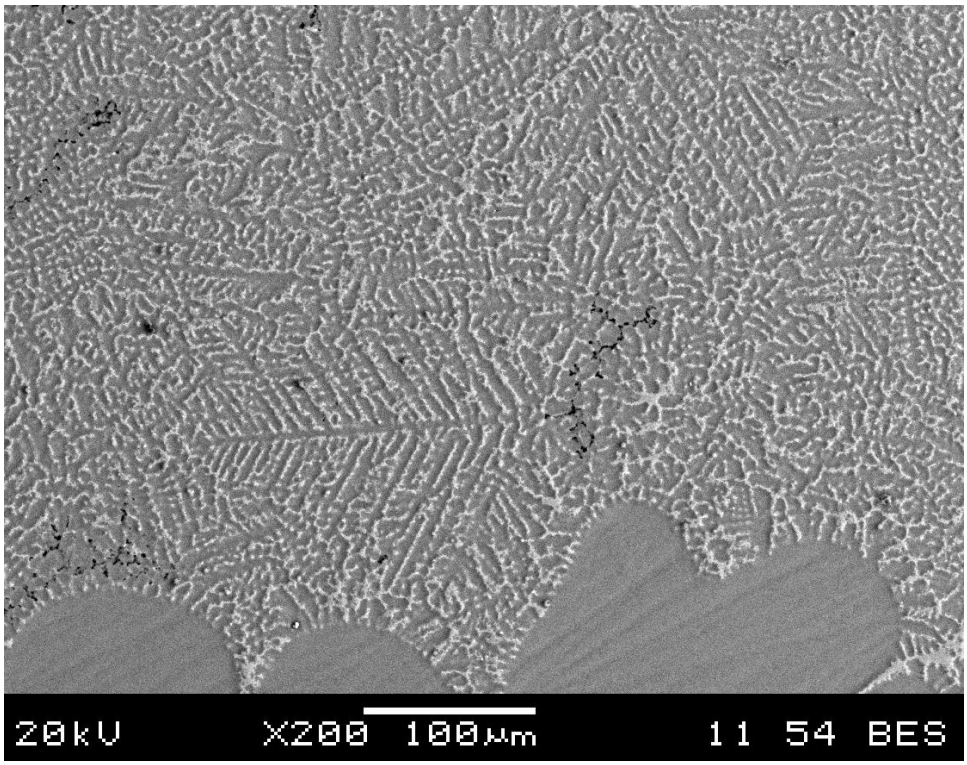

Figure C.5.1. SEM micrograph illustrating the lancet dendritic morphology.

APPENDIX D ANOVA ANALYSIS

The purpose of the ANOVA test is to determine if the means of a group are equal. The null hypothesis in ANOVA is that the sample means of the groups compared are equal. If the null hypothesis is true, the groups tested belong to the same population. However, if the null hypothesis is rejected, the populations means are different. A confidence level of 99% was selected for the ANOVA tests. Therefore, if the null hypothesis for any ANOVA test is rejected, there is a 99% confidence that the two sample means belong to two different populations.

D.1 ANOVA Analysis of Grain Size

Table D.1.1. Grain size values for the base alloy and all addition levels.

Base (µm)	0.005 wt.% Ti (µm)	0.05 wt.% Ti (µm)	0.1 wt.% Ti (µm)	0.2 wt.% Ti (µm)	0.3 wt.% Ti (µm)
1682.0	592.9	911.6	957.6	911.4	955.4
1579.7	619.1	903.2	1022.2	957.6	1013.4
		929.8	927.8	957.5	925.8
		958.8		1001.6	960.9

Table D.1.2. ANOVA (single factor) of grain size for base alloy and 0.005 wt.% Ti level.

Source of Variation	Sum of Squares	Degrees of Freedom	Mean-Square Value	F	α
Between Groups	1050318	1	1050318	376.7371	0.002644
Within Groups	5575.865	2	2787.933		
Total	1055893	3			

$P_{\alpha max} = 1-\alpha$

$P_{\alpha max} = 0.9974$

$P_{\alpha max} = 99.74\%$

$P_{\alpha max} > 99\%$ therefore reject null hypothesis.

This indicates that there was a significant decrease in grain size from the base alloy to the 0.005 wt.% Ti level.

Table D.1.3. ANOVA (single factor) of grain size for 0.005 wt.% Ti and 0.05 wt.% Ti level.

Source of Variation	Sum of Squares	Degrees of Freedom	Mean-Square Value	F	α
Between Groups	136405.4	1	136405.4	252.5312	9.17E-05
Within Groups	2160.61	4	540.1525		
Total	138566	5			

$P_{\alpha max} = 1-\alpha$

$P_{\alpha max} = 0.9999$

$P_{\alpha max} = 99.99\%$

$P_{\alpha max} > 99\%$ therefore reject null hypothesis.

This indicates that there was a significant increase in grain size from the 0.005 wt.% Ti to the 0.05 wt.% Ti level.

Table D.1.4. ANOVA (single factor) of grain size for 0.05 wt.% Ti and 0.1 wt.% Ti level.

Source of Variation	Sum of Squares	Degrees of Freedom	Mean-Square Value	F	α
Between Groups	3221.524	1	3221.524	2.487698	0.175566
Within Groups	6474.91	5	1294.982		
Total	9696.434	6			

$P_{\alpha max} = 1-\alpha$

$P_{\alpha max} = 0.82$

$P_{\alpha max} = 82\%$

$P_{\alpha max} < 99\%$ therefore cannot reject null hypothesis.

This indicates that there was not a significant change in grain size from the 0.05 wt.% Ti to the 0.1 wt.% Ti level.

D.2 ANOVA Analysis of Growth Rate

Table D.2.1. Growth rate values for the base alloy and all addition levels.

Base (µm/s)	0.005 wt.% Ti (µm/s)	0.05 wt.% Ti (µm/s)	0.1 wt.% Ti (µm/s)	0.2 wt.% Ti (µm/s)	0.3 wt.% Ti (µm/s)
28	6.7	16	18	20	23
35	6.6	13	12	29	18
33	7.0	14	15	21	24
35		14	13		
29		13			
36		14			

Table D.2.2. ANOVA (single factor) of growth rate for base alloy and 0.005 wt.% Ti level.

Source of Variation	Sum of Squares	Degrees of Freedom	Mean-Square Value	F	α
Between Groups	1341.62	1	1341.62	163.5552	4.14E-06
Within Groups	57.42	7	8.202857		
Total	1399.04	8			

$P_{\alpha max} = 1-\alpha$

$P_{\alpha max} > 0.9999$

$P_{\alpha max} > 99.99\%$

Since $P_{\alpha max} > 99\%$ reject null hypothesis. This indicates that there was a significant decrease in growth rate from the base alloy to the 0.005 wt.% Ti level.

Table D.2.3. ANOVA (single factor) of growth rate for 0.005 wt.% Ti and 0.05 wt.% Ti level.

Source of Variation	Sum of Squares	Degrees of Freedom	Mean-Square Value	F	α
Between Groups	104.6422	1	104.6422	120.3443	1.16E-05
Within Groups	6.086667	7	0.869524		
Total	110.7289	8			

$P_{\alpha max} = 1-\alpha$

$P_{\alpha max} > 0.9999$

$P_{\alpha max} > 99.99\%$

Since $P_{\alpha max} > 99\%$ reject null hypothesis. This indicates that there was a significant increase in growth rate from the 0.005 wt.% Ti to the 0.05 wt.% Ti level.

D.3 ANOVA Analysis of Coherency Solid Fraction

Table D.3.1. Dendrite coherency solid fraction values for the base alloy and all addition levels.

Base (%)	0.005 wt.% Ti (%)	0.05 wt.% Ti (%)	0.1 wt.% Ti (%)	0.2 wt.% Ti (%)	0.3 wt.% Ti (%)
11.3	19.1	12.6	13.6	11.1	8.93
11.3	21.0	16.2	17.1	7.60	10.6
9.25	20.8	16.2	17.1	9.40	8.97
9.14		12.5	18.7		
13.3		14.3			
9.36		14.3			

Table D.3.2. ANOVA (single factor) of dendrite coherency solid fraction for base alloy and 0.005 wt.% Ti level.

Source of Variation	Sum of Squares	Degrees of Freedom	Mean-Square Value	F	α
Between Groups	187.8568	1	187.8568	82.49007	4.02E-05
Within Groups	15.94128	7	2.277326		
Total	203.7981	8			

$P_{\alpha max} = 1-\alpha$

$P_{\alpha max} > 0.9999$

$P_{\alpha max} > 99.99\%$

Since $P_{\alpha max} > 99\%$ reject null hypothesis. This indicates that there was a significant increase in the coherency solid fraction from the base alloy to the 0.005 wt.% Ti level.

Table D.3.3. ANOVA (single factor) of dendrite coherency solid fraction for 0.005 wt.% Ti and 0.05 wt.% Ti level.

Source of Variation	Sum of Squares	Degrees of Freedom	Mean-Square Value	F	α
Between Groups	70.805	1	70.805	31.94554	0.000773
Within Groups	15.515	7	2.216429		
Total	86.32	8			

$P_{\alpha max} = 1-\alpha$

$P_{\alpha max} = 0.9997$

$P_{\alpha max} = 99.97\%$

Since $P_{\alpha max} > 99\%$ reject null hypothesis. This indicates that there was a significant decrease in the coherency solid fraction from the 0.005 wt.% Ti to the 0.05 wt.% Ti level.

D.4 ANOVA Analysis of Porosity

Table D.4.1. Porosity values for the base alloy and all addition levels.

Base (%)	0.005 wt.% Ti (%)	0.05 wt.% Ti (%)	0.1 wt.% Ti (%)	0.2 wt.% Ti (%)	0.3 wt.% Ti (%)
1.710	0.7343	0.8200	1.179	1.214	1.657
1.533	0.7262	0.8061	1.210	1.412	1.677

Table D.4.2. ANOVA (single factor) of porosity for base alloy and 0.005 wt.% Ti level.

Source of Variation	Sum of Squares	Degrees of Freedom	Mean-Square Value	F	α
Between Groups	0.794327	1	0.794327	101.2055	0.009737
Within Groups	0.015697	2	0.007849		
Total	0.810024	3			

$P_{\alpha max} = 1-\alpha$

$P_{\alpha max} = 0.9903$

$P_{\alpha max} = 99.03\%$

Since $P_{\alpha max} > 99\%$ reject null hypothesis. This indicates that there was a significant decrease in the porosity of the castings from the base alloy to the 0.005 wt.% Ti level.

Table D.4.3. ANOVA (single factor) of porosity for 0.005 wt.% Ti and 0.05 wt.% Ti level.

Source of Variation	Sum of Squares	Degrees of Freedom	Mean-Square Value	F	α
Between Groups	0.006856	1	0.006856	105.9553	0.009306
Within Groups	0.000129	2	6.47E-05		
Total	0.006985	3			

$P_{\alpha max} = 1-\alpha$

$P_{\alpha max} = 0.9906$

$P_{\alpha max} = 99.06\%$

Since $P_{\alpha max} > 99\%$ reject null hypothesis. This indicates that there was a significant decrease in the porosity of the castings from the base alloy to the 0.005 wt.% Ti level.